TU WIEN
TECHNISCHE UNIVERSITÄT WIEN
Vienna | Austria

AG TOSCHI

Diplomarbeit

Breakdown of the self-consistent perturbation theory beyond particle-hole symmetry

zur Erlangung des akademischen Grades

Diplom-Ingenieur

im Rahmen des Studiums

Technische Physik

eingereicht von

Herbert Eßl

Matrikelnummer: 11717680

ausgeführt am Institut für Festkörperphysik
der Fakultät für Physik der Technischen Universität Wien

Betreuung
Betreuer: Associate Prof. Dr. Alessandro Toschi
Mitwirkung: Dipl. Ing. Matthias Reitner

Wien, June 13, 2023   _____   _____
                            (Unterschrift Verfasser)   (Unterschrift Betreuer)

Abstract

The breakdown of the self-consistent perturbation theory for many-electron systems has several physical and formal manifestations. Among the latter ones, of the most studied are **(i)** the divergence of 2-particle irreducible vertex functions and **(ii)** the misleading convergence of the self-consistent perturbation theory, which emerges from the intrinsic multivaluedness of the Luttinger-Ward functional.

Hitherto, most investigations of the perturbation theory breakdown in many-electron models have been restricted to the particle-hole symmetric cases. This Master thesis represents a first step beyond such restrictions.

To this aim, we start by investigating the 2-particle properties of the Hubbard Atom, for positive (repulsive) and negative (attractive) on-site interaction, in order to determine the location in the phase space and the nature of the irreducible vertex divergences as a function of the chemical potential. Further, the $T = 0$ limit of the 2-particle quantities in the Hubbard Atom is investigated in two ways. First, by studying the asymptotic $(T \to 0)$ behavior of the 2-particle quantities in the dimensionless parameter space $\{\mu/T, U/T\}$, exploiting the universality of this representation. Second, by taking the $T = 0$ limit for Lehmann representation of the 2-particle quantities of the Hubbard Atom.

Additionally, by extending the derivation of the Shiba-mapping for local 2-particle quantities beyond SO(4)-symmetry, we get new insights on the vertex divergences in situations, where SU(2)-symmetry is broken due to an external magnetic field.

Finally, we analyze the self-consistent perturbation series beyond the particle-hole symmetry condition, in order to identify the specific constraints for its convergence to the physical solution of the Luttinger-Ward functional at arbitrary electronic densities.

Deutsche Kurzfassung

Der Zusammenbruch der selbstkonsistenten Störungstheorie für Viel-Elektronen-Systeme hat mehrere physikalische und formale Erscheinungsformen. Zu den am meisten untersuchten formalen Erscheinungsformen gehören **(i)** die Divergenz der 2-Teilchen irreduziblen Vertexfunktionen und **(ii)** die irreführende Konvergenz der selbstkonsistenten Störungstheorie, die sich aus der intrinsischen Mehrwertigkeit des Luttinger-Ward-Funktionals ergibt.

Bisher waren die meisten Untersuchungen zum Zusammenbruch der Störungstheorie in Viel-Elektronen-Modellen auf den Fall der Teilchen-Loch-Symmetrie beschränkt. Diese Masterarbeit stellt einen ersten Schritt über solche Beschränkungen hinaus dar.

Zu diesem Zweck untersuchen wir zunächst die 2-Teilchen-Eigenschaften des Hubbard-Atoms bei positiver (abstoßender) und negativer (anziehender) lokaler Wechselwirkung, um die Lage im Phasenraum und die Art der irreduziblen Vertex-Divergenzen als Funktion des chemischen Potentials zu bestimmen. Außerdem wird $T = 0$ Limes der 2-Teilchen-Größen im Hubbard-Atom auf zwei Arten untersucht. Erstens wird das asymptotische ($T \to 0$) Verhalten der 2-Teilchen-Größen im dimensionslosen Parameterraum $\{\mu/T, U/T\}$ unter Ausnutzung der Universalität dieser Darstellung untersucht. Zweitens wird der $T = 0$ Limes für die Lehmann-Darstellung der 2-Teilchen-Größen des Hubbard-Atoms berechnet.

Des Weiteren, wird durch die Herleitung des Shiba-Mappings für lokale 2-Teilchen-Größen über die SO(4)-Symmetrie hinaus erweitert, wodurch wir neue Erkenntnisse über die Vertex-Divergenzen in Situationen, in denen die SU(2)-Symmetrie durch ein externes Magnetfeld gebrochen ist, erhalten. Schließlich analysieren wir die selbstkonsistente Störungsreihe jenseits der Teilchen-Loch-Symmetrie, um die spezifischen Einschränkungen für ihre Konvergenz zur physikalischen Lösung des Luttinger-Ward-Funktionals bei beliebigen elektronischen Dichten zu identifizieren.

Acknowledgement

First, I would like to thank my supervisor Alessandro Toschi for his invaluable scientific advice and guidance throughout my master thesis. His support extended way beyond addressing both real and imagined "Sackgassen" during my master's thesis, he also constatly inspired me with his passion for physics and his deep understanding of the subject. Furthermore, he provided me with the opportunities to participate in schools and a conference, allowing me to engage with the "correlated electrons community". I am very excited to continue working with him during my PhD. I would like to extend my thanks to the research groups led by Alessandro Toschi and Sabine Andergassen for the nice working environment and the group lunches. Especially I want to thank Matthias Reitner, who co-supervised my master thesis and always had time for me to discuss some code, physics, or the properties of weird matrices.

Additionally, I want to express my appreciation to the people from the student's office for a pleasant and enjoyable office atmosphere. In particular, Emin Moghadas and Samuel Badr, who accompanied me on my first scientific trips, enriching my experience.

Zuletzt möchte ich mich bei meinen Eltern und Andreas bedanken, dafür dass sie mich immer ermutigt haben selbst zu entscheiden was ich in meinem Leben machen möchte und mich dann auch noch auf meinem gewählten Weg unterstütz haben. Danke für alles.

Contents

Chapter 1

Introduction

Many interesting phenomena characterize the physics of strongly correlated systems: High-temperature superconductivity in cuprates, nickelates and iron-pnictides/chalcogenides, quantum criticality in heavy fermion systems, Mott-Hubbard or Hund's-Mott metal-to-insulator transitions and many more [1]. This provides a strong motivation, besides mere scientific curiosity, to investigate correlated many-electron systems. However, like in most aspects of life, "there is no free lunch", and these fascinating physics turns out to be exceptionally demanding. More specifically, due to the large number of degrees of freedom in interacting many-electron systems, a quantum field theoretical description is often necessary. Therefore, modern condensed matter theory shares several similarities with quantum electrodynamics (QED) such as the Feynman diagrammatic description [2, 3], albeit with a very important difference: For correlated electrons no universal small expansion parameter, like the fine structure constant α for QED, could be identified in general. Therefore, we will have to deal with non-perturbative parameter regimes, where the Feynman diagrammatic description can, to some extent, break down. In particular, as it has been addressed by the recent literature, the breakdown of self-consistent perturbation theory of many-electron systems has multifaceted physical and formal manifestations [4]. Among the latter ones, of the most studied are: **(i)** the divergence of 2-particle irreducible vertex functions[5–19] and **(ii)** the misleading convergence of the self-consistent perturbation theory[12, 17, 18, 20–25], which originates from the intrinsic multivaluedness of the Luttinger Ward functional. For the study of the irreducible vertex function a systematic investigation of 2-particle quantities, and namely of the generalized susceptibilities [26, 27], is needed: The generalized susceptibilities are linked to the irreducible vertex function via the Bethe-Salpeter equation (BSE) [28], which can be regarded as the 2-particle analogue of the Dyson equation. The BSE becomes not invertible for specific parameter values in several fundamental many-electron models, which leads to the divergence of the corresponding irreducible vertex function [16, 17]. The vertex divergences represent a clear hallmark for the breakdown of self-consistent perturbation theory, which however gives rise to an even more significant effect, namely the misleading convergence of bold (self-consistent) diagrammatic summation. In fact, due to the intrinsic multivaluedness of the Luttinger-Ward functional, several unphysical solutions to the many-electron problem can be found. This mathematical feature has relevant consequences as, these unphysical solutions lead to a misleading convergence of the

self-consistent perturbation theory [18, 20] in large parameter regions. Remarkably, the parameter values where the misleading convergence stets in, are the same as the parameters where the vertex divergences appear. This correspondence has been formalized by a proof that shows that a crossing of the physical with an unphysical solution implies a vertex divergence [12].

In spite of the several studies appeared in the most recent literature, the investigation of the breakdown of self-consistent perturbation theory has been so far mostly[1] limited to finite temperatures and high symmetry cases, e.g. to models with local (Hubbard) interaction where particle-hole symmetry and SU(2)-symmetry, which together lead to a SO(4)-symmetry, are both fulfilled.

This thesis is a first step towards a systematic study of the breakdown of perturbation theory in the more realistic situation of lower symmetry. The thesis is organized as follows: A brief recapitulation of the formalism and the basic models of interest for this thesis (the Hubbard Atom as well as the Anderson Impurity model) is done in chapter 2 followed by a concise summary of the relevant previous results from the literature together with a schematic discussion of open questions in chapter 3.

The following two chapters are devoted to the presentation of the obtained results.

In chapter 4 one of the manifestations of the breakdown of self-consistent perturbation theory, the vertex divergences, are investigated. First, a mapping that links the local generalized susceptibilities out of half filling with SU(2)-symmetry with the corresponding ones at half filling without SU(2)-symmetry is derived in section 4.1). Further, in section 4.2 the vertex divergences of the Hubbard Atom (HA) beyond particle-hole symmetry are studied and a formalism that makes it possible to investigate the $T = 0$ limit is developed in section 4.3. Eventually, the mapping, that is introduced in section 4.1, is used to extend the obtained results to the case with external magnetic field and particle-hole symmetry. This allows us to identify the non-perturbative regimes of the Hubbard Atom in a wide region of the parameter space.

The problematic consequence of this non-perturbative breakdown one best sees in the self-consistent perturbation theory: The second manifestation of the perturbation theory breakdown, the misleading convergence, is studied in chapter 5. To this aim, the Anderson Impurity model (AIM) has been exploited, similarly as in [20], as an auxiliary model to implement an iterative scheme that mimics the misleading convergence of the self-consistent perturbation theory. The misleading convergence of this scheme is investigated beyond particle-hole symmetry, with a particular focus on understanding how the misleading convergence happens in the different parameter regions.

Finally, a conclusion and an outlook are presented in chapter 6.

---

[1]The few expectations are [13, 18, 20], though the focus of these works was not the systematic investigation presented here.

Chapter 2

Formalism and models

The formalism of many-body quantum field theory together with the models that are investigated in this thesis are presented in this chapter. The essential theoretical concepts introduced here are: The n-particle Green's function formalism, the role played by physical symmetries and how they reflect on Green's functions, the definition of generalized and physical susceptibilities and, more on the methodological side, the self-consistent perturbation expansion and the Luttinger-Ward (LW) functional.
Further, the introduced models are the Hubbard Atom (HA) which is the primary focus of this thesis and the Anderson Impurity model (AIM) which used as an auxiliary model.

Parts of this chapter are taken/slightly readopted from a project work of mine [29]. These parts are marked by a black bar on the outer edge of the page.

2.1   Formalism

The common formalism to describe non-relativistic quantum many-body systems is non-relativistic thermal field theory, which has been used for more than fifty years. The central objects in this formal approach are the n-particle Green's functions G_n. For $T \neq 0$ it is useful to work within the Matsubara formalism, which is done by performing a Wick rotation $\tau = it$. As a consequence of this rotation, the Green's function can be only well-defined in the interval $\tau \in [-\beta, \beta]$. One can define the Green's function such that it is periodically continued out of this interval. Because the n-particle Green's function for a fermionic system is "anti-periodic" in the interval $[-\beta, \beta]$ i.e. $G_n(\tau_i) = -G_n(\tau_i + \beta)$ for $\tau \in [-\beta, 0]$. Therefore, it is sufficient to only consider the Green's function on the interval $\tau \in [0, \beta]$. As a consequence of the periodic continuation the Fourier transformed variables (i.e. the frequencies) of the Green's function are discrete $\Omega_n = \frac{n\pi}{\beta}; n \in \mathbb{Z}$, which further divide into odd fermionic Matsubara frequencies $\nu_n = \frac{(2n-1)\pi}{\beta}$ and even bosonic Matsubara frequencies $\omega_n = \frac{2n\pi}{\beta}$ [2, 26, 30, 31].
The explicit definition of the n-particle Green's function used in this work is

$$G_{n,\sigma_1...\sigma_{2n}}(\tau_1,...,\tau_{2n}) := \langle T_\tau c^\dagger_{\sigma_1}(\tau_1) c_{\sigma_2}(\tau_2)...c^\dagger_{\sigma_{2n-1}}(\tau_{2n-1}) c_{\sigma_{2n}}(\tau_{2n}) \rangle, \tag{2.1}$$

where $c^{(\dagger)}_\sigma(\tau) = e^{\tau H} c^{(\dagger)}_\sigma e^{-\tau H}$ and T_τ being Wick's Time ordering operator in imaginary times τ. Note that σ can, in principle, stand for a whole set of quantum numbers. In this work only the spin (the z-direction is used for the quantization axis) is relevant, because our models are local, and only one orbital is considered.

The Fourier expansion of the Green's function reads

$$\tilde{G}_{n,\sigma_1...\sigma_{2n}}(\nu_1,...,\nu_{2n}) := \int_0^\beta d\tau_1...d\tau_{2n} \, e^{-i(\nu_1\tau_1 - \nu_2\tau_2 + ... - \nu_{2n}\tau_{2n})} \, G_{n,\sigma_1...\sigma_{2n}}(\tau_1,...,\tau_{2n}) \tag{2.2}$$

with the inverse Fourier expansion

$$G_{n,\sigma_1...\sigma_{2n}}(\tau_1,...,\tau_{2n}) = \frac{1}{\beta^{2n}} \sum_{\{\nu_i\}} e^{i(\nu_1\tau_1 - \nu_2\tau_2 + ... - \nu_{2n}\tau_{2n})} \, \tilde{G}_{n,\sigma_1...\sigma_{2n}}(\nu_1,...,\nu_{2n}), \tag{2.3}$$

where all $\nu_i = \frac{(2n-1)\pi}{\beta}$ are fermionic Matsubara frequencies. The tilde for the Fourier expanded quantity is dropped in the following, whether the quantity is Fourier expanded or not is made visible by the frequency or time arguments.

2.1.1 Symmetries of the Green's function

The n-particle Green's function of a fermionic system obeys two "symmetries" that are not connected to a unitary transformation that leaves the Hamiltonian of the system invariant. These "symmetries" are therefore always present independent of the system considered. The first one is the crossing symmetry that is connected to the Pauli principle for indistinguishable fermions, that is mathematically encoded in the anticommutation relation of the creation and annihilation operator. The crossing symmetry states that

$$G_{n,\sigma_1..\sigma_i..\sigma_j..\sigma_{2n}}(\tau_1,..,\tau_i,..,\tau_j,..,\tau_{2n}) = -G_{n,\sigma_1..\sigma_j..\sigma_i..\sigma_{2n}}(\tau_1,..,\tau_j,..,\tau_i,..,\tau_{2n}) \tag{2.4}$$

for arbitrary i and j.

The second symmetry that is not connected to a transformation of the specific Hamiltonian is the complex conjugation of the n-particle Green's function. Using the definition of Hermitian transpose $(\langle i| c_1...c_n |j\rangle)^* = \langle j| c^\dagger_n...c^\dagger_1 |i\rangle$ leads to the identity

$$G^*_{n,\sigma_1...\sigma_{2n}}(\tau_1,...,\tau_{2n}) = -G_{n,\sigma_{2n}...\sigma_1}(-\tau_{2n},...,-\tau_1), \tag{2.5}$$

4

where the cyclic property of the trace is used. Fourier expanding Eq. (2.5) gives

$$G^*_{n,\sigma_1...\sigma_{2n}}(\nu_1,...,\nu_{2n}) = -G_{n,\sigma_{2n}...\sigma_1}(-\nu_{2n},...,-\nu_1). \tag{2.6}$$

Now coming to the symmetries that are defined by a unitary transformation U commuting to a specific Hamilton of interest. The consequences of these symmetries are more lengthy to prove, therefore the action of the considered symmetries on the Green's function is just stated here, for a detailed proof the reader is referred to [26].

Time translation symmetry is connected to the operator

$$U = e^{-\tau H}. \tag{2.7}$$

The system is time translation invariant for all time independent Hamiltonians, therefore this symmetry is always fulfilled for the models considered in this work. As a result of this symmetry the Green's function only depends on time differences and one argument of the function can then be discarded

$$G_{n,\sigma_1...\sigma_{2n}}(\tau_1,...,\tau_{2n}) = G_{n,\sigma_1...\sigma_{2n}}(\tau_1 - \tau_{2n},...,0). \tag{2.8}$$

The Fourier expansion of this relation ensures the energy conservation

$$\tilde{G}_{n,\sigma_1...\sigma_{2n}}(\nu_1,...,\nu_{2n}) = \beta\delta_{(\nu_1-\nu_2+...+\nu_{2n-1}),\nu_{2n}}G_{n,\sigma_1...\sigma_{2n-1}}(\nu_1,...,\nu_{2n-1}) \tag{2.9}$$

with the $2n - 1$ frequency Green's function

$$G_{n,\sigma_1...\sigma_{2n}}(\nu_1,...,\nu_{2n-1}) = \int_0^\beta d\tau_1...d\tau_{2n}\, e^{-i(\nu_1\tau_1-\nu_2\tau_2+...+\nu_{2n-1}\tau_{2n-1})}\, G_{n,\sigma_1...\sigma_{2n}}(\tau_1,...,\tau_{2n-1}). \tag{2.10}$$

The next symmetry to be discussed is the SU(2) symmetry. The operator associated to the SU(2) symmetry is

$$U = e^{-i\varphi\vec{n}\cdot\vec{S}} \quad \text{with} \quad \vec{n} \in \mathbb{R}^3, \|\vec{n}\|_2 = 1 \text{ and } \varphi \in [0,2\pi), \tag{2.11}$$

the components of the spin operator in second quantization read

$$S_i = \frac{1}{2}c_\sigma^\dagger \sigma_i^{\sigma\sigma'} c_{\sigma'}, \tag{2.12}$$

5

where the Einstein sum convention is used and σ_i is a Pauli matrix. The SU(2) symmetry evidently implies spin conservation (note that spin conservation can be present without SU(2) symmetry, which is the case for the Hubbard Atom with external magnetic field) which can (e.g. for the quantization axis z) be expressed as:

$$\sigma_1 + \sigma_3 + ... + \sigma_{2n-1} = \sigma_2 + \sigma_4 + ... + \sigma_{2n}. \tag{2.13}$$

The second consequence of SU(2) symmetry is that a flip of all spins ($\sigma_i \mapsto -\sigma_i \ \forall i$) does not change the Green's function.

Due to the spin conservation the 1-particle Green's function depends only on one spin index Eq. (2.14) and due to the SU(2) symmetry the 1-particle Green's function is the same for spin up and spin down Eq. (2.15). Assuming also time translation invariance, the 1-particle Green's function can be written as

$$G_{1,\sigma}(\nu) := \delta_{\sigma\sigma'} G_{1,\sigma\sigma'}(\nu) \tag{2.14}$$

and

$$G_1(\nu) := G_{1,\uparrow}(\nu) = G_{1,\downarrow}(\nu). \tag{2.15}$$

For the 2-particle Green's function it follows from the spin conservation that out of the 2^4 possible combinations only 6 remain,

$$\sigma_1 = \sigma_2 = \sigma_3 = \sigma_4, \quad \sigma_1 = \sigma_2 \neq \sigma_3 = \sigma_4, \quad \sigma_1 = \sigma_4 \neq \sigma_2 = \sigma_3. \tag{2.16}$$

Therefore, the following definitions can be introduced on the 2-particle level which, by considering time translation invariance read

$$G_{2,\sigma\sigma'}(\nu_1, \nu_2, \nu_3) := G_{2,\sigma\sigma\sigma'\sigma'}(\nu_1, \nu_2, \nu_3) \quad \text{and} \quad G_{2,\overline{\sigma\sigma'}}(\nu_1, \nu_2, \nu_3) := G_{2,\sigma\sigma'\sigma\sigma'}(\nu_1, \nu_2, \nu_3). \tag{2.17}$$

These definitions are not independent of each other, as one can show with the crossing symmetry Eq. (2.4). Moreover, because of the SU(2) symmetry there are only two independent 2-particle Green's functions

$$G_{2,\uparrow\uparrow}(\nu_1, \nu_2, \nu_3) = G_{2,\downarrow\downarrow}(\nu_1, \nu_2, \nu_3) \quad \text{and} \quad G_{2,\uparrow\downarrow}(\nu_1, \nu_2, \nu_3) = G_{2,\downarrow\uparrow}(\nu_1, \nu_2, \nu_3). \tag{2.18}$$

Another useful symmetry is the time reversal symmetry. In quantum mechanics the time

reversal operator is given by $U = \sigma_2 \otimes K$ where K is the complex conjugation. For a system where the spin does not couple to other degrees of freedom (orbitals, position, ...) the time reversal operator is just a complex conjugation

$$K\Psi(x) \coloneqq \Psi^*(x). \tag{2.19}$$

A similar argument can be made in quantum field theory, by exploiting the fact that the matrix elements of the creation and annihilation operator in Fock basis $|\{n_j\}\rangle$ are real. Therefore, the matrix elements of the Hamilton operator are also real, if the Hamilton is a real function of c_σ and $c_\sigma^\dagger$. This also holds for real functions of the Hamilton operator like $e^{\tau H}$. As a consequence of the time reversal symmetry, the n-particle Green's function in imaginary time is purely real

$$G^*_{n,\sigma_1...\sigma_{2n}}(\tau_1, ..., \tau_{2n}) = G_{n,\sigma_1...\sigma_{2n}}(\tau_1, ..., \tau_{2n}). \tag{2.20}$$

Further, if one uses the complex conjugation Eq. (2.5) and time translation symmetry Eq. (2.8) where each time is shifted by β one gets

$$G_{n,\sigma_1...\sigma_{2n}}(\tau_1, ..., \tau_{2n}) = G_{n,\sigma_{2n}...\sigma_1}(-\tau_{2n}, ..., -\tau_1) = G_{n,\sigma_{2n}...\sigma_1}(\beta - \tau_{2n}, ..., \beta - \tau_1). \tag{2.21}$$

Eventually, by Fourier expanding Eq. (2.21) and using again time translation invariance by setting the last time to zero we get

$$G_{n,\sigma_1...\sigma_{2n}}(\nu_1, ..., \nu_{2n-1}) = G_{n,\sigma_{2n}...\sigma_1}(\nu_{2n}, ..., \nu_2), \tag{2.22}$$

where $\nu_{2n} = \nu_1 - \nu_2 + ... + \nu_{2n-1}$ ensures energy conservation.

Finally, we consider the special case of the particle-hole symmetry. The Hubbard Atom is only particle-hole symmetric if $\mu = U/2$. The corresponding unitary particle-hole transformation for the Hubbard Atom reads

$$U = W = (c_\uparrow^\dagger + c_\uparrow)(c_\downarrow^\dagger + c_\downarrow), \tag{2.23}$$

which transforms the creation and annihilation operator as

$$c_\sigma' = W^\dagger c_\sigma W = c_\sigma^\dagger \quad \text{and} \quad c_\sigma^{\dagger\prime} = W^\dagger c_\sigma^\dagger W = c_\sigma. \tag{2.24}$$

For particle-hole symmetric systems the relation

$$G_{n,\sigma_1\ldots\sigma_{2n}}(\tau_1,\ldots,\tau_{2n}) = (-1)^n G_{n,\sigma_{2n}\ldots\sigma_1}(\tau_{2n},\ldots,\tau_1) \qquad (2.25)$$

holds. Using the relation for complex conjugation Eq. (2.5) and transforming Eq. (2.25) into Fourier space, using time translation invariance, finally yields

$$G^*_{n,\sigma_1\ldots\sigma_{2n}}(\nu_1,\ldots,\nu_{2n-1}) = (-1)^n G_{n,\sigma_1\ldots\sigma_{2n}}(\nu_1,\ldots,\nu_{2n-1}). \qquad (2.26)$$

Therefore, the Green's function for particle-hole symmetric systems is either purely real or purely complex, depending on n.

2.1.2 Generalized susceptibility

In general, instead of working with the 2-particle Green's function a directly related quantity is considered: The generalized susceptibility, which is defined as follows

$$\chi_{\sigma_1\sigma_2\sigma_3\sigma_4}(\tau_1,\tau_2,\tau_3,\tau_4) = G_{2,\sigma_1\sigma_2\sigma_3\sigma_4}(\tau_1,\tau_2,\tau_3,\tau_4) - G_{1,\sigma_1\sigma_2}(\tau_1,\tau_2)G_{1,\sigma_3\sigma_4}(\tau_3,\tau_4), \qquad (2.27)$$

where the last term is often referred to as *bubble* term and is defined as

$$\chi_{0,\sigma_1\sigma_2\sigma_3\sigma_4}(\tau_1,\tau_2,\tau_3,\tau_4) = -G_{1,\sigma_1\sigma_4}(\tau_1,\tau_4)G_{1,\sigma_3\sigma_2}(\tau_3,\tau_2). \qquad (2.28)$$

The physical susceptibility can be obtained by taking the limits $\tau_2 \to \tau_1^-, \tau_4 \to \tau_3^-, \tau_4 \to 0$. By considering spin conservation Eqs. (2.16), (2.17) and then time translation invariance Eq. (2.8), one can define the generalized susceptibility as

$$\chi_{\sigma\sigma'}(\tau_1,\tau_2,\tau_3) := \chi_{\sigma\sigma\sigma'\sigma'}(\tau_1,\tau_2,\tau_3,0). \qquad (2.29)$$

Although it is possible to define $\chi_{\overline{\sigma\sigma'}}$ based on Eq. (2.17), it is not often used since it lacks independence from $\chi_{\sigma\sigma'}$, as evident through the application of crossing symmetry.

For the Fourier transformation it is useful to introduce two frequency conventions, as they correspond to two distinct physical situations. The particle-hole (ph) and the particle-particle (pp) notation

$$\textbf{ph:}\ \nu_1 = \nu \qquad\qquad\qquad \textbf{pp:}\ \nu_1 = \nu \qquad\qquad\qquad (2.30\text{a})$$

$$\nu_2 = \nu + \omega \qquad\qquad\qquad \nu_2 = \omega - \nu' \qquad\qquad\qquad (2.30\text{b})$$

$$\nu_3 = \nu' + \omega \qquad\qquad\qquad \nu_3 = \omega - \nu \qquad\qquad\qquad (2.30\text{c})$$

$$\nu_4 = \nu' \qquad\qquad\qquad\qquad \nu_4 = \nu', \qquad\qquad\qquad\quad (2.30\text{d})$$

where $\nu = \frac{\pi}{\beta}(2n-1)$ and $\nu' = \frac{\pi}{\beta}(2n'-1)$ are fermionic Matsubara frequencies and $\omega = \frac{\pi}{\beta}2m$ is a bosonic Matsubara frequency. One interprets the creation (annihilation) operators as outgoing (incoming) electrons and incoming (outgoing) holes. The two notations correspond to the following physical situations: The ph-notation describes the scattering of an electron with energy $\nu + \omega$ with a hole with energy $-\nu$, where the transferred energy of the process is ω. The pp-notation describes the scattering of two electrons with energies ν' and $\omega - \nu'$ again with the transfer energy ω. These two processes are visualized in Fig. 2.1.
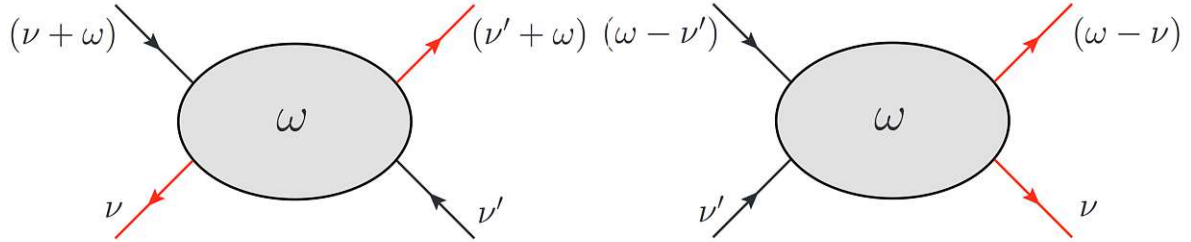
Figure 2.1: **Left:** A process in ph-notation. **Right:** A process in pp-notation. Picture taken from [26].

The Fourier transformation of these two notations are defined as

$$\chi_{\text{ph},\sigma\sigma'}^{\nu\nu'\omega} := \int_0^\beta d\tau_1 d\tau_2 d\tau_3\, \chi_{\sigma\sigma'}(\tau_1,\tau_2,\tau_3)\, e^{-i\nu\tau_1} e^{i(\nu+\omega)\tau_2} e^{-i(\nu'+\omega)\tau_3} \qquad (2.31)$$

and

$$\chi_{\text{pp},\sigma\sigma'}^{\nu\nu'\omega} := \int_0^\beta d\tau_1 d\tau_2 d\tau_3\, \chi_{\sigma\sigma'}(\tau_1,\tau_2,\tau_3)\, e^{-i\nu\tau_1} e^{i(\omega-\nu')\tau_2} e^{-i(\omega-\nu)\tau_3}, \qquad (2.32)$$

where one can view $\chi^{\nu\nu'\omega}$ as infinite dimensional matrix in the fermionic Matsubara space for fixed ω. From the definitions Eqs. (2.31), (2.32) one can also see that χ_{ph} can be transformed into χ_{pp} and vice versa by the frequency shift

$$\chi_{\text{pp},\sigma\sigma'}^{\nu\nu'\omega} = \chi_{\text{ph},\sigma\sigma'}^{\nu\nu'(\omega-\nu-\nu')}. \qquad (2.33)$$

In Eqs. (2.34) to (2.38) all relevant symmetries that were discussed in section 2.1.1 are displayed

in the context of susceptibilities

$$\text{Crossing Symmetry: } \chi_{\text{ph},\sigma\sigma'}^{\nu\nu'\omega} = \chi_{\text{ph},\sigma'\sigma}^{(\omega+\nu')(\omega+\nu)-\omega}$$
$$\chi_{\text{pp},\sigma\sigma'}^{\nu\nu'\omega} = \chi_{\text{pp},\sigma'\sigma}^{(\omega-\nu)(\omega-\nu')\omega} \tag{2.34}$$

$$\text{Complex Conjugation: } (\chi_{\sigma\sigma'}^{\nu\nu'\omega})^* = \chi_{\sigma'\sigma}^{-\nu'-\nu-\omega} \tag{2.35}$$

$$\text{Time reversal symmetry: } \chi_{\sigma\sigma'}^{\nu\nu'\omega} = \chi_{\sigma'\sigma}^{\nu'\nu\omega} \tag{2.36}$$

$$\text{SU(2) symmetry: } \chi_{\sigma\sigma'}^{\nu\nu'\omega} = \chi_{\sigma'\sigma}^{\nu\nu'\omega} \tag{2.37}$$

$$\text{Particle-hole symmetry: } (\chi_{\sigma\sigma'}^{\nu\nu'\omega})^* = \chi_{\sigma\sigma'}^{\nu\nu'\omega}, \tag{2.38}$$

where a relation without ph or pp index means that this relation holds for particle-hole and particle-particle notation.

To obtain the physical susceptibility (as a function of a bosonic Matsubara frequency ω) one needs to sum over all fermionic frequencies, which precisely corresponds to the limits $\tau_2 \to \tau_1^-, \tau_4 \to \tau_3^-, \tau_4 \to 0$

$$\chi_{\sigma\sigma'}^{\text{physical}}(\omega) = \frac{1}{\beta} \sum_{\nu\nu'} \chi_{\sigma\sigma'}^{\nu\nu'\omega}. \tag{2.39}$$

In general, one can split the generalized susceptibility into two terms (one Wick contraction is eliminated by the bubble term in Eq. (2.27))

$$\chi_{\sigma\sigma'}^{\nu\nu'\omega} = \chi_0^{\nu\nu'\omega}\delta_{\sigma\sigma'} - \frac{1}{\beta^2} \sum_{\nu_1\nu_2} \chi_0^{\nu\nu_1\omega} F_{\sigma\sigma'}^{\nu_1\nu_2\omega} \chi_0^{\nu_2\nu'\omega}, \tag{2.40}$$

with

$$\chi_{0,\text{ph}}^{\nu\nu'\omega} = -\beta G(\nu)G(\nu+\omega)\delta_{\nu\nu'} \quad \text{and} \quad \chi_{0,\text{pp}}^{\nu\nu'\omega} = -\beta G(\nu)G(\omega-\nu)\delta_{\nu\nu'}. \tag{2.41}$$

The first part of in Eq. (2.40) is given by the product of two 1-particle Green's functions and

evidently belongs to the class of bubble contributions, while the second term entails a connected 2-particle Green's function. Diagrammatically, this can be expressed as shown in Fig. 2.2.

Figure 2.2: Diagrammatic representation of the generalized susceptibility. Picture taken from [26].

The different scattering processes contributing to the full vertex F can be characterized by the (2-particle) reducibility of their diagrammatic representation. The three channels are characterized by the lines that are cut so that the diagram falls apart. This characterization is called the parquet decomposition [26, 28]. A diagram in the full vertex is either fully two particle irreducible or (2-particle) reducible in exactly one channel. The channels are the particle-particle channel (pp) the particle-hole longitudinal channel (ph) and the particle-hole transverse channel $(\overline{\text{ph}})$.

$$F = \Lambda + \Phi_{\text{pp}} + \Phi_{\text{ph}} + \Phi_{\overline{\text{ph}}}, \tag{2.42}$$

where Λ is the fully irreducible part and Φ_r is reducible in channel r.
The parquet equation together with diagrammatic examples is shown in Fig. 2.3.
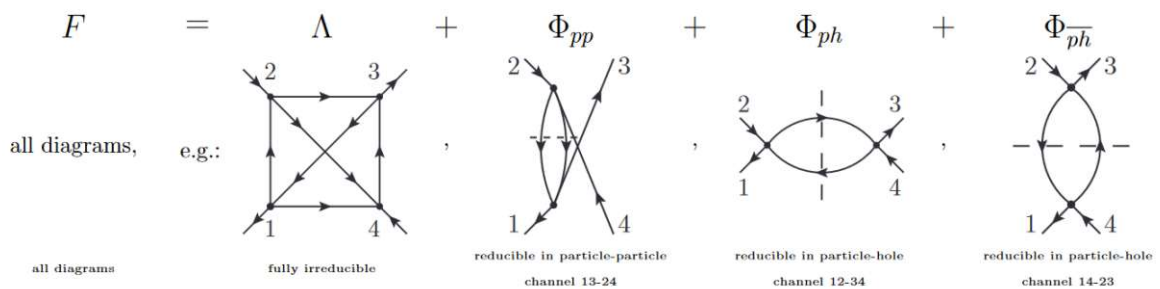
Figure 2.3: Parquet decomposition with diagrammatic examples. Picture taken from [26].

Because a diagram is either fully irreducible or reducible in exactly one channel, one can also define an irreducible vertex for a specific channel r: $\Gamma_r = \Lambda + \Phi_j + \Phi_i; i, j \neq r$.
Furthermore, in the presence of SU(2) symmetry, it is convenient to introduce new channels for the spin degree of freedom so that these channels do not mix. The channels that are used

through this work are the charge, spin, and the pairing channel

$$\chi_{\mathrm{c}}^{\nu\nu'\omega} := \chi_{\mathrm{ph},\uparrow\uparrow}^{\nu\nu'\omega} + \chi_{\mathrm{ph},\uparrow\downarrow}^{\nu\nu'\omega}, \tag{2.43}$$

$$\chi_{\mathrm{s}}^{\nu\nu'\omega} := \chi_{\mathrm{ph},\uparrow\uparrow}^{\nu\nu'\omega} - \chi_{\mathrm{ph},\uparrow\downarrow}^{\nu\nu'\omega} \tag{2.44}$$

and

$$\chi_{\mathrm{pair}}^{\nu\nu'\omega} := \chi_{\mathrm{pp},\uparrow\downarrow}^{\nu(\omega-\nu')\omega} - \chi_{0,\mathrm{pp}}^{\nu\nu'\omega}, \tag{2.45}$$

with the associated irreducible vertices

$$\Gamma_{\mathrm{c/s}}^{\nu\nu'\omega} := \Gamma_{\mathrm{ph},\uparrow\uparrow}^{\nu\nu'\omega} \pm \Gamma_{\mathrm{ph},\uparrow\downarrow}^{\nu\nu'\omega} \quad \text{and} \quad \Gamma_{\mathrm{pair}}^{\nu\nu'\omega} := \Gamma_{\mathrm{pp},\uparrow\downarrow}^{\nu(\omega-\nu')\omega} - \Gamma_{0,\mathrm{pp}}^{\nu\nu'\omega}. \tag{2.46}$$

The latter can be used to write the Bethe-Salpeter equation (BSE) Eq. (2.47), which represents the 2-particle analogue to the well known Dyson equation $G = G_0 + G_0\Sigma G$

$$\pm\chi_r^{\nu\nu'\omega} = \chi_{0,r}^{\nu\nu'\omega} - \frac{1}{\beta^2}\chi_{0,r}^{\nu\nu_1\omega}\Gamma^{\nu_1\nu_2\omega}\chi_r^{\nu_2\nu'\omega}, \tag{2.47}$$

where there is a sum over repeated indices and the plus for the charge and spin channel and the minus for the pairing channel. Diagrammatically, this equation can be visualized as in Fig. 2.4.
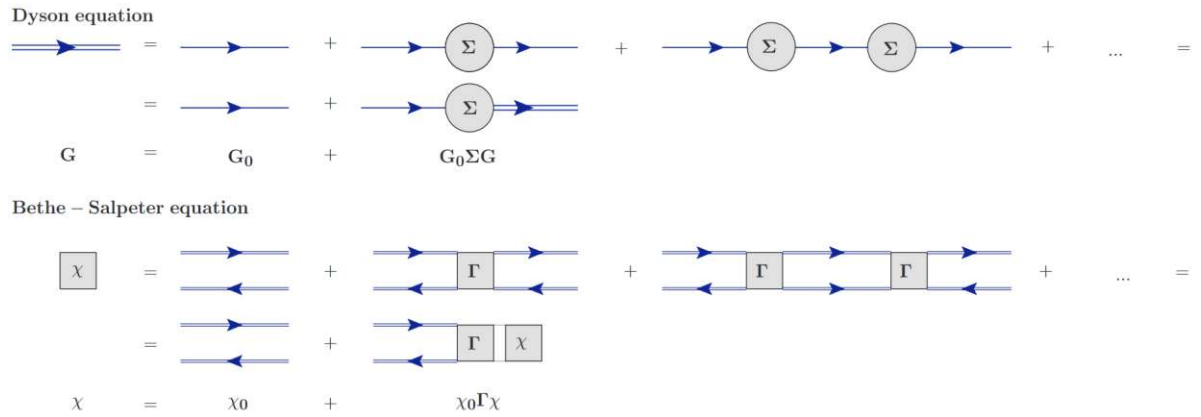
Figure 2.4: Diagrammatic representation of the Dyson equation and the Bethe-Salpeter equation, where double lines represent the dressed Green's function G. Picture taken from [17]

The treatment of generalized susceptibilities as infinite dimensional matrices in fermionic Matsubara space is possible, since the different bosonic frequency planes do not couple (see Eq. (2.47)). Further, the generalized susceptibilities can be treated approximately as finite dimensional matrices because

in the high frequency limit $\nu, \nu' \to \pm\infty$, they decline with $\frac{1}{\nu^2}$ and become diagonal. This is the trivial non-interaction high-frequency behavior and can be neglected safely by taking a finite matrix from $-\nu_{\mathrm{max}}$ to ν_{max} if ν_{max} is big enough to capture all physical relevant behavior. Evidently the smaller β is, the fewer frequencies are needed to get a good approximation.

2.1.3 Self-consistent perturbation expansion

The perturbative expansion of the one-particle Green's function can diagrammatically be done in two ways. One is to calculate the Green's function up to a specific order (in interaction) by drawing all diagrams up to this order and then summing up the diagrams. In this case the diagrams are built with the non-interacting Green's function G_0 and the interaction U. Since the number of diagrams grows exponential with the order [3] this approach become numerically heavy when several orders have to be considered. An alternative approach is the self-consistent perturbation expansion. For this approach the self energy Σ is defined as the sum of all skeleton diagrams without the two external legs[1]. The skeleton diagrams for Σ are 2-particle irreducible diagrams with the two external legs amputated. Additionally, all non-interacting Green's functions are replaced by full Green's functions G in the skeleton diagrams. Therefore, the self energy can be seen as a functional of G and U: $\Sigma = \Sigma[G, U]$. Hence, it follows that the Dyson equation can be rewritten as a self-consistent equation of G (for known G_0)

$$G = \frac{1}{G_0^{-1} - \Sigma[G]}. \tag{2.48}$$

In principle, this equation could be used to self-consistently compute G, if $\Sigma[G]$ is known. Unfortunately, the form of the functional $\Sigma[G]$ is normally not known[2]. Therefore, one approximates the functional $\Sigma[G]$ with $\Sigma_{\mathrm{approx}}[G]$, which is a chosen set of skeleton diagrams. Starting from some G (usually $G_{\mathrm{start}} = G_0$) one calculates $\Sigma_{\mathrm{approx}}[G]$ then a new G is calculated via Eq. (2.48). This new G is used to calculate $\Sigma_{\mathrm{approx}}[G]$ again. These two steps are done iteratively until the procedure converges to a certain G.

2.1.4 Luttinger-Ward (LW) functional

In order to derive an explicit expression for the grand canonical potential Ω for interacting fermions in terms of the Green's function G Luttinger and Ward introduced the Luttinger-Ward (LW) functional [32]. The LW functional plays an essential role when one considers self-consistent field theory (SCF) as it is done in Ref. [28]. Following [28], one can split the action S in a non-interacting part S_0 and an interacting part S_V. Then S can be rewritten in terms of a SCF part S_{SCF} and the difference to the exact expression ΔS

---

[1]Normally, the self energy is the sum of all one-particle irreducible diagrams without external legs
[2]Even in such a simple model as the Hubbard Atom its expression is unknown

$$S = S_{\mathrm{SCF}} + \Delta S \tag{2.49}$$

with

$$S_{\mathrm{SCF}} = S_0 + \beta \sum_{kk'\sigma\sigma'} \Sigma_{\sigma\sigma'}(k,k') c_\sigma^\dagger(k) c_{\sigma'}(k') + \beta\bar{\Omega}, \tag{2.50}$$

where $k = (\mathbf{k}, i\nu_n)$, representing $\mathbf{k}$ the crystal momentum of the electron and $\nu_n = (2n-1)\pi/\beta$ a fermionic Matsubara frequency, Σ is the self-consistent field and $\bar{\Omega}$ is a c-number. The SCF action gives rise to a self-consistent propagator

$$G_\sigma^{\mathrm{SCF}}(k) = \frac{1}{i\nu - (\epsilon_{\mathbf{k}} - \mu) - \Sigma_\sigma(k)}, \tag{2.51}$$

where space translation symmetry, time translation symmetry and spin conservation are assumed. In principle ΔS can be made arbitrary small by choosing an appropriate Σ and $\bar{\Omega}$ [28]. Hence, the exact solution can be obtained with the SCF approach.

The SCF grand canonical potential Ω_{SCF} is defined by

$$e^{-\beta\Omega_{\mathrm{SCF}}} := Z_{\mathrm{SCF}} = \int \mathcal{D}c^\dagger \mathcal{D}c \, e^{-S_{\mathrm{SCF}}} \tag{2.52}$$

and therefore Ω_{SCF} reads

$$\Omega_{\mathrm{SCF}} = -1/\beta \, \mathrm{Tr} \ln(-\beta G_{\mathrm{SCF}}^{-1}) + \bar{\Omega}. \tag{2.53}$$

At this point $\bar{\Omega}$ is still arbitrary but by requiring consistency of thermodynamic derivatives and respect of local conservation laws (or continuity equations) for particle number, momentum, and energy, this arbitrariness disappears and

$$\bar{\Omega} = -\mathrm{Tr}(\Sigma G_{\mathrm{SCF}}) + \Phi, \tag{2.54}$$

where Φ is the famous LW functional that has the property

$$\frac{\delta\Phi}{\delta G_\sigma^{\mathrm{SCF}}(k)} = \Sigma_\sigma(k). \tag{2.55}$$

Further, it holds that

$$\frac{\delta \Sigma_\sigma(k)}{\delta G^{\text{SCF}}_{\sigma'}(k')} = \frac{\delta^2 \Phi}{\delta G^{\text{SCF}}_\sigma(k) \delta G^{\text{SCF}}_{\sigma'}(k')} = \Gamma^{\text{ph}}_{\sigma\sigma'}(k, k') \tag{2.56}$$

as it can also be seen in [28].

Diagrammatically the LW functional is defined as the sum of all closed[3] skeleton diagrams with certain symmetry prefactors [33]. Φ is therefore a functional of the full Green's function G and the interaction U. An important application of the LW functional is its use in constructing approximate approaches to compute the self-energy Σ and Green's function G. These approaches, known as Φ-derivable schemes, are called conserving approximations. Which means that quantities that are conserved on the microscopic level are also conserved on the macroscopic level in Φ-derivable approximations.

2.2 Models

2.2.1 Hubbard Atom (HA)

The model studied in this thesis is the single orbital Hubbard Atom (HA), which describes correlated electrons in a single orbital on an *isolated* lattice site, which interact via an instantaneous and purely local electrostatic repulsion U. Because of the Pauli principle, the maximum number of electrons on this lattice point is limited to two, with opposite spin directions. The HA can be regarded as the limiting case of other more complicated many-electron models. For example, it corresponds to a Hubbard model, whose hopping amplitude t is set to zero, therefore it is also often referred to as *atomic limit*. It is also equivalent to an Anderson Impurity model (AIM) in the limit of a vanishing hybridization function Δ between the impurity site and the non-interacting electronic bath. Evidently, the HA provides an idealized description of the physics of localized magnetic moments, at least in the limit $T \ll U$.

The Hamilton of the Hubbard Atom in second quantization reads:

$$H = -\mu(n_\uparrow + n_\downarrow) - h(n_\uparrow - n_\downarrow) + U n_\uparrow n_\downarrow \quad \text{with} \quad n_\sigma = c^\dagger_\sigma c_\sigma, \tag{2.57}$$

where $c^{(\dagger)}_\sigma$ annihilates (creates) an electron with spin $\sigma = \uparrow, \downarrow$ on the single site/orbital considered, μ is the chemical potential and h is an external magnetic field in z-direction. For the scope of this master thesis we assume that the gyro-magnetic factor of the fermionic particles is *positive*, consistent with the notation of [34]. If electrons are considered, the shift $h \to -h$ is needed. These operators obey the anticommutation rule of fermionic operators, i.e. $\{c^\dagger_\sigma, c_{\sigma'}\} = \delta_{\sigma,\sigma'}$. As one can see, the Hubbard Atom is purely local and the only parameters relevant for its physical description are the chemical potential μ and the local ("Hubbard") interaction U between two

---

[3]Closed diagrams are diagrams that do not have external variables

electrons.

The Hilbert space of the Hubbard Atom is four dimensional, being defined by the following eigenstates and eigenenergies

$$N = \{|0\rangle, |\uparrow\rangle, |\downarrow\rangle, |\uparrow\downarrow\rangle\} \quad \text{and} \quad E_N = \{0, -\mu - h, -\mu + h, U - 2\mu\}. \tag{2.58}$$

The Hubbard Atom is half filled for $\mu = U/2$ as one can see by calculating the occupation number $\langle n_\uparrow + n_\downarrow \rangle$, where the thermal expectation value $\langle ... \rangle$ is given by

$$\langle A \rangle = \frac{1}{Z} Tr(e^{-\beta H} A) \quad \text{with} \quad Z = Tr(e^{-\beta H}) = 1 + e^{\beta(\mu+h)} + e^{\beta(\mu-h)} + e^{\beta(2\mu-U)}. \tag{2.59}$$

Therefore

$$\langle n_\sigma \rangle = \frac{1}{Z} \sum_N \langle N| e^{-\beta E_N} n_\sigma |N\rangle = \frac{e^{\beta(\mu+\sigma h)} + e^{\beta(2\mu-U)}}{1 + e^{\beta(\mu+h)} + e^{\beta(\mu-h)} + e^{\beta(2\mu-U)}}, \tag{2.60}$$

with $\sigma \in \{-1, +1\}$ and $\langle n_\uparrow + n_\downarrow \rangle = 1$ for $\mu = U/2$. The double occupancy reads

$$\langle n_\uparrow n_\downarrow \rangle = \frac{e^{\beta(2\mu-U)}}{1 + e^{\beta(\mu+h)} + e^{\beta(\mu-h)} + e^{\beta(2\mu-U)}}. \tag{2.61}$$

2.2.2 Anderson Impurity model (AIM)

A quantum impurity model describes an interacting impurity hosted in a non-interacting Fermi sea with which it can exchange electrons. The physical systems that can be described with impurity models are for example dilute metal alloys, quantum dots and molecular conductors [35]. Moreover, impurity models are often used as auxiliary models, since they can be solved numerical exact with continuous-time Quantum Monte Carlo solvers [36], this is done for example in dynamical mean field theory (DMFT) [37] and also in this thesis the AIM is used as an auxiliary model.

In this section we consider a single-orbital Anderson Impurity model (AIM) [35]. The single-orbital AIM is described by the Hamiltonian

$$H = \sum_{k,\sigma} \varepsilon_k c^\dagger_{k,\sigma} c_{k,\sigma} - \mu \sum_\sigma d^\dagger_\sigma d_\sigma + U d^\dagger_\uparrow d_\uparrow d^\dagger_\downarrow d_\downarrow + \sum_{k,\sigma} V_{k,\sigma} d^\dagger_\sigma c_{k,\sigma} + V^*_{k,\sigma} c^\dagger_{k,\sigma} d_\sigma, \tag{2.62}$$

where $c^{(\dagger)}_{k,\sigma}$ annihilates (creates) an electron in the non-interacting bath with spin σ and momentum k and $d^{(\dagger)}_\sigma$ annihilates (creates) an electron on the impurity with spin σ. The coupling between the impurity and the bath is described by $V_{k,\sigma}$ and U refers to the on-site interaction at the impurity. Since the terms in the Hamiltonian that describe the coupling between impurity and bath and the bath itself are quadratic, the bath degrees of freedom can be integrated out and the partition function of the remaining impurity can be written as

$$Z = \text{Tr}_{\text{d}}(T_\tau e^{-S}),\tag{2.63}$$

where the effective action S of the impurity reads

$$S = \int_0^\beta d\tau\, U n_\uparrow(\tau) n_\downarrow(\tau) - \mu\left(n_\uparrow(\tau) + n_\downarrow(\tau)\right) + \sum_\sigma \int_0^\beta d\tau d\tau'\, d_\sigma^\dagger(\tau') \Delta_\sigma(\tau' - \tau) d_\sigma(\tau),\tag{2.64}$$

with

$$n_\sigma(\tau) = d_\sigma^\dagger(\tau) d_\sigma(\tau).\tag{2.65}$$

The coupling to the bath is replaced by the hybridization function Δ, which represents the amplitude of an electron hopping from the impurity to the bath at τ and back to the impurity at τ', and reads

$$\Delta_\sigma(i\nu_n) = \sum_k \frac{|V_{k,\sigma}|^2}{i\nu_n - \varepsilon_k}.\tag{2.66}$$

The non-interacting Green's function of the AIM $\mathcal{G}_0$ then reads

$$\mathcal{G}_{0,\sigma}^{-1}(i\nu_n) = i\nu_n + \mu - \Delta_\sigma(i\nu_n).\tag{2.67}$$

For continuous-time Quantum Monte Carlo solvers, two different expansions in the partition Eq. (2.63) are possible: The interaction expansion where the exponential in Eq. (2.63) is expanded for the interaction term and the hybridization expansion where the expansion is done in the term with the hybridization.

Chapter 3

State of the art and open questions

This chapter concisely illustrates a selection of the existing results on the breakdown of perturbation theory. This has two main manifestations: (i) The divergence of the irreducible vertex functions and (ii) the misleading convergence of the self-consistent perturbation theory, which emerges from the intrinsic multivaluedness of the Luttinger-Ward functional. Further, it is recalled how these two aspects of the perturbative breakdown are connected according to the recent literature. Finally, the main limitations of the existing studies, which are mostly focused on the parameter region at or close to particle-hole symmetry, are addressed.

To date, most of the existing studies on the two manifestations of the breakdown of many-electron perturbation theory are considering the special case of perfect particle-hole symmetry. The calculations of this thesis, discussed in the following chapters 4 and 5, represent one of the first steps towards an important generalization of these studies to the more realistic situations encountered in condensed matter physics, where the particle-hole symmetry is not fulfilled.
Parts of this chapter are taken/slightly readopted from a project work of mine [29]. These parts are marked by a black bar on the outer edge of the page.

3.1   Vertex divergences

In reference [17] it is shown that a divergence in the irreducible vertex $\Gamma_r^{\nu\nu'\omega}$ corresponds to an eigenvalue that is zero in the generalized susceptibility $\chi_r^{\nu\nu'\omega}$. This is done by using the BSE Eq. (2.47). Viewing the quantity $\mathbf{X}(\omega)$ as a matrix in the fermionic Matsubara frequency space (ν, ν') for a fixed bosonic frequency ω, one can invert the BSE

$$\mathbf{\Gamma}_r(\omega) = \beta^2(\boldsymbol{\chi}_r^{-1}(\omega) \mp \boldsymbol{\chi}_{r,0}^{-1}(\omega)), \tag{3.1}$$

where $...^{-1}$ is a matrix inversion in the fermionic frequency space, and the minus/plus sign has to be taken for $r = $ c,s/pair. The bubble term $\boldsymbol{\chi}_{r,0}$ is a diagonal matrix, given by the product of two Green's functions. The elements of the bubble term are always different from zero for

finite temperatures except for the trivial limit $\nu \to \infty$ (the matrix is proportional to $1/\nu^2$ in the high ν limit, which corresponds to a high-frequency a non-interacting behavior). Therefore, the irreducible vertex $\mathbf{\Gamma}_r$ only diverges if the matrix $\mathbf{\chi}_r$ is singular, i.e. has an eigenvalue that is equal to zero.

Often it is useful to view the generalized susceptibility in its eigenvalue decomposition

$$\chi_r^{\nu\nu'\omega} = \sum_l v_{l,r}^{-1}(\nu)\,\lambda_{l,r}\,v_{l,r}(\nu'), \tag{3.2}$$

where λ_l and v_l are eigenvalues and eigenvectors of χ and v_l^{-1} is the lth row in the inverse of the eigenvector matrix V. The physical corresponding susceptibility then reads

$$\chi_r^{\text{physical}}(\omega) = \sum_l \lambda_{l,r} w_{l,r} \quad \text{with} \quad w_{l,r} = \sum_\nu v_{l,r}^{-1}(\nu) \sum_{\nu'} v_{l,r}(\nu'), \tag{3.3}$$

where w_l defines the weight of the lth eigenvalue.

Since the divergences in the irreducible vertex are caused by vanishing eigenvalues of the generalized susceptibility, it is useful to analyze the properties of the corresponding eigenvectors in terms of the possible symmetries of the system. In Tab. 3.1 the properties of the generalized susceptibility for $\omega = 0$ are shown. The table distinguishes between cases that involve different symmetries, while always assuming time translation invariance. These are: CC=complex conjugation, CS=crossing symmetry, TR=time reversal and SU(2).

Symmetry	$\boldsymbol{\chi}_{\sigma\sigma',\text{ph}}(\omega = 0)$	$\boldsymbol{\chi}_{\sigma\sigma',\text{pp}}(\omega = 0)$
CC+CS	centro-hermitian	hermitian
TR+SU(2)	centro-hermitian, symmetric	real, bi-symmetric
PH	real, centro-hermitian	real, symmetric
PH+TR+SU(2)	real, bi-symmetric	real, bi-symmetric

Table 3.1: Table for the properties of the generalized susceptibility when different symmetries are considered. Properties taken from [38].

Centro-hermitian means that

$$\boldsymbol{J}\boldsymbol{\chi}\boldsymbol{J} = \boldsymbol{\chi}^* \quad \text{with} \quad J^{\nu\nu'} = \delta^{\nu-\nu'} \tag{3.4}$$

and a bi-symmetric matrix is simultaneously centro-symmetric and symmetric [39].

As it can be seen in Tab. 3.1 the generalized susceptibility is no longer hermitian when some symmetries are broken. But generalized susceptibility remains a centro-hermitian matrix independent of the symmetries that are broken Tab. 3.1. Therefore, the eigenvalues of the generalized susceptibility are either real or come in complex conjugate pairs [39]. The existence

of complex conjugate pairs as eigenvalues can lead to the formation of so called *pseudo-divergences* (see section 4.2 for more information).

An explicit calculation of the analytically exact expression for the 1- and 2-particle Green's function for the Hubbard Atom is performed in reference [34]. Hence, from that, it is also possible to calculate the generalized susceptibilities. The formalism was adopted to the particle-hole convention Eq. (2.30a) in a bachelor thesis at the group [40] (see also appendix A.1).

In Ref. [5] the irreducible vertex of the Hubbard Atom are analytically calculated for the half filling case ($\mu = U/2$). There it is shown that the eigenvectors of the generalized susceptibility $\chi_r^{\nu\nu'\omega}$ corresponding to the divergences in the irreducible vertex $\Gamma_r^{\nu\nu'\omega}$ are either antisymmetric and localized or symmetric and delocalized in Matsubara frequency space. In the charge channel (in [5] d(ensity) channel) the divergences for $\omega = 0$ are defined by the condition following

$$\nu^* = \pm \frac{U}{2}\sqrt{3} \text{ for the antisymmetric singularity} \tag{3.5}$$

and

$$\frac{U\tan\left(\frac{\beta}{2}|B_c|\right)}{2|B_c|} + 1 = 0 \text{ for the symmetric singularity,} \tag{3.6}$$

with ν^* being the fermionic Matsubara frequency where the localized divergence is located and $B_c = \frac{U}{2}\sqrt{\frac{-1+3e^{\beta U/2}}{1+e^{\beta U/2}}}$. In Fig. 3.1 the divergence lines for a vertex at $\omega = 0$ in the HA at half filling are shown, where the red lines are the antisymmetric divergence in the charge channel and the orange lines are the symmetric divergence that simultaneous occur in the charge and the pairing channel.
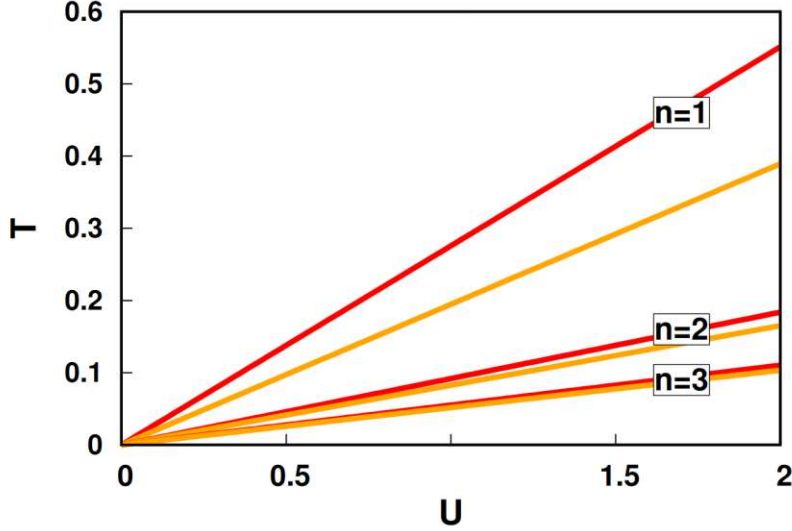
Figure 3.1: The lines where the irreducible vertex function of the HA diverges at half filling are shown: the red lines correspond to divergences in the charge channel associated to a frequency antisymmetric eigenvector, while the orange lines indicate the divergences that simultaneous occur in the charge and the pairing channel, associated to symmetric eigenvectors. n defines the positive Matsubara frequency where the antisymmetric eigenvector is localized $\nu^* = (2n-1)\pi/\beta$. Figure from [17].

Further, it is often useful to use the fact that a complex and symmetric matrix can be diagonalized by a complex orthogonal transformation, if and only if each eigenspace of the matrix has an orthonormal basis, i.e. no eigenvector that is *"quasi-null"* (see below) needs to be included in the basis itself [41]. The inner product and the induced Euclidean quasi-norm are defined as

$$\langle u, v \rangle := u^T \cdot v = \sum_i^n u_i v_i \tag{3.7}$$

and

$$\|u\|_T^2 := u^T \cdot u. \tag{3.8}$$

We recall that a vector is "quasi-null" if $\|u\|_T^2 = 0$ but $u \neq 0$. The only points in the phase space where we have quasi-null vectors in our basis are at the exceptional points [42] that will be excluded from the following analysis. Further, the usual norm that is used for complex vector spaces will be denoted by $\|u\|_\dagger^2 = u^\dagger \cdot u$.

This complex orthogonal transformation turns out to be particularly useful since the eigenvectors normalized in such a way **(i)** preserve symmetry properties regarding frequency even out of ph-symmetry and **(ii)** are orthogonal to each other regarding the scalar product defined in Eq. (3.7).

For a centro-hermitian matrix χ with eigenvector v and eigenvalue λ (either real or element of a

complex conjugate pair) it holds that

$$\chi v = \lambda v \Leftrightarrow \chi J v^* = \lambda^* J v^*. \tag{3.9}$$

From Eq. (3.9) follows that for a complex conjugate pair of eigenvalues, i.e. λ_α and $\lambda_{\alpha'} = \lambda_\alpha^*$, the relation

$$\text{if } \lambda_\alpha \in \mathbb{C}\colon \ \exists v_{\alpha'} = J v_\alpha^* \text{ with } \lambda_{\alpha'} = \lambda_\alpha^* \tag{3.10}$$

between the eigenvectors v_α and $v_{\alpha'} = J v_\alpha^*$ of this complex conjugate pair holds.

For non-degenerate[1] *real* eigenvalues Eq. (3.9) implies that v is linearly dependent on $J v^*$, e.g. $v = \gamma J v^*$ with $\gamma \in \mathbb{C}$. Using the usual norm $\|.\|_\dagger$ and enforcing $\|v\|_\dagger = 1$ we get the additional constraint of $|\gamma| = 1$. In the specific case of particle-hole symmetric systems, where we can restrict ourselves to real vector spaces, it holds $\gamma = \pm 1$. On the other hand, by adopting the quasi norm $\|.\|_T$ and enforcing $\|v\|_T = 1$ one gets $\gamma = \pm 1$, even when the restriction to particle-hole symmetry is lifted. Hence, in this case, one finds $v = \pm J v^*$, which means the vector has either a symmetric real part with antisymmetric imaginary part or vice versa. Therefore, we can state in general that:

$$\lambda_\alpha \in \mathbb{R} \text{ and non-degenerate} \ \Rightarrow v_\alpha = \gamma J v_\alpha^* \text{ with } |\gamma| = 1$$
$$\text{if } \|v_\alpha\|_\dagger = 1\colon \ \gamma \in \mathbb{C} \tag{3.11}$$
$$\text{if } \|v_\alpha\|_T = 1\colon \ \gamma \in \mathbb{R}.$$

In practice, this means that the eigenvectors of complex conjugate pairs are related to each other via $v_\alpha = J v_{\alpha'}^*$ and the eigenvectors of real eigenvalues are linearly dependent on $J v^*$ with $v = \gamma J v^*$. Further, important information has been joined recent literature by exploiting, an exact mapping that links the local 2-particle quantities of the half filled (ph-symmetric) attractive ($U < 0$) and repulsive ($U > 0$) model [11]. In particular, this mapping was then used to obtain the divergences lines of the attractive Hubbard model (solved with DMFT) from the corresponding ones in the repulsive model. It was found that only the symmetric vertex divergences are transformed under the mapping, while the antisymmetric divergences are invariant. The corresponding map of divergence lines, extended to $U < 0$, can be seen in Fig. 3.2.

---

[1]Note that non-degenerate is just a sufficient condition but not a necessary, therefore also an eigenvector with a real degenerate eigenvalue can possess the discussed symmetry. In fact, we see (empirically) that also real and degenerate eigenvalues have the discussed symmetry.
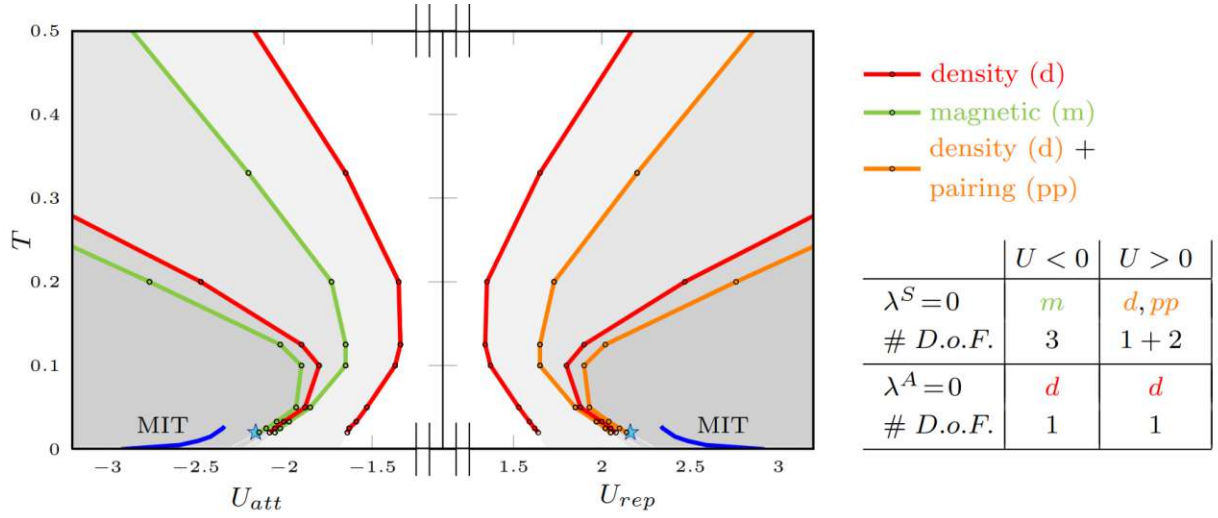
Figure 3.2: Vertex divergence lines at half filling for the Hubbard model solved with DMFT. Divergences are shown for repulsive and attractive interaction. The lines in the attractive sector, which have been explicitly computed in DMFT, can also be obtained from the lines in the repulsive sector by using the derived mapping for half filling. Further, the mapped degrees of freedom are shown, where $\lambda^{A/S}$ means (anti-)symmetric eigenvector. Figure taken from [11].

The mapping in Ref. [11] is derived by using a partial (local) particle-hole transformation, or Shiba transformation [43], where the $\downarrow$–spin is transformed as $c_\downarrow \to c_\downarrow^\dagger$ and $c_\downarrow^\dagger \to c_\downarrow$ while the $\uparrow$–spin is not affected by the transformation[2].

Additional to the (local) spin operator $\hat{\boldsymbol{S}}$ with the components

$$S_x = \frac{1}{2}(c_\uparrow^\dagger c_\downarrow + c_\downarrow^\dagger c_\uparrow), \tag{3.12}$$

$$S_y = \frac{1}{2i}(c_\uparrow^\dagger c_\downarrow - c_\downarrow^\dagger c_\uparrow), \tag{3.13}$$

$$S_z = \frac{1}{2}(c_\uparrow^\dagger c_\uparrow - c_\downarrow^\dagger c_\downarrow) \tag{3.14}$$

we can define a (local) pseudospin operator $\hat{\boldsymbol{S}}_p$ with the components

$$S_{p,x} = \frac{1}{2}(c_\uparrow^\dagger c_\downarrow^\dagger + c_\downarrow c_\uparrow), \tag{3.15}$$

$$S_{p,y} = \frac{1}{2i}(c_\uparrow^\dagger c_\downarrow^\dagger - c_\downarrow c_\uparrow), \tag{3.16}$$

$$S_{p,z} = \frac{1}{2}(c_\uparrow^\dagger c_\uparrow + c_\downarrow^\dagger c_\downarrow - 1). \tag{3.17}$$

Evidently, the Shiba transformation of the spin $\hat{\boldsymbol{S}}$ is the pseudospin $\hat{\boldsymbol{S}}_p$. Further, one can show that the spin and pseudospin are independent of each other as each component of the spin operator

---

[2]Note that the transformation can be also defined for non-local lattice problems by including a factor $(-1)^i$ in the transformation, where i is the lattice side. Here, we will only consider the local Shiba transformation.

commutes with any component of the pseudospin operator [26].

The pseudospin is physically interpreted as follows: $\mathcal{S}_{p,x}$ and $\mathcal{S}_{p,y}$ correspond to local Cooper pair operator, which describe the order parameter of a strong-coupling (Bose-Einstein-like) superconductor, and $\mathcal{S}_{p,z}$ describes the deviation of the density from half filling.

Normally, if one speaks about SU(2)-symmetric systems, what is meant is that the Hamiltonian of the system commutes with an arbitrary rotation generated by the spin operator (see Eq. (2.11)). Further, one can show that, in the perfect *particle-hole symmetric* case, the Hamiltonian commutes with any rotation generated by the *pseudospin* operator [26].

Hence, for systems that exhibit a symmetry under rotations generated by spin *and* pseudospin, e.g. a system that possesses the usual SU(2)-symmetry *and* is particle-hole symmetric, one has two independent SU(2)-algebras. The spin algebra SU(2)$_\text{S}$ and the pseudospin algebra SU(2)$_\text{P}$. Combining these SU(2)-algebras leads to $SO(4) \simeq (SU(2)_S \times SU(2)_P)/\mathbb{Z}_2$ [26], therefore we can refer to these systems as SO(4)-symmetric.

3.2 Misleading convergence

In Refs. [18, 20] it was found that the self-consistent perturbation theory described in section 2.1.3 can converge to unphysical solutions. This possibility of multiple solutions is due to the intrinsic multivaluedness of the LW functional. In Ref. [20], this remarkable feature of the many-body-theories is investigated for the Hubbard Atom at half filling by means of an iterative scheme that mimics the convergence of the self-consistent perturbation theory. The difference to the standard self-consistent perturbation theory is that the authors keep the values of the full Green's function G (which is known in the HA) fixed instead of the non-interacting Green's function G_0. Their scheme starts from a guess $G_0^{(n=0)}$ and finds a certain $G^{(n)}[G_0^{(n)}]$ using an interaction-expansion continuous-time quantum Monte Carlo solver. The iterative procedure is defined by the relation:

$$[G_0^{(n+1)}]^{-1} = [G_0^{-1}]^{(n)} + \left(G_{\text{exact}}^{-1} - \left[G^{(n)}[G_0^{(n)}] \right]^{-1} \right), \tag{3.18}$$

The parameters at which this iterative procedure, which corresponds to self-consistent perturbation theory, ceases to converge to the physical solution exactly corresponds to the parameters at which the first divergence of the irreducible vertex in the charge channel takes place. Remarkably, for U values higher than the U value of the first vertex divergence in the charge channel, the scheme still converges, but to an unphysical solution. The convergence of this scheme (named scheme A in Fig. 3.3) can be seen in Fig. 3.3.
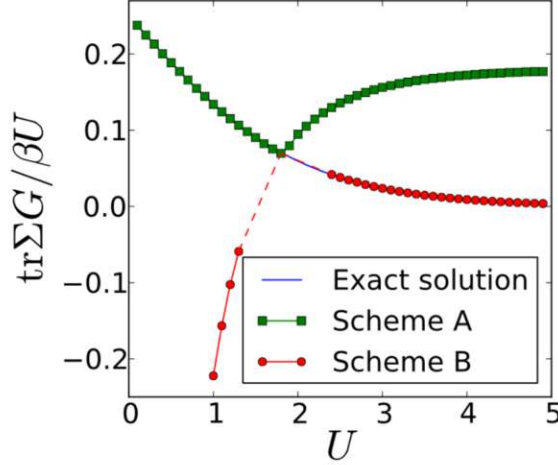
Figure 3.3: Misleading convergence of the schemes in Eq. (3.18) for the Hubbard Atom at half filling. Scheme A converges to the exact solution for small U and scheme B for large U. Figure taken from [20].

Further, an *ad hoc* scheme, called scheme B, has been developed in Ref. [20]. Scheme B reads

$$[G_0^{(n+1)}]^{-1} = [G_0^{(n)}]^{-1} \pm \left(G_{\text{exact}}^{-1} - \left[G^{(n)}[G_0^{(n)}] \right]^{-1} \right), \tag{3.19}$$

where the $\pm$ means that minus is used for the lowest Matsubara frequency and plus is used for all other Matsubara frequencies. By using scheme B the authors of Ref. [20] managed to obtain a convergence to the physical solution in the complementary region of the phase-diagram, i.e., for U values higher than the U value of the first divergence in the charge channel, as it can be seen in Fig. 3.3.

At the present stage it is unclear, why the scheme B modifies the convergence like that. One could speculate that the *ad hoc* sign change made in Eq. (3.19) works due to the fact that the first vertex divergence in the charge channel is localized on the lowest Matsubara frequencies [5]. It is not known, however, whether scheme B can be generalized to become applicable to other cases than the Hubbard Atom.

3.3 Link between vertex divergences and misleading convergence

In Ref. [12] a connection between the two manifestations of the breakdown of perturbation theory, discussed in the previous sections, is made. The intrinsic multivaluedness of the LW functional [20] is explicitly accounted for by considering a functional $\mathcal{F}[G_0^{-1}; U, \nu]$ that equals G when evaluated at the functions $G_0^{(1)}$ or $G_0^{(2)}$. Further, it holds that

$$\chi_{\text{c}}^{\nu\nu'\omega=0} = \left. \frac{\delta \mathcal{F}[G_0^{-1}; U, \nu]}{\delta G_0^{-1}(\nu')} \right|_{G_0 = G_{0,\text{physical}}}. \tag{3.20}$$

The formal derivation in [12] is obtained via the following steps. First, it is assumed that $G_0^{(1)} = G_0^{(2)}$ at $U = U_0$, then by means of a functional Taylor expansion of $\mathcal{F}$ it is demonstrated that the irreducible vertex function in the charge channel must diverge at U_0. This finding links the crossing of two solutions with the occurrence of vertex divergences in the charge channel. A heuristic picture of this crossing of different LW solutions is shown in Fig. 3.4, which sketch the situation if G and G_0 would just be real numbers and $G(G_0)$ a function of G_0. The point of crossing is a minimum, so it holds that $\frac{\partial G}{\partial G_0} = 0$ and therefore $\Gamma = \frac{\partial \Sigma}{\partial G} = \frac{\partial \Sigma}{\partial G_0} \frac{\partial G_0}{\partial G} \to \infty$.
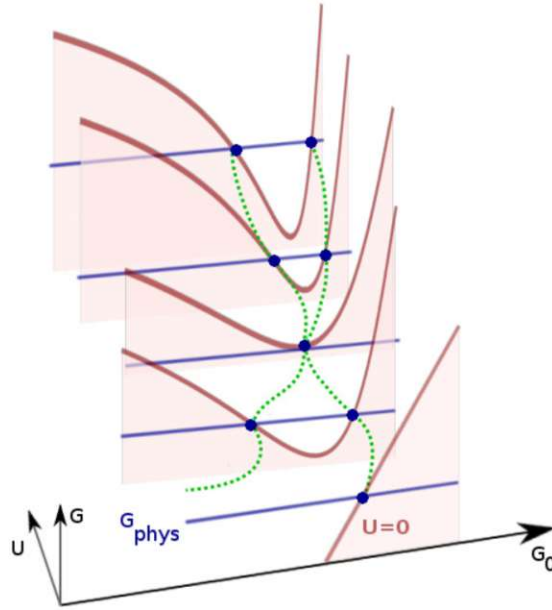
Figure 3.4: Heuristic picture for the crossing of two G_0 functions, both corresponding to the physical G_{phys}. The blue lines mark the value of the physical Green's function for different U, the red lines show the function $G(G_0)$ for different U and the green line describes the evolution of the two G_0 functions for different interactions U. Figure taken from [12].

Beyond the formal implications of the general relation derived in [12] it is interesting, on a more practical point of view, to recall that the crossing of LW-solutions has also been directly associated with the onset of misleading convergence of the bold (self-consistent) perturbation expansion[3] [17, 18, 20–22, 24, 25]. Hence, the occurrence of the first divergence of Γ_{c} with progressively increasing $|U|$ should represent a hard border for the convergence of the self-consistent perturbation resummation to the physical solution.

---

[3]Exactly in the cases of the simplest zero space-time dimensional model [21, 22, 24] and empirically (with no exception known) in the general case of many-electron models with on-site interaction.

3.4 Open questions

As the largest part of the previous investigations was restricted to high symmetry cases, where the rather special condition of particle-hole symmetry is fulfilled, a natural extension would be to lift such a restriction. This represents the main goal of the present thesis. Our study aims to address several key questions, emphasizing the specific motivation behind each one. These questions are listed below:

- How can the mapping of 2-particle quantities between repulsive and attractive models of Ref. [11] be extended beyond SO(4)-symmetry?

  Motivation: Extending the mapping would allow a better understanding of the underlying physics and, on a more practical note, one would be able to investigate a larger parameter space with reduced numerical effort.

- How do the vertex divergences behave beyond particle-hole symmetry?

  Motivation: By the means of this analysis one could identify the non-perturbative regions out of half filling and investigate whether the non-perturbation region remains always bounded by vertex divergences when the condition of particle-hole symmetry is lifted.

- How does the $T = 0$ limit behave?

  Motivation: Clarifying the $T = 0$ limit would improve the understanding between the ground state properties of the system and the non-perturbative breakdown. Further, there are computational methods that can mostly be used for $T = 0$ [44, 45].

- How does the misleading convergence of self-consistent perturbation theory happen beyond particle-hole symmetry?

  Motivation: The investigation of the misleading convergence would answer the very practical and important question, in which regions of the phase space the bold diagrammatic summation is still applicable. Further the question, if only vertex divergences lead to misleading convergence, can be addressed. Moreover, investigating the way in which the perturbation theory breaks down is a first step towards the derivation of a formal link between vertex properties and misleading convergence in the sense of Ref. [12] that goes beyond the implicit assumption of particle-hole symmetry.

Chapter 4

Results: Vertex divergences in Hubbard Atom

In this chapter, the results obtained for the first manifestation of the perturbative breakdown, i.e. the divergence of the irreducible vertex, are presented. Specifically, the vertex divergences in the Hubbard Atom (HA) beyond particle-hole symmetry are investigated along the following steps: First, an exact mapping that links the local 2-particle quantities in the SU(2)-symmetric out-of-half-filling case to the SU(2)-broken half filling case is derived and discussed. Then, a precise determination of the vertex divergences occurring at finite temperature in the SU(2)-symmetric HA beyond particle-hole symmetry is presented for the whole phase space, including repulsive as well as attractive interaction. Exploiting the universality of this result, the limit $T \to 0$ is then thoroughly investigated. Finally, the introduced mapping is used to obtain the vertex divergences of the HA in presence of a finite magnetic field at half filling, extending the previous analysis to the whole phase space of the HA where either spin or pseudospin symmetry is broken.

4.1 Mapping of local 2-particle quantities beyond SO(4)-symmetry

In section 3.1 the mapping of local 2-particle quantities is investigated when the two Hamiltonians linked by this mapping exhibit a SO(4) symmetry, e.g. the system is invariant under rotations in spin and pseudospin space. In this section the mapping is extended to the case where either the spin or the pseudospin symmetry is broken on one side of the mapping.

In order to map the local 2-particle quantities (for bosonic frequency $\omega = 0$) from the SU(2)-symmetric[1] out of half filling case to the SU(2)-broken half filling case we start with a partial particle-hole, or Shiba, transformation [43]:

$$c_\uparrow \to c_\uparrow, c_\uparrow^\dagger \to c_\uparrow^\dagger, c_\downarrow \to c_\downarrow^\dagger \text{ and } c_\downarrow^\dagger \to c_\downarrow. \tag{4.1}$$

---

[1]By SU(2)-symmetric we mean symmetric under rotation in spin (and *not* pseudospin) space, unless explicitly stated otherwise.

The effect of such a transformation becomes more transparent when using the particle-hole symmetric form of the corresponding Hamiltonian, as it is stated in the first line of Eq. (4.2)

$$
\begin{aligned}
H &= -\delta\mu(n_\uparrow + n_\downarrow) - h(n_\uparrow - n_\downarrow) + U(n_\uparrow - 1/2)(n_\downarrow - 1/2) \\
&= -\mu(n_\uparrow + n_\downarrow) - h(n_\uparrow - n_\downarrow) + Un_\uparrow n_\downarrow + \text{const.},
\end{aligned}
\tag{4.2}
$$

with $\delta\mu = \mu - U/2$.

Performing the Shiba transformation for this Hamiltonian leads to

$$
\begin{aligned}
H(U, \delta\mu, h) &= -\delta\mu(n_\uparrow + n_\downarrow) - h(n_\uparrow - n_\downarrow) + U(n_\uparrow - 1/2)(n_\downarrow - 1/2) \\
&\overset{\text{Shiba}}{\longleftrightarrow} -\delta\mu(n_\uparrow - n_\downarrow) - h(n_\uparrow + n_\downarrow) - U(n_\uparrow - 1/2)(n_\downarrow - 1/2) = H(-U, h, \delta\mu).
\end{aligned}
\tag{4.3}
$$

As it can be seen in Eq. (4.3) the Shiba transformation corresponds to exchanging the values of $\delta\mu$ and h *and* changing the sign of U. In this thesis, the specific transformation $H(U, \delta\mu, 0) \leftrightarrow H(-U, 0, h)$ with $\delta\mu = h$ is considered. Hence, the mapping is from a Hubbard Atom (or local problem) out of half filling without external magnetic field to the same system at half filling in presence of a magnetic field *and* a sign flip in the interaction.

For the physical susceptibility the effect of the Shiba transformation is well known: The charge susceptibility gets mapped into the longitudinal spin susceptibility while the pairing susceptibility is mapped into the transverse spin susceptibility [43]. The action of the mapping is much more complicated for the generalized susceptibilities, especially for the charge and longitudinal spin channel, as we will see in the following.

Looking at the definition of the generalized susceptibility Eq. (4.4) we can calculate how the generalized susceptibilities transform under the Shiba transformation[2]

$$
\begin{aligned}
\chi_{\sigma\sigma'}^{\nu\nu'\omega} = \int_0^\beta & d\tau_1 d\tau_2 d\tau_3 \, e^{-i\nu\tau_1} e^{i(\nu+\omega)\tau_2} e^{-i(\nu'+\omega)\tau_3} \\
& \left(\langle T_\tau c_\sigma^\dagger(\tau_1) c_\sigma(\tau_2) c_{\sigma'}^\dagger(\tau_3) c_{\sigma'}(0) \rangle - \langle T_\tau c_\sigma^\dagger(\tau_1) c_\sigma(\tau_2) \rangle \langle T_\tau c_{\sigma'}^\dagger(\tau_3) c_{\sigma'}(0) \rangle \right),
\end{aligned}
\tag{4.4}
$$

which leads to

$$
\chi_{\uparrow\uparrow,\text{h}}^{\nu\nu'} = \chi_{\uparrow\uparrow,\delta\mu}^{\nu\nu'}, \quad \chi_{\uparrow\downarrow,\text{h}}^{\nu\nu'} = -\chi_{\uparrow\downarrow,\delta\mu}^{\nu-\nu'}, \quad \chi_{\downarrow\uparrow,\text{h}}^{\nu\nu'} = -\chi_{\downarrow\uparrow,\delta\mu}^{-\nu\nu'} \text{ and } \chi_{\downarrow\downarrow,\text{h}}^{\nu\nu'} = \chi_{\downarrow\downarrow,\delta\mu}^{-\nu-\nu'},
\tag{4.5}
$$

where the subscript $\delta\mu$ marks the system out of half filling without magnetic field, while the subscript h corresponds to the case of finite magnetic field and half filling.

We recall that the charge and spin channel are decoupled in presence of SU(2)-symmetry [28] and therefore the matrix $\chi_{\delta\mu}$ is block diagonal

---

[2]if no explicit ph or pp index is present the quantity is always expressed in ph-notation and $\chi^{\nu\nu'} := \chi^{\nu\nu'\omega=0}$

$$\chi_{\delta\mu} = \begin{pmatrix} \chi_{\mathrm{c},\delta\mu} & \mathbb{0} \\ \mathbb{0} & \chi_{\mathrm{s},\delta\mu} \end{pmatrix}. \tag{4.6}$$

When SU(2)-symmetry is broken, instead, charge and longitudinal spin channel get coupled by the matrices χ_{cs} and χ_{sc}. Therefore, χ_h is no longer block diagonal for finite h:

$$\chi_h = \begin{pmatrix} \chi_{\mathrm{c,h}} & \chi_{\mathrm{cs,h}} \\ \chi_{\mathrm{sc,h}} & \chi_{\mathrm{s,h}} \end{pmatrix}. \tag{4.7}$$

The matrices in Eq. (4.7) (defined in Ref. [46]) can be represented with the SU(2)-symmetric quantities by using the transformations in Eq. (4.5)

$$\chi_{\mathrm{c,h}}^{\nu\nu'} = \frac{1}{2}(\chi_{\uparrow\uparrow,\mathrm{h}}^{\nu\nu'} + \chi_{\downarrow\downarrow,\mathrm{h}}^{\nu\nu'} + \chi_{\uparrow\downarrow,\mathrm{h}}^{\nu\nu'} + \chi_{\downarrow\uparrow,\mathrm{h}}^{\nu\nu'}) = \mathrm{Re}(\chi_{\uparrow\uparrow,\delta\mu}^{\nu\nu'}) - \mathrm{Re}(\chi_{\uparrow\downarrow,\delta\mu}^{-\nu\nu'}), \tag{4.8}$$

$$\chi_{\mathrm{s,h}}^{\nu\nu'} = \frac{1}{2}(\chi_{\uparrow\uparrow,\mathrm{h}}^{\nu\nu'} + \chi_{\downarrow\downarrow,\mathrm{h}}^{\nu\nu'} - \chi_{\uparrow\downarrow,\mathrm{h}}^{\nu\nu'} - \chi_{\downarrow\uparrow,\mathrm{h}}^{\nu\nu'}) = \mathrm{Re}(\chi_{\uparrow\uparrow,\delta\mu}^{\nu\nu'}) + \mathrm{Re}(\chi_{\uparrow\downarrow,\delta\mu}^{-\nu\nu'}), \tag{4.9}$$

$$\chi_{\mathrm{cs,h}}^{\nu\nu'} = \frac{1}{2}(\chi_{\uparrow\uparrow,\mathrm{h}}^{\nu\nu'} - \chi_{\downarrow\downarrow,\mathrm{h}}^{\nu\nu'} - \chi_{\uparrow\downarrow,\mathrm{h}}^{\nu\nu'} + \chi_{\downarrow\uparrow,\mathrm{h}}^{\nu\nu'}) = i\mathrm{Im}(\chi_{\uparrow\uparrow,\delta\mu}^{\nu\nu'}) - i\mathrm{Im}(\chi_{\uparrow\downarrow,\delta\mu}^{-\nu\nu'}), \tag{4.10}$$

$$\chi_{\mathrm{sc,h}}^{\nu\nu'} = \frac{1}{2}(\chi_{\uparrow\uparrow,\mathrm{h}}^{\nu\nu'} - \chi_{\downarrow\downarrow,\mathrm{h}}^{\nu\nu'} + \chi_{\uparrow\downarrow,\mathrm{h}}^{\nu\nu'} - \chi_{\downarrow\uparrow,\mathrm{h}}^{\nu\nu'}) = i\mathrm{Im}(\chi_{\uparrow\uparrow,\delta\mu}^{\nu\nu'}) + i\mathrm{Im}(\chi_{\uparrow\downarrow,\delta\mu}^{-\nu\nu'}), \tag{4.11}$$

where it is used that the generalized susceptibilities are centro-hermitian ($\chi_{\sigma\sigma'}^{-\nu-\nu'} = (\chi_{\sigma\sigma'}^{\nu\nu'})^*$) and the susceptibilities with $\delta\mu$ index are SU(2)-symmetric ($\chi_{\sigma\sigma',\delta\mu}^{\nu\nu'} = \chi_{-\sigma-\sigma',\delta\mu}^{\nu\nu'}$).

In order to understand the mapping of the full generalized susceptibilities χ_h and $\chi_{\delta\mu}$ it is useful to introduce the orthogonal transformation Q [11]

$$Q = \frac{1}{\sqrt{2}} \begin{pmatrix} \mathbb{1} & -J \\ \mathbb{1} & J \end{pmatrix} \quad \text{with} \quad J = \begin{pmatrix} & & 1 \\ & \cdot^{\cdot^{\cdot}} & \\ 1 & & \end{pmatrix}. \tag{4.12}$$

The transformation Q applied to a centro-hermitian matrix χ_{CH} separates the parts that couple to symmetric $\chi_{\mathcal{S}}$ respectively antisymmetric $\chi_{\mathcal{A}}$ vectors, in blocks

$$Q\chi_{CH}Q^T = \begin{pmatrix} \chi_{\mathcal{A}}' & i\chi_{\mathcal{S}}'' \\ i\chi_{\mathcal{A}}'' & \chi_{\mathcal{S}}' \end{pmatrix}. \tag{4.13}$$

To understand why these blocks are antisymmetric ($\mathcal{A}$) or symmetric ($\mathcal{S}$) see appendix A.2. Further, defining two transformations for the space of the full generalized susceptibilities

$$\mathcal{Q} = \begin{pmatrix} Q & \mathbb{0} \\ \mathbb{0} & Q \end{pmatrix} \quad \text{and} \quad T = \begin{pmatrix} \mathbb{1} & \mathbb{0} & \mathbb{0} & \mathbb{0} \\ \mathbb{0} & \mathbb{0} & \mathbb{0} & \mathbb{1} \\ \mathbb{0} & \mathbb{0} & \mathbb{1} & \mathbb{0} \\ \mathbb{0} & \mathbb{1} & \mathbb{0} & \mathbb{0} \end{pmatrix} \tag{4.14}$$

we show that

$$\mathcal{Q}\chi_h\mathcal{Q}^T = T\mathcal{Q}\chi_{\delta\mu}\mathcal{Q}^T T, \tag{4.15}$$

see appendix A.2 for the calculation.

Hence, if $v_{\delta\mu}$ is an eigenvector of $\chi_{\delta\mu}$, then consequently $T\mathcal{Q}v_{\delta\mu}$ is an eigenvector of χ_h. We find that the symmetric part of the eigenvector $v_{\delta\mu}$ is mapped from the charge to the spin sector or vice versa, and the antisymmetric part is invariant under the transformation.

Further, it holds that

$$\chi_{S_x,h}^{\nu\nu'} = \chi_{S_y,h}^{\nu\nu'} = \chi_{\uparrow\downarrow,h}^{\nu\nu'} + \chi_{\downarrow\uparrow,h}^{\nu\nu'} = \chi_{\text{pp},\uparrow\downarrow,\delta\mu}^{\nu-\nu'} - \chi_{0,\text{pp}}^{\nu\nu'} = \chi_{\text{pair},\delta\mu}^{\nu\nu'}, \tag{4.16}$$

see appendix A.2 for the calculations.

This derivation, which extends the results of [11] beyond SO(4)-symmetry, is useful for several reasons. First, it allows us to directly obtain the 2-particle quantities with external magnetic field at half filling from the corresponding 2-particle quantities out of half filling without magnetic field (or vice versa). Further, it clarifies which part of the susceptibilities are mapped and which are invariant under this transformation. Finally, it can be also used to obtain the divergence lines in both sectors by just calculating one sector as it is done in section 4.4.

4.2 Vertex divergences out of half filling

In this section the vertex divergences at transfer frequency $\omega = 0$ for the Hubbard Atom out of half filling without magnetic field are calculated. As it is already stated in section 3.1 vertex divergences correspond to a vanishing eigenvalue in the generalized susceptibility expressed as a matrix in fermionic Matsubara frequency space. When particle-hole symmetry is fulfilled the generalized susceptibilities in the ph-channel are real and symmetric (hence hermitian), therefore they only have real eigenvalues. By breaking particle-hole symmetry, e.g. by varying the chemical potential μ, the static generalized susceptibilities in ph-channel (and $\sigma\sigma'$ spin channel) become centro-hermitian matrices[3], which have either real or complex conjugate pairs as eigenvalues [39]. Since the eigenvalues of centro-hermitian matrices can be complex a sign change of the real part of an eigenvalue can occur continuously without the necessity of crossing the origin of the complex

---

[3]The pp-channel, instead, is not affected by breaking the ph-symmetry Tab. 3.1.

plane: The eigenvalues can get negative real parts also by crossing the imaginary axis with a finite value of the imaginary part. In this context, we define the occurrence of a complex conjugate pair of eigenvalues with vanishing real part but finite imaginary part as *pseudo-divergences*. Evidently, the BSE remains invertible in this case, but pseudo-divergences appear to be nonetheless important due to their impact on the self-consistent perturbation theory, as we will see in chapter 5.

We start our analysis by investigating the Lehmann-representation of the generalized susceptibility[4]. Let us consider a model which depends on N parameters $\{\varepsilon_i\}|_{i=1}^N$, where all ε_i have the unit of energy. Of course, all energies of the corresponding many-body Hamiltonian will only depend on these parameters $\{E_j\} = \{E_j(\{\varepsilon_i\})\}$ and on the basis of dimensional considerations βE_j must only be dependent on the set $\{\beta \epsilon_i\}$ for all j.

Hence, by looking at the Lehmann-representation of the generalized susceptibility, we notice that, apart from an overall scaling of β^3, the generalized susceptibility can be expressed in terms of the parameter set $\{\beta E_i\}$. As a consequence, one finds that:

$$\chi_{\alpha_1,\alpha_2,\alpha_3,\alpha_4}^{\nu\nu'\omega}(\beta, \{\varepsilon_i\}) = \beta^3 f_{\alpha_1,\alpha_2,\alpha_3,\alpha_4}^{nn'm}(\{\beta\varepsilon_i\}), \tag{4.17}$$

where n, n' and m are the indices for ν, ν' and ω and α is a generic set of quantum numbers.

In the general case of the Hubbard Model with the three parameters μ, U, t we have a 4-dimensional parameter space $\{\beta, \mu, U, t\}$ that needs to be considered. On the basis of the above consideration, we can restrict ourselves to a 3-dimensional reduced parameter space $\{\beta\mu, \beta U, \beta t\}$ which can be investigated without losing any information about the model.

For this thesis we use the insight of Eq. (4.17) for the Hubbard Atom, we notice that we can reduce the 3-dimensional parameter space $\{\beta, \mu, U\}$ to a 2-dimensional parameter space $\{\beta\mu, \beta U\}$ without loosing any information about the system. We can therefore investigate a 2-dimensional parameter space instead of a 3-dimensional one without loosing any information about the system, as all information is present to the reduced phase space.

Based on the above considerations, we present our results for the position and the nature of the vertex divergences in the HA without magnetic field in this 2-dimensional parameter space $\{\beta\mu, \beta U\}$ by searching for vanishing eigenvalues, or for a vanishing real part of the eigenvalues in the case of pseudo-divergences, of the generalized susceptibility. To this aim, a discrete grid in the $(\delta\mu, U)$-space for constant β (for simplicity $\beta = 1$) is introduced, the generalized susceptibilities are calculated on this grid, and then the eigenvalues of these susceptibilities are calculated and searched for vanishing eigenvalues or vanishing real parts. Note that we define $\delta\mu = \mu - U/2$ instead of μ to make the plot symmetric around half filling.

Before discussing the results, let us clarify the semantics. We classify a divergence as "symmetric/antisymmetric" if the corresponding eigenvector of the generalized susceptibility, which has a vanishing eigenvalue, has a symmetric/antisymmetric real part and an antisymmetric/symmetric imaginary part, provided that we use the norm Eq. (3.8) to normalize the eigenvectors. The

---

[4]See [47] for the exact formula for local susceptibilities, but note that the presented arguments also apply for non-local susceptibilities with the only difference that the σ index becomes a σ, k index.

notation used to display the (pseudo-)divergences is the phase space is the following: Solid lines mark divergences and dashed lines mark pseudo-divergences. For different channels we use different colors. The adopted color coding, which is consistent with the existing literature, is: For a vertex (pseudo-)divergence in the charge channel: red, pairing channel: yellow, spin channel: bluish green.

The calculated vertex divergences and pseudo-divergences for the Hubbard Atom without external magnetic field are shown in Fig. 4.1, where the known divergences (see Figs. 3.1, 3.2) at half filling has been marked with colored dots (charge: red, charge and pairing simultaneously: orange, spin: bluish green). In the 2-dimensional parameter space the red dots mark antisymmetric divergences in the charge channel and the orange dots mark symmetric divergences in the charge and pairing channel simultaneously. Then the mapping derived in Ref. [11] can be used to get the corresponding divergences in the attractive ($U < 0$) sector at half filling: The antisymmetric divergences in the charge channel are invariant, and the symmetric divergences get mapped to the spin channel.

Starting from the known results at particle-hole symmetry, we investigate the development of the divergences lines without particle-hole symmetry.

For the repulsive sector we find that, by increasing/decreasing $\delta\mu$, an antisymmetric and a symmetric divergence line in the charge channel "meet" at an exceptional point (EP)[5] out of half filling and then form a pseudo-divergence line. Further, we find that, due to the lifting of perfect ph-symmetry, the symmetric divergence in the charge channel and pairing channel are no longer on top of each other, when going out of half filling. The charge divergences of the described structure look like ellipses in the phase space, as it can be seen in Fig. 4.1. Hence, we will call this structure, together with the attached pseudo-divergences and the pairing divergence, *loops*.

Note that the three loops shown in Fig. 4.1 are just the first three loop structures. Since in Refs. [5, 17] the authors find infinitely many divergences at half filling, we also have infinitely many loops for higher and higher U values.

---

[5]EPs are points where the algebraic multiplicity of an eigenvalue is bigger than the geometric multiplicity [42]
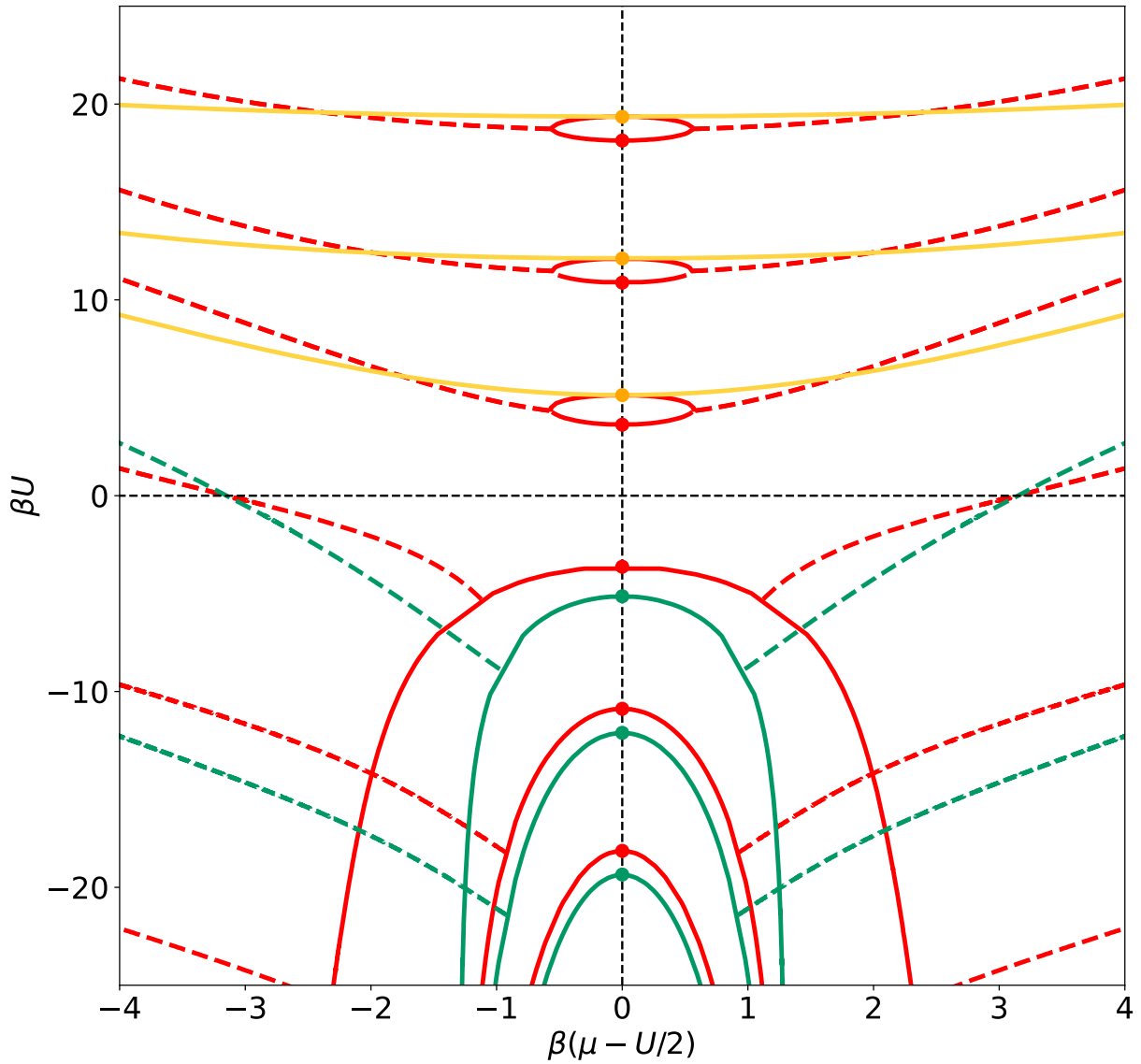
Figure 4.1: Vertex divergences and pseudo-divergences for the HA with broken ph-symmetry and without external magnetic field. Solid lines mark vertex divergences and dashed lines mark pseudo-divergences. The channel in which the (pseudo-)divergence appears is indicated by the color of the line: charge: red, pairing: yellow, spin: bluish green. The (pseudo-)divergences are plotted and calculated in the reduced parameter space $\{\beta\delta\mu, \beta U\}$, where $\delta\mu = \mu - U/2$ is used instead of μ to make the plot symmetric around half filling.

For a closer inspection, let us now considering a path with constant $\beta\delta\mu$ and increasing βU. We find that crossing a divergence corresponds to a real eigenvalue, in the generalized susceptibility, that goes from positive to negative. Hence, after crossing N divergence lines we have N negative real eigenvalues, of which $\lceil N/2 \rceil$ have antisymmetric eigenvectors and $\lfloor N/2 \rfloor$ have symmetric eigenvectors[6]. At higher values of $\delta\mu$, where we cross a pseudo-divergence and not a divergence,

---

[6]The notation symmetric/antisymmetric eigenvector is again used for eigenvector that have symmetric/antisymmetric real part.

we find that the crossing corresponds to a complex conjugate pair whose real part changes from positive to negative[7]. Therefore, after crossing N pseudo-divergences (that emerge from the loops), one finds $2N$ complex conjugate pairs with negative real parts.

In Figs. 4.2 to 4.4 we show the eigenvectors along the (pseudo-)divergence lines for the first loop structure for different $\beta\delta\mu$.
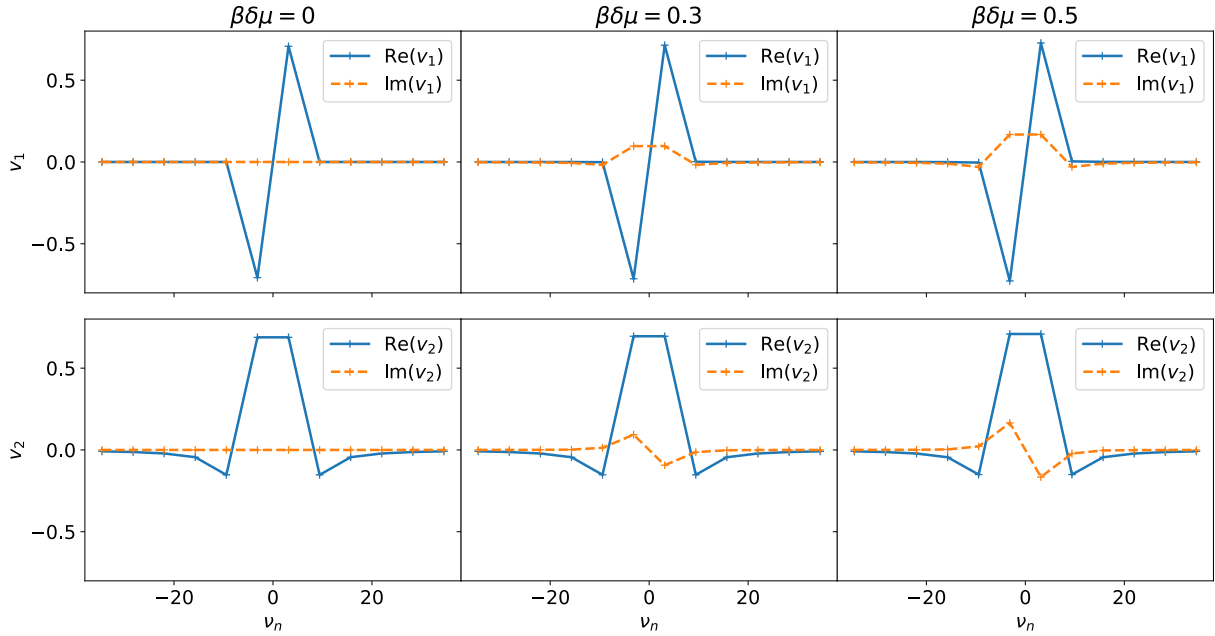
Figure 4.2: Upper row: Eigenvectors along the first antisymmetric divergence v_1.
Lower row: eigenvectors along the first symmetric divergence v_2. Both for different $\beta\delta\mu$ (the exceptional point is at $\beta\delta\mu = 0.6$). Vectors are normalized with $\|.\|_T$.

In Fig. 4.2 the eigenvectors in the charge channel that correspond to the divergences that form the first loop are shown. We find that the real antisymmetric/symmetric eigenvector at half filling acquire a symmetric/antisymmetric imaginary part out of half filling. The imaginary part increases for increasing values of $\beta\delta\mu$, e.g. by progressively approaching the value of $\beta\delta\mu = 0.6$, where the EP is located.

In Fig. 4.3 the eigenvector pairs along the first pseudo-divergence are shown for different $\beta\delta\mu$.

---

[7]Note that this only holds for pseudo-divergences that emerge from the loops. Considering the pseudo-divergences that cross the $U = 0$ axis, we find that this corresponds to a complex conjugate pair, whose real part changes from negative to positive along a path with increasing U.
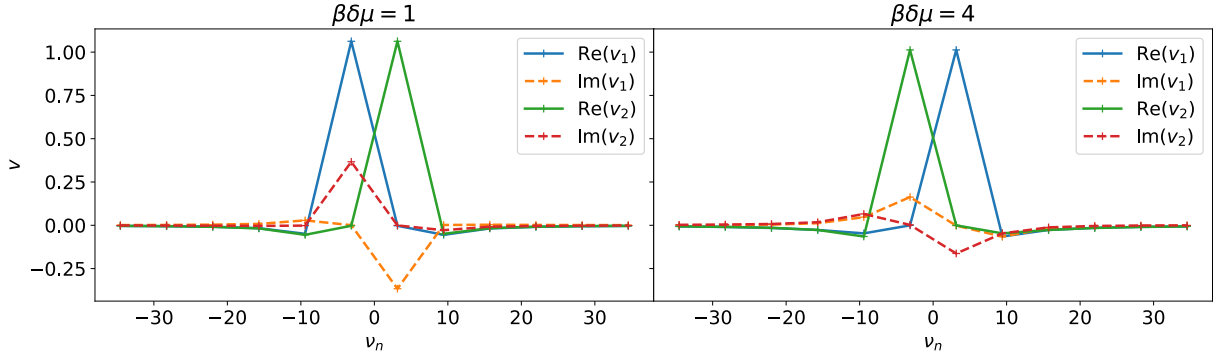
Figure 4.3: Eigenvectors along the first pseudo-divergence in the charge channel for different $\beta\delta\mu$. Vectors are normalized with $\|.\|_T$.

We find the expected behavior that the two eigenvectors associated to the pseudo-divergence are related to each other via $v_1 = Jv_2^*$ (see Eq. (3.10)).

Finally, in Fig. 4.4 the eigenvectors along the pairing channel of the first loop structure are shown for different $\beta\delta\mu$.
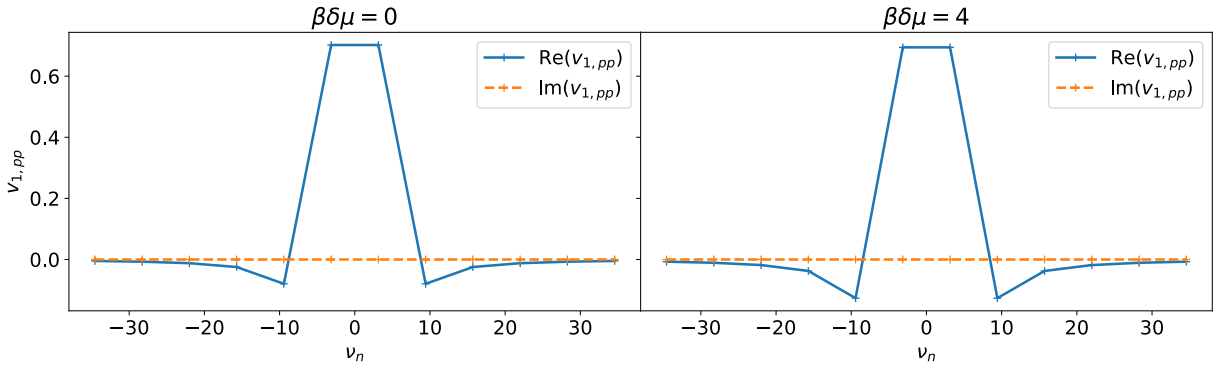
Figure 4.4: Eigenvector of the first divergence in the pairing channel for different $\beta\delta\mu$.

We note that eigenvectors in the pairing channel are real for any $\beta\delta\mu$, because breaking the ph-symmetry has no effect on the pairing channel and therefore χ_{pair} remains a real and symmetric matrix. Further, we find that the real and symmetric eigenvector of the pairing divergence does not change very much depending on $\beta\delta\mu$.

Making our analysis more quantitative, Figs. 4.2 to 4.4 show that all eigenvectors corresponding to the first loop structure are approximately localized at ν_1 and $-\nu_1$. This appears to be a general feature of the eigenvectors that are related to the divergences. So the eigenvectors of the Nth loop structure are approximately localized at ν_N and $-\nu_N$ (See Figs. A.1 to A.3 for the second loop structure).

Turing now to the study of the attractive sector, we find that the divergence lines show a completely different shape: They are disposed in a series of parabolas one inside the other, as it can be seen in Fig. 4.1. In the charge channel we only have antisymmetric divergences at half filling. An antisymmetric divergence line meets with a symmetric divergence one out of half filling at an EP, forming a pseudo-divergence afterward. The different structure compared to the divergences in the

repulsive sector reflects in a specific difference: Each symmetric divergence extends to $U \to -\infty$. The reason this happens is the following: There are no symmetric divergences at half filling, and therefore a symmetric and an antisymmetric divergence can not form a closed loop at difference with the repulsive sector.

In the spin channel we find nearly the same but with the difference that the spin channel has only symmetric divergences at half filling. This symmetric divergences meet at an exceptional point with an antisymmetric divergence that again extends to $U \to -\infty$. Hence, the charge and the spin channel exhibit the same structure but with the role of symmetric and antisymmetric divergences exchanged.

Further, we find that the Nth pseudo-divergences crosses the $U = 0$ axis at[8] $\beta\delta\mu = \beta\mu = \pm(2N-1)\pi$. This must be the same point for charge and spin channel, because these two channels coincide for $U = 0$, due to the absence of vertex corrections. After crossing $U = 0$ these pseudo-divergences reach into the repulsive sector.

Following the same steps made in the repulsive case, let us consider again a path with constant $\beta\delta\mu$ and decreasing βU (increasing $|\beta U|$). Going through an antisymmetric divergence corresponds to a real eigenvalue that goes from positive to negative. When looking at a path at higher $\beta\delta\mu$ where we cross pseudo-divergence, we find a complex conjugate pair of eigenvalues whose real part changes from positive to negative. Going to lower βU along this path, we get to an exceptional point where this complex conjugate pair of eigenvalues splits apart, and two real eigenvalues appear afterward. From this two eigenvalues the one with an antisymmetric eigenvector stays negative and the one with a symmetric eigenvector turns from negative to positive when crossing the symmetric divergence at even lower βU. Such a development can be seen in Fig. A.4 for the first pseudo-divergence and the first symmetric divergence in the charge channel.

For the spin channel the situation is nearly the same with the difference that again the role played by symmetric and antisymmetric divergence is interchanged.

Therefore, in the charge channel there are N negative real eigenvalues with antisymmetric eigenvectors inside the Nth parabola and $2N$ (real or complex) eigenvalues with negative real part inside the area bounded by the Nth symmetric divergence and the Nth pseudo-divergence lines. For the spin channel we have the same situation, but again with symmetric and antisymmetric divergences exchanged.

In Figs. 4.5 to 4.7 the eigenvectors along the first parabola are shown for charge and spin channel.

---

[8]This can be understood by calculating when the real part of $\chi_0^{\nu\nu'}(U = 0) = -\beta G_0^2(\nu)\delta_{\nu\nu'}$ vanishes
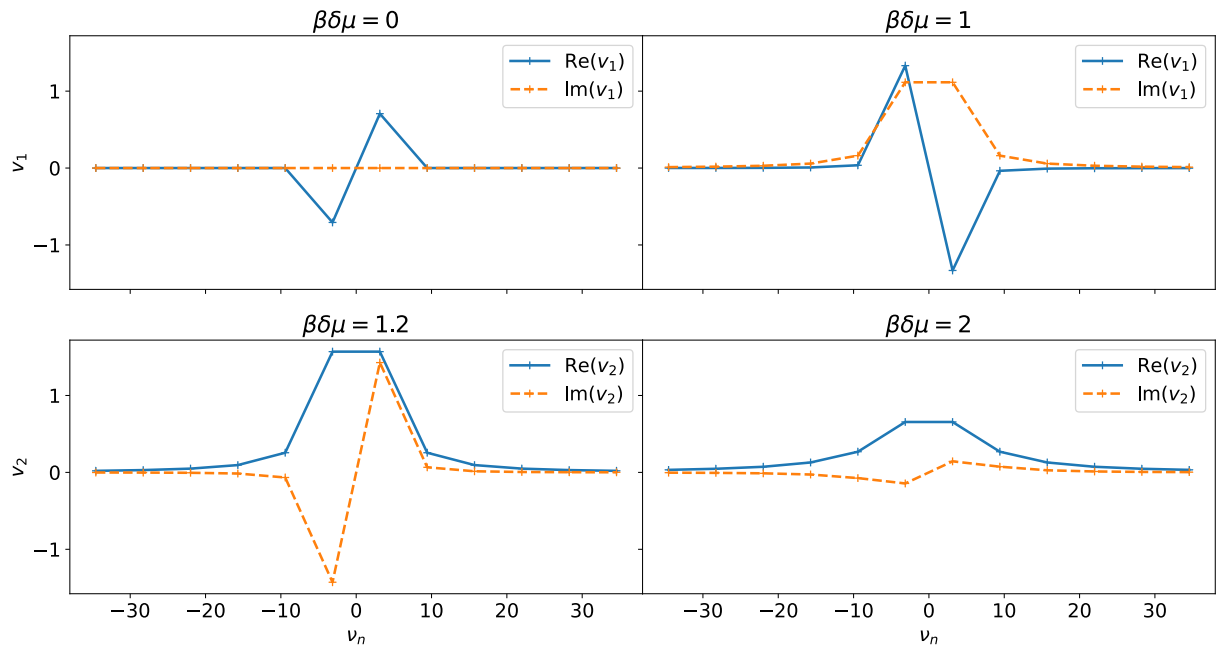
Figure 4.5: Eigenvectors along the first parabola of vertex divergences in the charge channel for different $\beta\delta\mu$. The exceptional point is at $\beta\delta\mu = 1.12$. Vectors are normalized with $\|\cdot\|_T$.

Looking at Fig. 4.5 we start with a real antisymmetric eigenvector at half filling ($\delta\mu = 0$), which gradually acquires a symmetric imaginary part by increasing $\beta\delta\mu$. This imaginary part gets larger when approaching the exceptional point, which is at $\beta\delta\mu = 1.12$. After the exceptional point, the eigenvector features a symmetric real part and an antisymmetric imaginary part, whereas the latter gets progressively smaller when moving away from the exceptional point.

For the first parabola in the spin channel (see Fig. 4.6) we find the same behavior, albeit with antisymmetric and symmetric divergences interchanged and an exceptional point at $\beta\delta\mu = 0.975$.
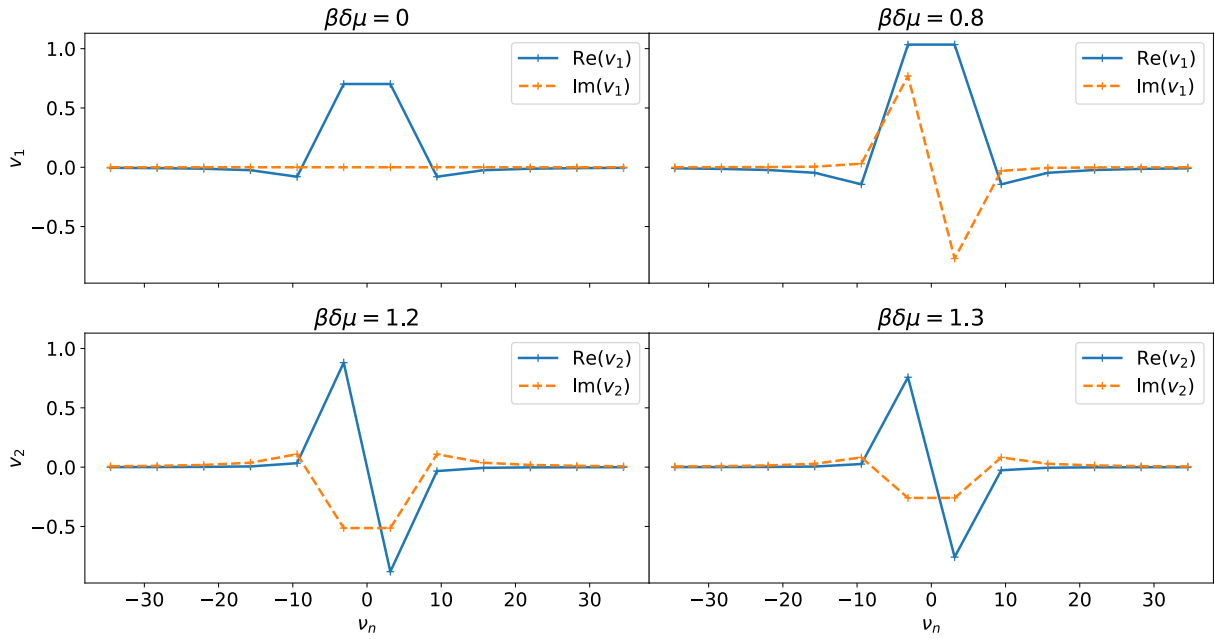
Figure 4.6: Eigenvectors along the first parabola in the spin channel for different $\beta\delta\mu$. The exceptional point is at $\beta\delta\mu = 0.975$. Vectors are normalized with $\|.\|_T$.

For the eigenvectors along the first pseudo-divergence in Fig. 4.7 we find again the usual behavior as in the repulsive case.
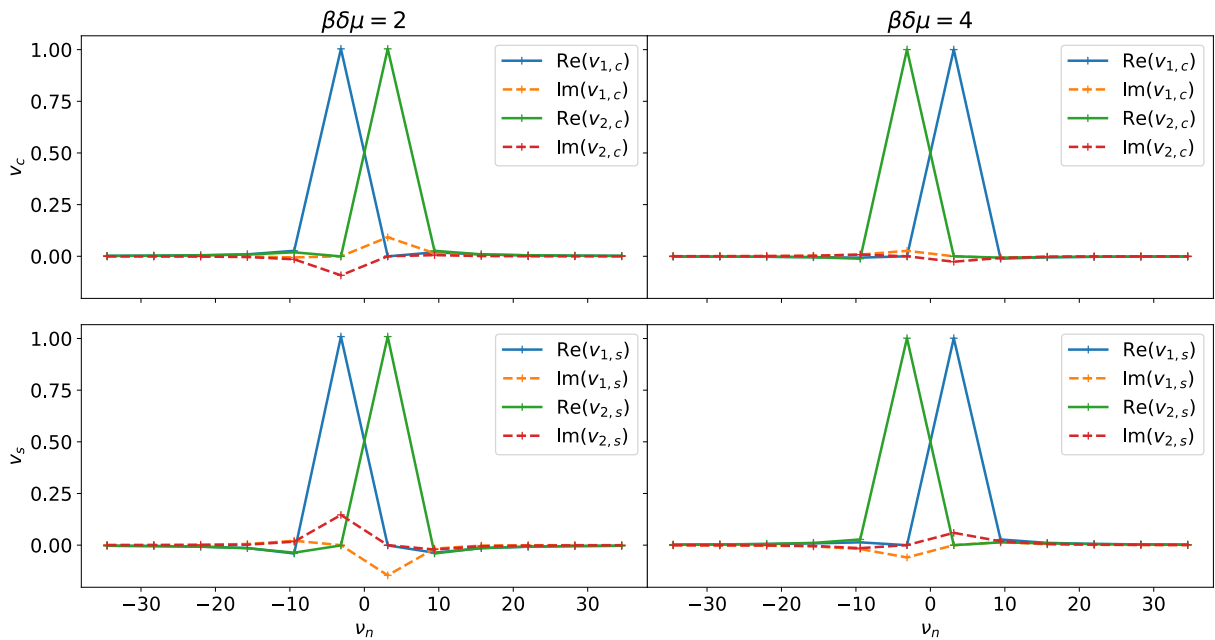
Figure 4.7: Eigenvectors along first pseudo-divergences for different $\beta\delta\mu$ ($\beta\delta\mu = 2$ is for $U < 0$ and $\beta\delta\mu = 4$ for $U > 0$). Upper row: Charge channel; Lower row: Spin channel. Vectors are normalized with $\|.\|_T$.

Looking at Figs. 4.5 to 4.7 we find, similarly as in the repulsive case, that the eigenvectors for the first parabola are approximately localized on ν_1 and $-\nu_1$, with an important exception: The

39

symmetric eigenvector in the charge channel for low βU. This specific vector gets more and more delocalized when going to lower βU, as it can be seen more clearly in Fig. A.5. The drastic delocalization for lower βU only happens for this vector, as it can be seen in Fig. A.7, and corresponds to a slow decaying frequency structure of the generalized susceptibility (Fig. A.6). Further, this behavior gives rise to the Curie behavior of the physical susceptibility as it is discussed in appendix A.3.

Finally, we want to highlight one additional feature of the reduced parameter space, introduced before, in combination with the approximately localized eigenvectors. Since the eigenvectors that correspond to the Nth symmetric or antisymmetric divergence are approximately localized at ν_N and ν_N a $2N \times 2N$-matrix is sufficient for a qualitative estimate of the position of the first N symmetric and antisymmetric divergence lines in the parameter space at arbitrary temperature[9].

4.3 Vertex divergences in the T=0 limit

The representation of the data in the reduced phase space $\{\beta\mu, \beta U\}$ can be exploited to learn something about the $T = 0$ limit of the vertex divergences. To this aim, we start by looking at the asymptotic behavior of the vertex (pseudo-)divergence lines for $\beta U \to \pm\infty$, from which we are able to infer the behavior for $\beta \to \infty$ and finite U. Our calculations show that the following asymptotic relation describes the position of the vertex (pseudo-)divergence lines in the $\beta U \to \pm\infty$ limit:

$$\beta U_r(\beta\mu_r) = k_r \beta\mu_r + d_r, \tag{4.18}$$

where r is the channel of the (pseudo-)divergence and βU_r and $\beta\mu_r$ are the values of βU and $\beta\mu$ where the (pseudo-)divergence is located. The (pseudo-)divergences present in the asymptotic regime in the repulsive sector are **(i)** the charge channel pseudo-divergences that emerge from the loops, **(ii)** the charge and spin pseudo-divergences, that emerge from the parabolas at $U < 0$ and then go through the $U = 0$ axis, and **(iii)** the pairing divergences. For a distinction between the two charge pseudo-divergences we call the pseudo-divergences that originates from the loops "repulsive" charge pseudo-divergences and the ones that stem from the parabolas in the $U < 0$ sector "attractive" charge pseudo-divergences.

In the asymptotic region of the attractive sector charge and spin divergences exist.

The fitted values of Eq. (4.18) can be seen in Tab. 4.1 for $\delta\mu > 0$ and the first (pseudo-)divergence in the considered channel.

---

[9]excluding the symmetric divergence of the first parabola in the charge channel for low βU

Sector	Channel	k_r	d_r
U>0	Charge "repulsive"	1	2.44
	Charge "attractive"	1	-3.83
	Spin	1	3.05
	Pairing	1	0
U<0	Charge	2	-7.18
	Spin	2	-2.63

Table 4.1: Fitted values for Eq. (4.18) for the different sectors and channels.

Note that all k in the repulsive sector are 1 and all k in the attractive sector are 2. Evidently, $k = 1$ corresponds to vertex divergence lines parallel to $\mu = U$ and $k = 2$ corresponds to lines parallel to the ph-symmetric line $\mu = U/2$. It is important to recall that, these two lines mark significant boarders in the phase space of the $T \to 0$ limit: They correspond to parameter points, where the ground state of the model changes leading to a discontinuity in the filling n for $T = 0$, see Eqs. (A.35), (A.39). In Fig. 4.8, the filling together with the corresponding ground states can be seen.
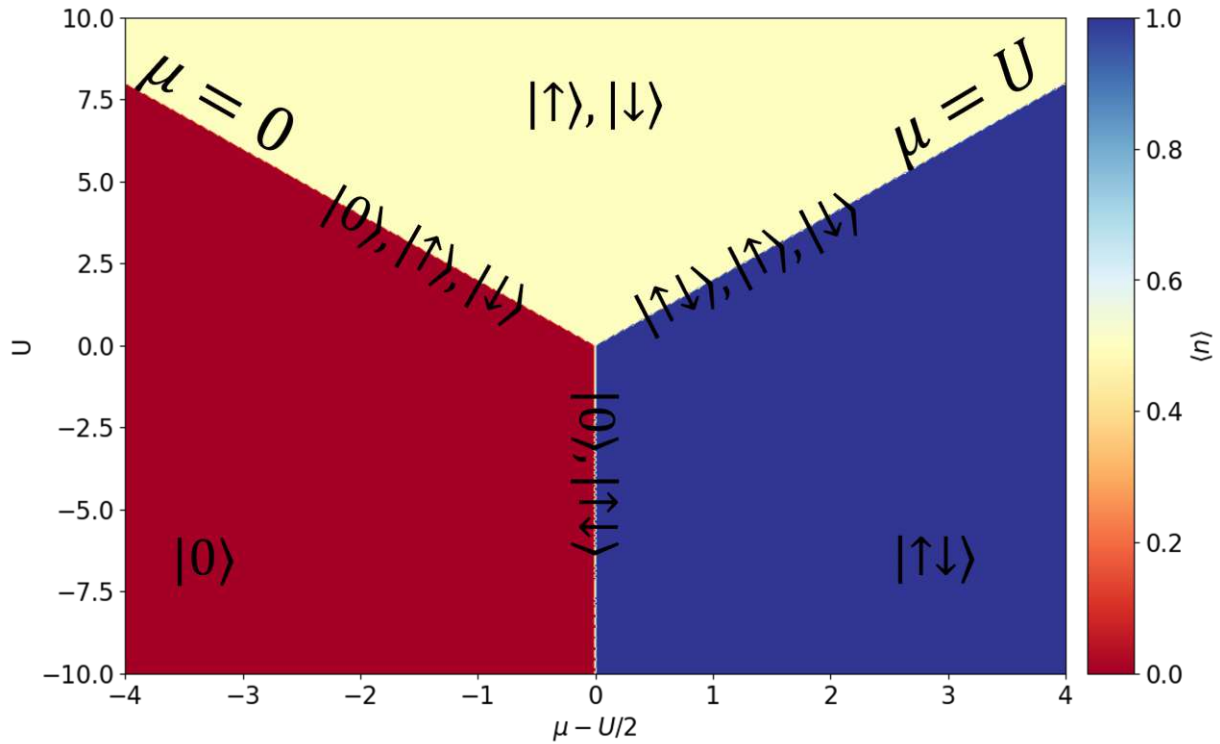
Figure 4.8: Filling $\langle n \rangle$ at $T = 0$ together with the corresponding ground state in the areas.

Since the filling n is a function of $\beta\mu$ and βU a (pseudo-)divergence is on the same value of n for every temperature. In the asymptotic repulsive regime we can set μ along the (pseudo-)divergence as $\mu = U - d_{U>0}$. This leads to

41

$$n = \frac{1 + e^{-\beta d_{U>0}}}{2 + e^{-\beta(U - d_{U>0})} + e^{-\beta d_{U>0}}} \xrightarrow{U \to \infty} \frac{1 + e^{-\beta d_{U>0}}}{2 + e^{-\beta d_{U>0}}}. \tag{4.19}$$

One will then find $d_{U>0} \to 0^{\pm}$, depending on the sign of d in Tab. 4.1, in the $T \to 0$ limit, since $\beta d_{U>0}$ must stay constant.

For the attractive sector we can set $\mu = U/2 - d_{U<0}/2$ along the divergences in the asymptotic regime. This leads to

$$n = \frac{e^{\beta U/2} + e^{-\beta d_{U<0}}}{2e^{\beta U/2} + e^{\beta d_{U<0}/2} + e^{-\beta d_{U<0}}} \xrightarrow{U \to -\infty} \frac{1}{1 + e^{3\beta d_{U<0}/2}}. \tag{4.20}$$

Therefore, also $d_{U<0} \to 0^-$ must hold for $T \to 0$.

Since we always considered the first (pseudo-)divergences in the corresponding channel we can draw the conclusion that there are *no* spin or attractive charge pseudo-divergences *inside* the V-shaped region bounded by $\mu = 0$ and $\mu = U$ (with the empirical fulfilled assumption that the (pseudo-)divergences of the same channel do not cross). Also, there are *no* pairing divergences or repulsive charge divergences *outside* this V-shaped area. Since, infinitely many loop structures for $U > 0$ and parabolas for $U < 0$ exist, we can infer that for $T = 0$ we have repulsive pseudo-divergences and pairing divergences at every (U, μ)-point inside the V-shaped area, except for ph-symmetry ($\mu = U/2$) where one has degenerate divergences namely a symmetric and an antisymmetric charge divergence and a symmetric pairing divergence for every $U > 0$ and $\mu = U/2$. Further, we have an antisymmetric charge and a symmetric spin divergence at every $U < 0$ and $\mu = U/2$. Finally, outside the V-shaped area we have pseudo-divergences in the attractive charge channel and the spin channel everywhere. All these results can be made by only considering the properties of the reduced phase $\{\beta\mu, \beta u\}$ space together with the asymptotic behavior in this reduced phase space. This shows again how useful it can be to work within this phase space.

The distribution of (pseudo-)divergence lines is schematically drawn in Fig. 4.9.
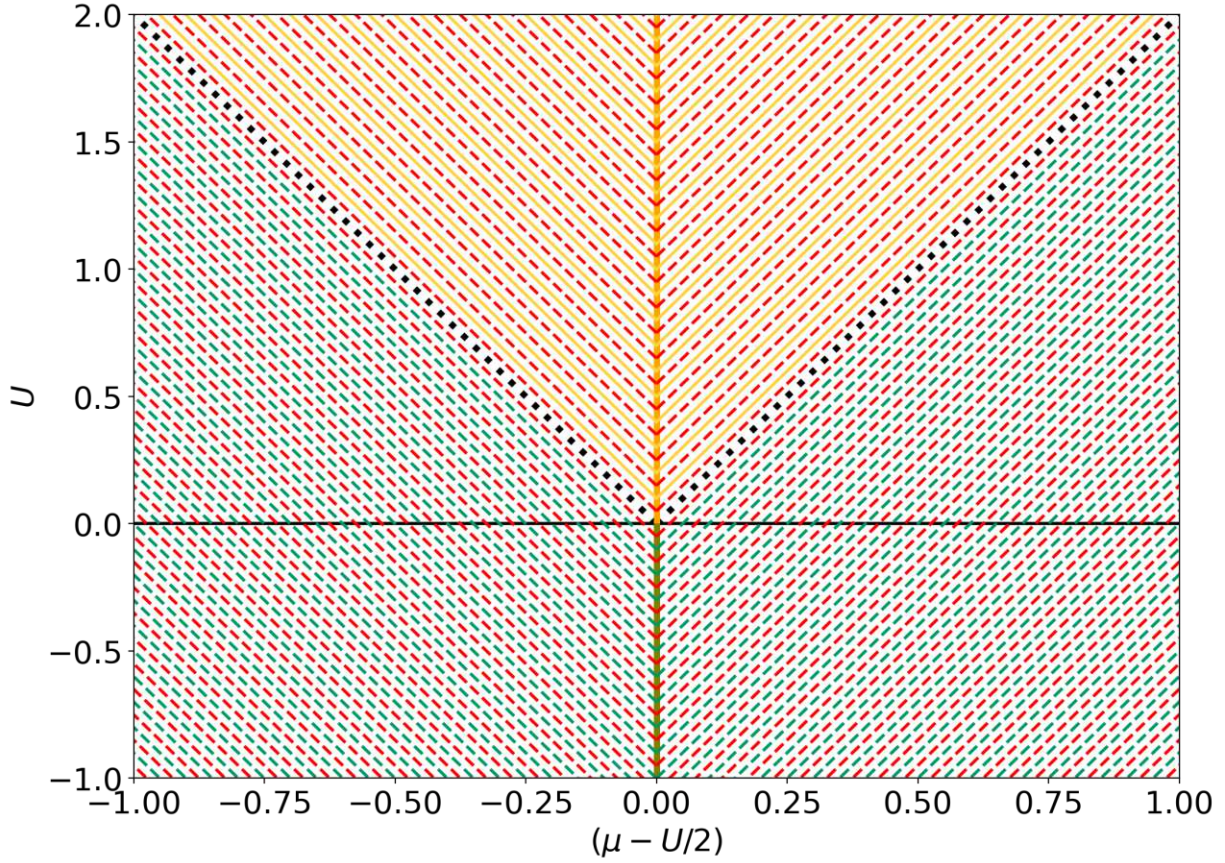
Figure 4.9: Schematic plot of the (pseudo-)divergence lines for $T = 0$. The area hatched with alternating dashed red and solid yellow lines indicates the parameter region, where pseudo-divergences in charge channel and divergences in pairing channel are found everywhere. The area hatched with alternating dashed red and green lines indicates the parameter region, where pseudo-divergences in charge and spin channel are found everywhere. At ph-symmetry $\mu = U/2$ the orange line indicates symmetric and antisymmetric charge divergences and symmetric pairing divergences for every $U > 0$ and the reddish green line indicates symmetric spin and antisymmetric charge divergences for every $U < 0$. The black dotted lines mark $\mu = 0$ and $\mu = U$.

A final note on the calculation of the different k and d values in Tab. 4.1 is due. For the spin channel in the repulsive sector and the charge channel in the attractive sector the calculation is more involved, because of the slow decaying frequency structure of the generalized susceptibilities. This structure is connected with a delocalization of a specific eigenvector, which gives rise to a Curie behavior (as discussed in appendix A.3). As a consequence, one needs to consider larger matrices for the generalized susceptibilities for larger $|U|$ values. Nonetheless, a careful analysis of the numerical data lead to the conclusion that k goes towards 1 respectively 2 for the asymptotic regime. Hence, at most, the values of d may not be accurate for these two cases, which would not affect our argumentation.

With these premises, we now use Eq. (A.7) and take the limit $T \to 0$ of the analytic formula, which allows us to further investigate the $T = 0$ limit of the HA. This leads to the operator $\chi_{c/s}(\nu, \nu', \omega)$ represented in Matsubara frequency space, where the former discrete Matsubara

frequencies become now continuous variables. The detailed procedure to obtain the operator presentation in Matsubara frequency space is described in appendix A.4. We start by analyzing the vertex divergences at $T = 0$ and particle-hole symmetry $\mu = U/2$, for this we can use the findings of Ref. [5] and take the $T = 0$ limit. The equation defining the antisymmetric divergences at ph-symmetry and $T = 0$ is

$$\nu^2 = A_r^2 \text{ with } A_\mathrm{c} = U\sqrt{3}/2 \text{ and } A_\mathrm{s} = iU/2. \tag{4.21}$$

The symmetric divergences are instead defined by

$$\nu^2 = B_r^2 \text{ with } B_\mathrm{c} = \left\{ \begin{array}{l} U\sqrt{3}/2 \text{ if } U > 0 \\ iU/2 \text{ if } U < 0 \end{array} \right. \text{ and } B_\mathrm{s} = \left\{ \begin{array}{l} -iU/2 \text{ if } U > 0 \\ -U\sqrt{3}/2 \text{ if } U < 0 \end{array} \right. \tag{4.22}$$

where, once again, the perfect mapping between spin and charge channel for the symmetric divergences can be noted.

For the repulsive sector we find degenerate symmetric and antisymmetric divergence for every finite $U = 2\nu/\sqrt{3}$ ($\nu > 0$) in the charge channel, because ν is real and continuous and no divergences in the spin channel. Note that the symmetric divergence in the charge channel is also a symmetric divergence in the pairing channel because we look at a ph-symmetric situation.

For the attractive sector, instead, we find antisymmetric divergences at all finite $U = -2\nu/\sqrt{3}$ ($\nu > 0$) and no symmetric divergences in the charge channel. In the spin channel symmetric divergences occur at all finite $U = -2\nu/\sqrt{3}$ ($\nu > 0$) while no antisymmetric divergences are present. Note that the degenerate charge divergences in the repulsive sector do not give rise to exceptional points, being simply degenerate. Pseudo-divergences out of ph-symmetry can then be formed with this degeneracy without the need for an exceptional point.

We now use the calculated $\chi_{\mathrm{c/s}}(\nu, \nu', \omega = 0)$ at $T = 0$ together with the developed discretization procedure (see appendix A.4) to compute the spectra of $\chi_{\mathrm{c/s}}$ at $T = 0$.

We start by looking at different μ values, inside and outside the V-shaped region, for constant positive U values. In Fig. 4.10 the spectrum of χ_c for $U = 1$ and different μ values is illustrated in the complex plane of their corresponding eigenvalues λ.
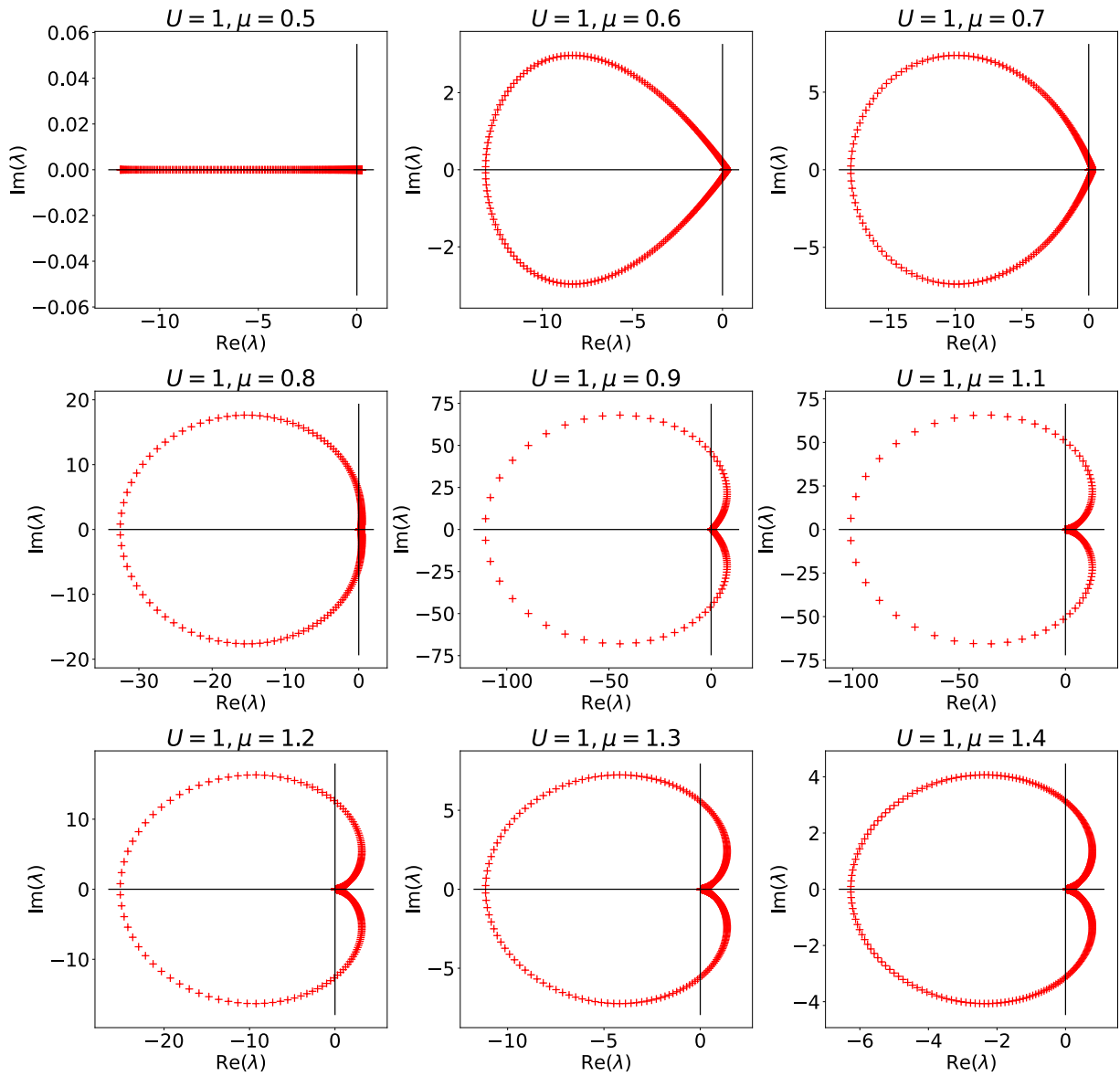
Figure 4.10: Discretized spectra of χ_c at $T = 0$ in the repulsive sector for $U = 1$ and different μ values. The spectra are presented in the complex plane of the eigenvalues λ.

Since, these spectra have been computed for the (properly) discretized version of χ_c we can argue that the spectra in Fig. 4.10 would progressively coalesce in continuous lines by taking the limit $\Delta\nu \to 0$. Therefore, it becomes clear why a divergence for every U at ph-symmetry and pseudo-divergences for every $\delta\mu \neq 0$ is found.

In Fig. 4.11 the spectra of χ_c are compared to spectra that are obtained by a χ that is calculated with the (perturbative) random phase approximation (RPA) (see appendix A.5).
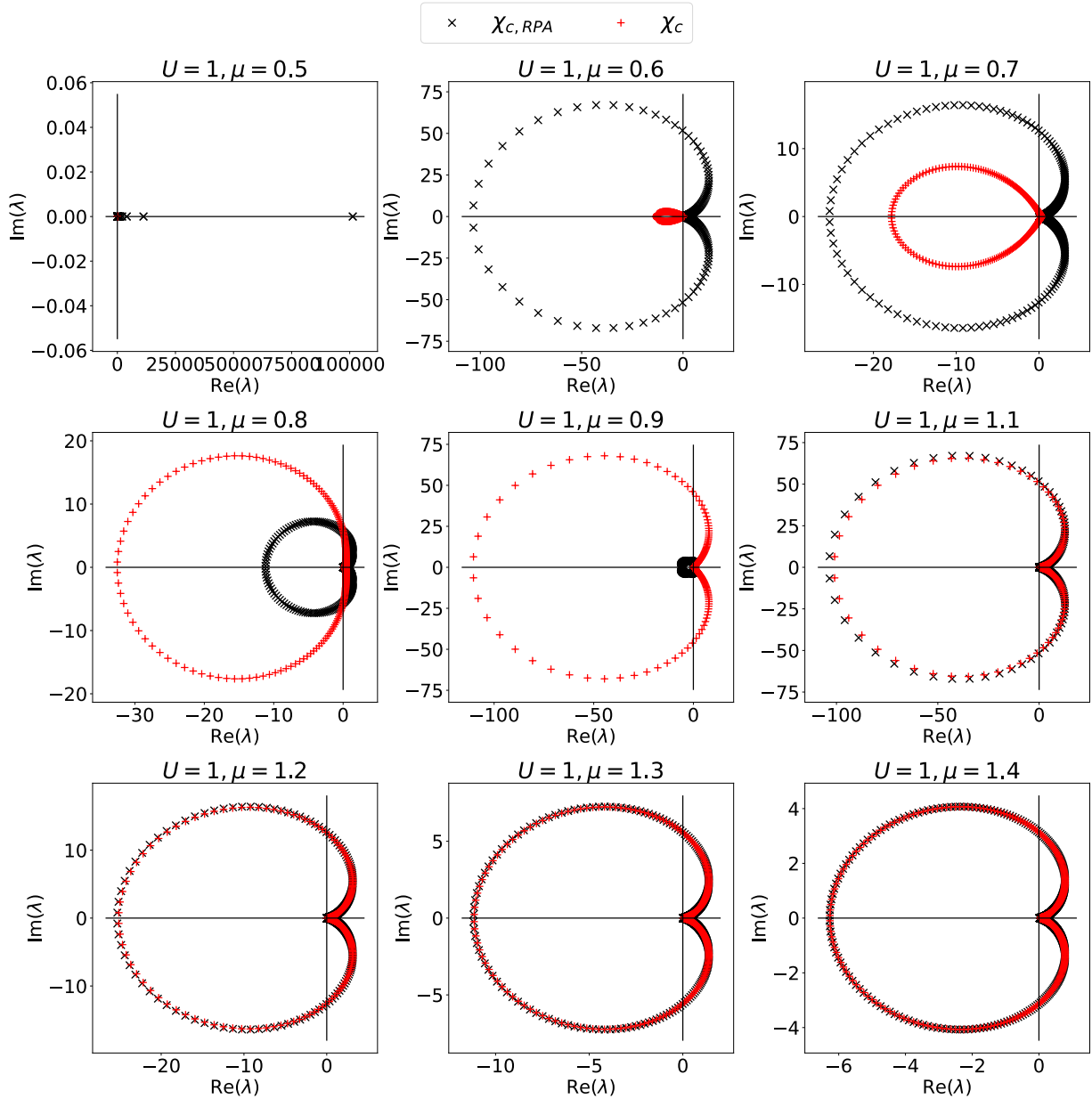
Figure 4.11: Discretized spectra of χ_c at $T = 0$ in the repulsive sector for $U = 1$ and different μ values together with the spectra of the charge susceptibility calculated with the RPA.

We see that the RPA nicely reproduce the spectra of the exact solution outside the V-shaped area $\mu > U$ but fails completely inside the V. Since RPA is a perturbative approximation, we interpret this as a signature of non-perturbative effects. Therefore, we conclude that the model has a *non-perturbative* behavior inside the V-shaped area and a *perturbative* behavior outside. Extending this argument to $T > 0$ we can infer that all divergences emerging from loop structures, which are the ones that are inside the V-shape, can have non-perturbative effects differently from the pseudo-divergences that originates from the attractive sector. This expectation is also supported by the fact that the pseudo-divergences that stem from the parabolas cross the $U = 0$ axis, which definitely link them to the perturbative regime. Hence, we can rename the pseudo-divergences as

non-perturbative when they emerge from the loop structures of divergences and *perturbative* ones for those stemming from the parabola structures found for $U < 0$ and going through the $U = 0$ axis. The interpretation suggested by such a renaming is also supported by our findings in chapter 5. Interestingly, if we now take a closer look at the spectrum, we find a qualitative difference in the structure of the spectra outside and inside the V-shaped area. This can be seen in Fig. 4.12.
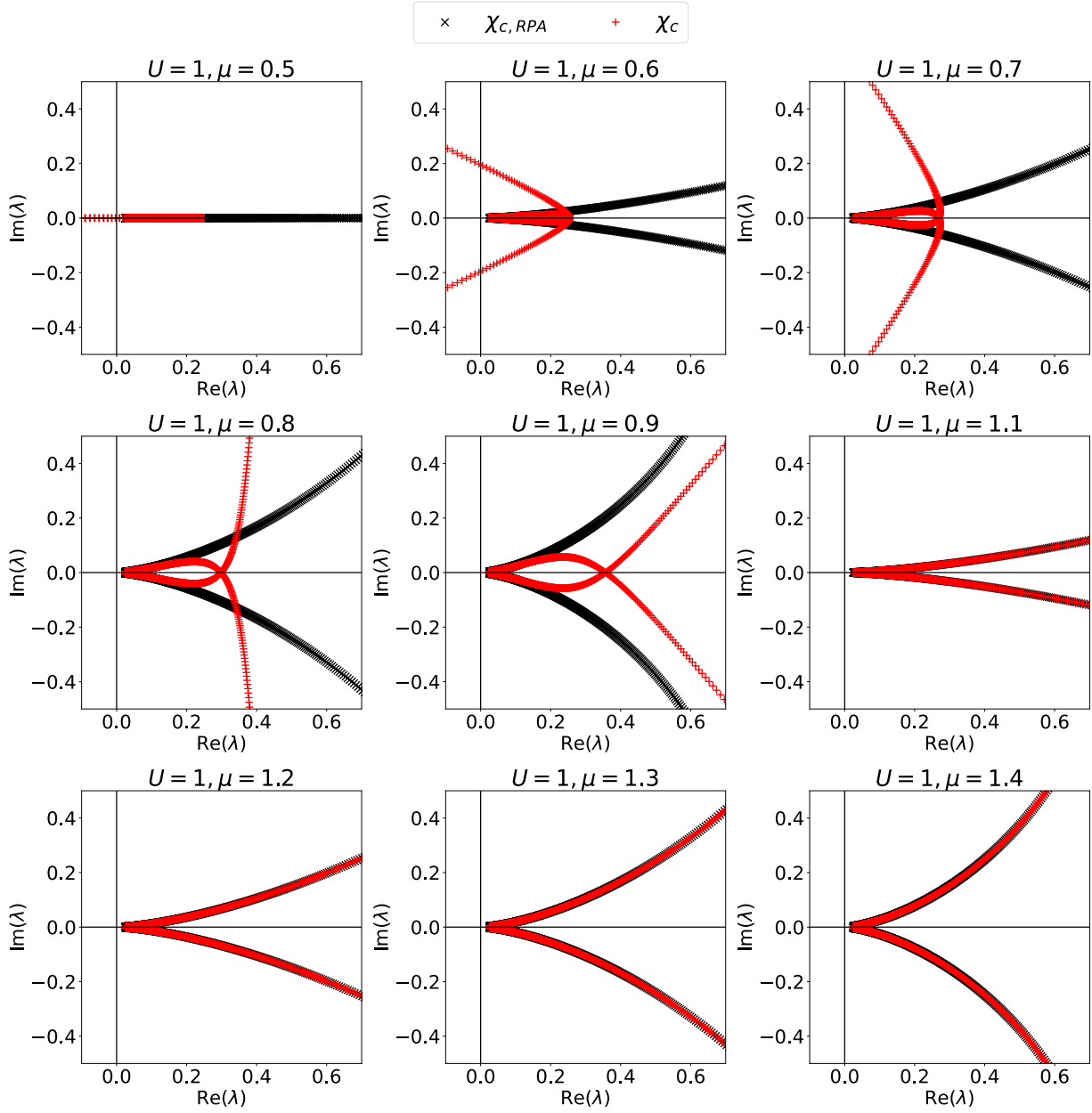
Figure 4.12: Discretized spectra of χ_c at $T = 0$ in the repulsive sector for $U = 1$ and different μ values together with the spectra of the charge susceptibility calculated with the RPA. Zoom in allows to distinguish the non-perturbative structure present for $0 < \mu < U$.

Moreover, we note that the spectra inside the V-shaped area (except for ph-symmetry at $\mu = U/2$) first cross the real axis of the complex plane and only afterward form the arches that give rise to the pseudo-divergences. Again, the RPA fails completely at reproducing this structure. Therefore,

we draw the conclusion that this structure is a distinguished signature of the non-perturbative properties of the corresponding pseudo-divergences. Further, we see that the slope at the point where the spectrum crosses the real axis gets flatter and the point where the spectrum crosses the real axis goes to ∞ as $\mu \to U^-$. This should happen since the physical charge susceptibility must diverge at $\mu = U$ (and $\mu = 0$), because there the degenerate ground state is $|\uparrow\downarrow\rangle, |\uparrow\rangle, |\downarrow\rangle$ (resp. $|0\rangle, |\uparrow\rangle, |\downarrow\rangle$) and the filling n is discontinuous.

Let us turn now to the analysis of the spin channel for the same values of μ and U. The spectra are plotted in Fig. 4.13.
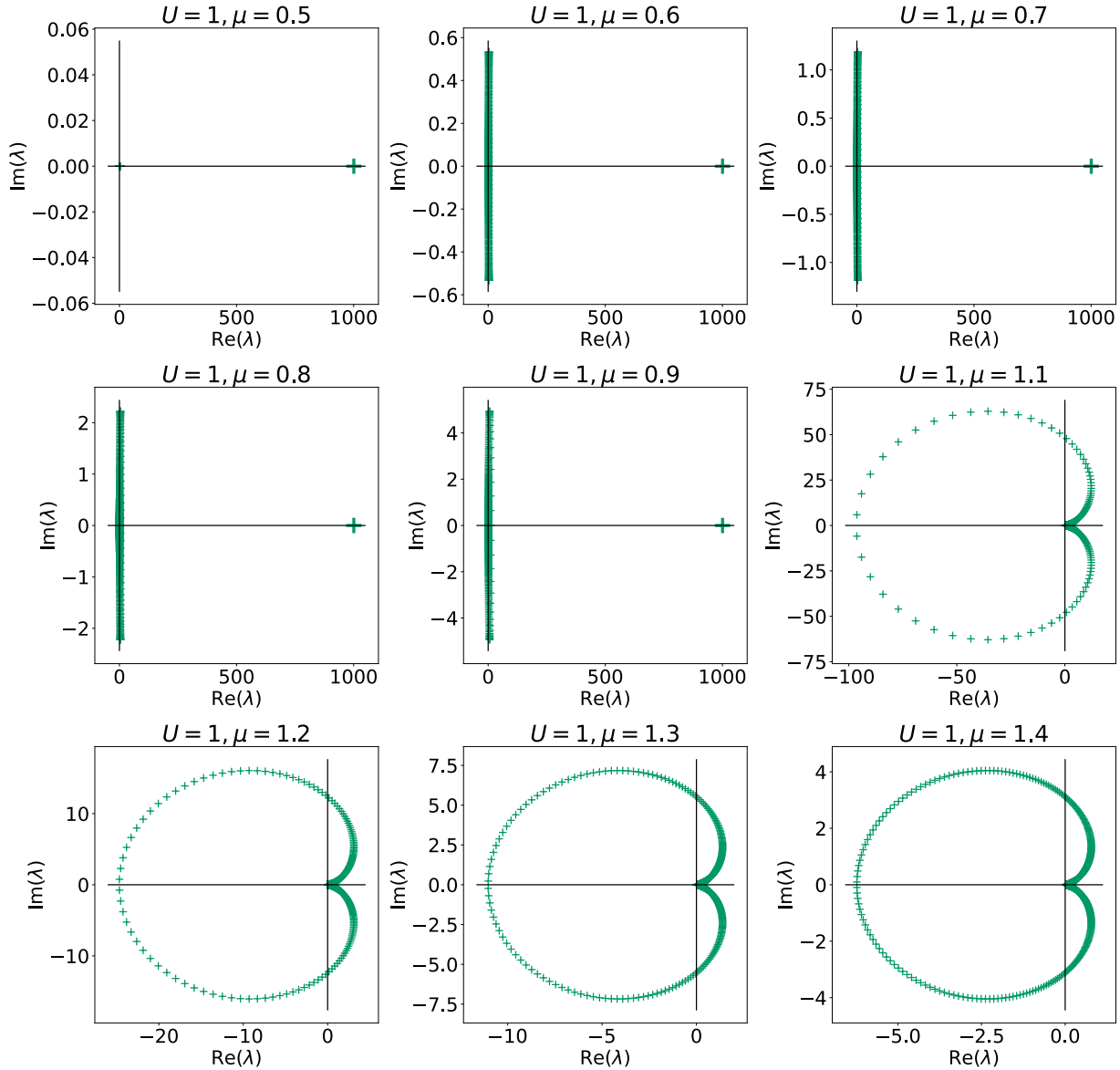
Figure 4.13: Discretized spectra of χ_s at $T = 0$ in the repulsive sector for $U = 1$ and different μ values. The spectra are presented in the complex plane of the eigenvalues λ.

We see that, for $\mu < U$, we have an eigenvalue that is disconnected from the rest of the spectrum. For a more precise inspection, we plot the spectra again without this one eigenvalue in Fig. 4.14.
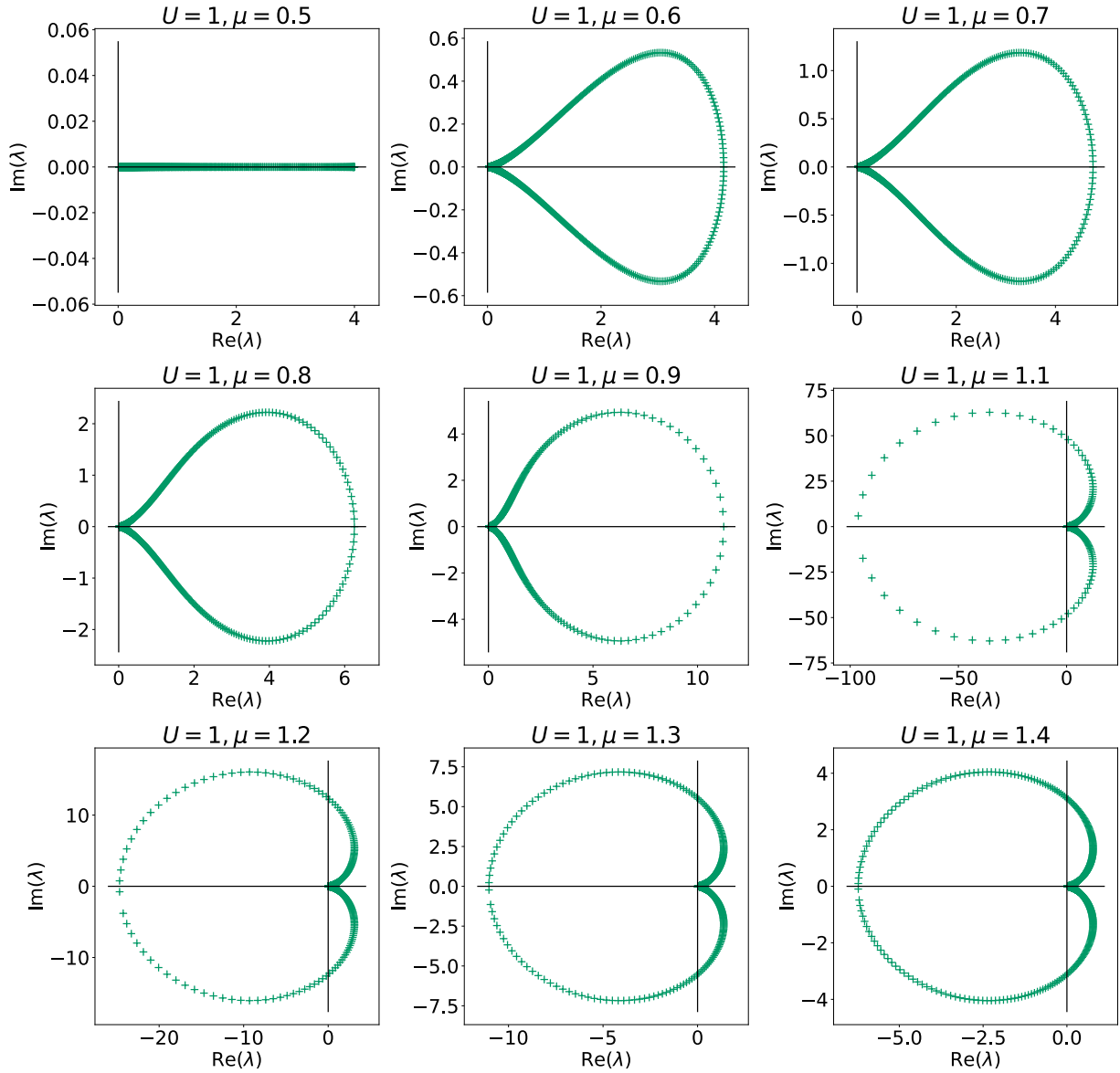
Figure 4.14: Discretized spectra of χ_{s} at $T = 0$ in the repulsive sector for $U = 1$ and different μ values. The spectra are plotted without the outlier to see if there is a pseudo-divergence.

We see that we have continuous spectra also in the spin sector, except for the one isolated outlier eigenvalue for all parameter values inside the V-shaped area. Further, we notice that we do not have any (pseudo-)divergences inside the V-shaped area and pseudo-divergences outside.

We must recall at this point, that the physical susceptibility in the spin channel $\chi_{\mathrm{s,phys}}$ must diverge for $0 < \mu < U$, because of the degenerate ground state $|\uparrow\rangle, |\downarrow\rangle$. This physics is captured by the outlier eigenvalue. Indeed, this eigenvalue goes to ∞ as discretization $\Delta\nu \to 0$, while the rest of the spectrum just gets denser, as it can be seen in Fig. 4.15. Further, this eigenvalue is connected to the delocalized symmetric eigenvector, which is also discussed in section 4.2, that leads to slow decaying frequency structure in the generalized susceptibility and gives rise to a Curie behavior of the physical susceptibility (see Fig. A.5).

49
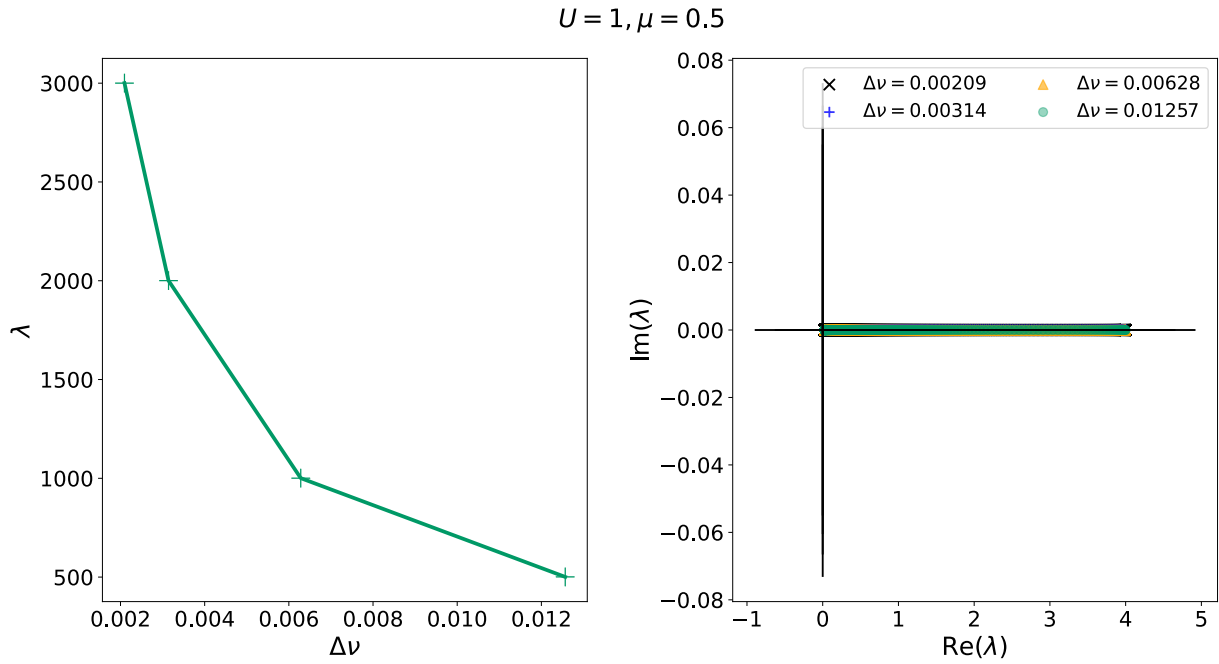
Figure 4.15: **Left:** The dependence of the outlier eigenvalue of the generalized susceptibility in the spin channel on the discretization $\Delta\nu$, one sees that the outlier eigenvalue diverges for $\Delta\nu \to 0$.
Right: The continuous part of the spectrum only gets denser with $\Delta\nu \to 0$. Both plots are for $U = 1$ and $\mu = 0.7$.

By taking a closer look at the spectra (see Fig. 4.16), we find that the structure we have previously identified as a sign of non-perturbative effects does not appear at all, consistent with the fact that the spin pseudo-divergences emerge from the parabolas at $U < 0$.
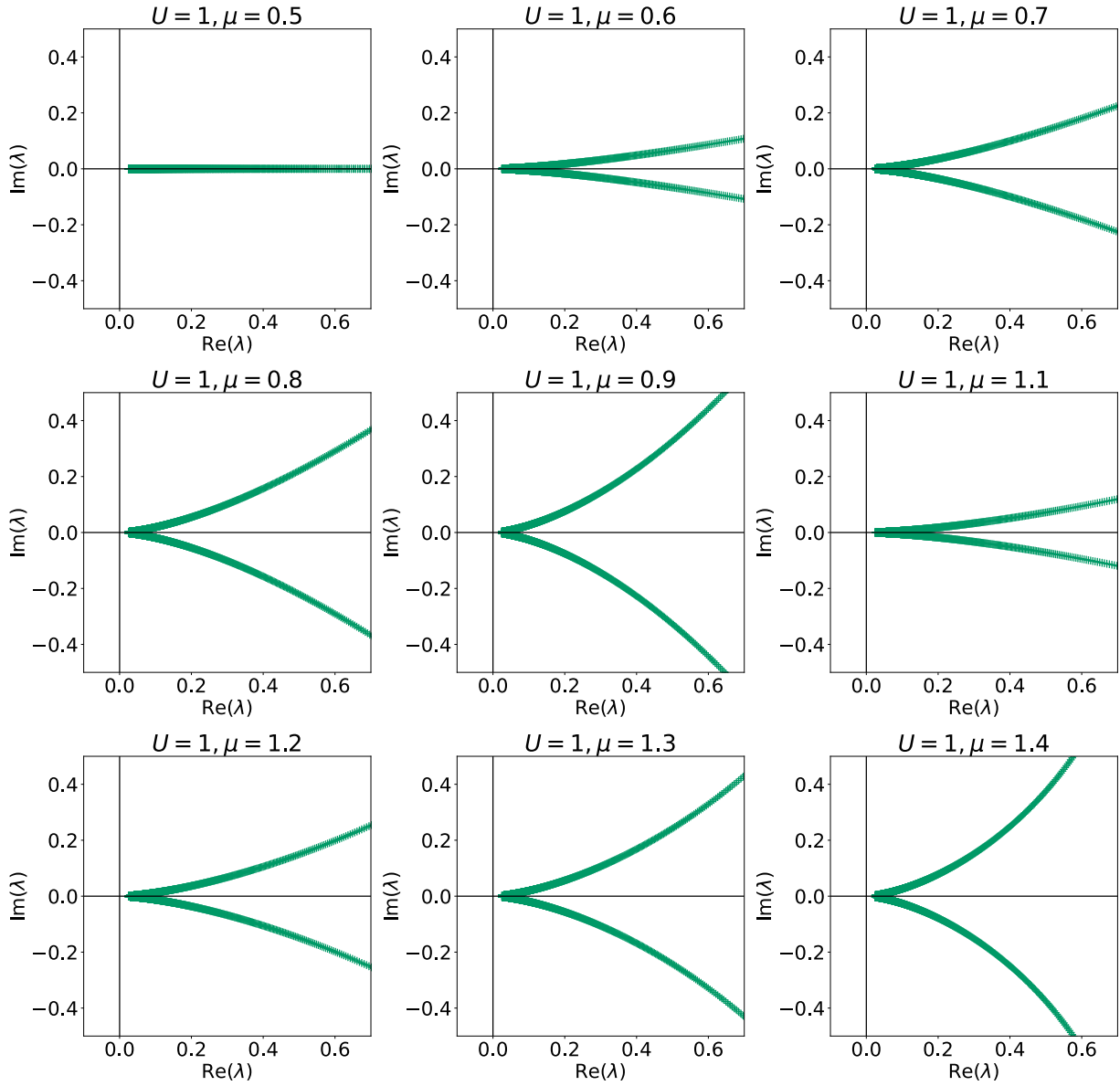
Figure 4.16: Zoomed in spectra of χ_s to see the absence of the non-perturbative structure.

We will now investigate the generalized charge and spin susceptibility at $T = 0$ in the attractive sector for $U = -1$ and different μ values. Starting with the charge channel, we plot the spectra for different μ values in Fig. 4.17.
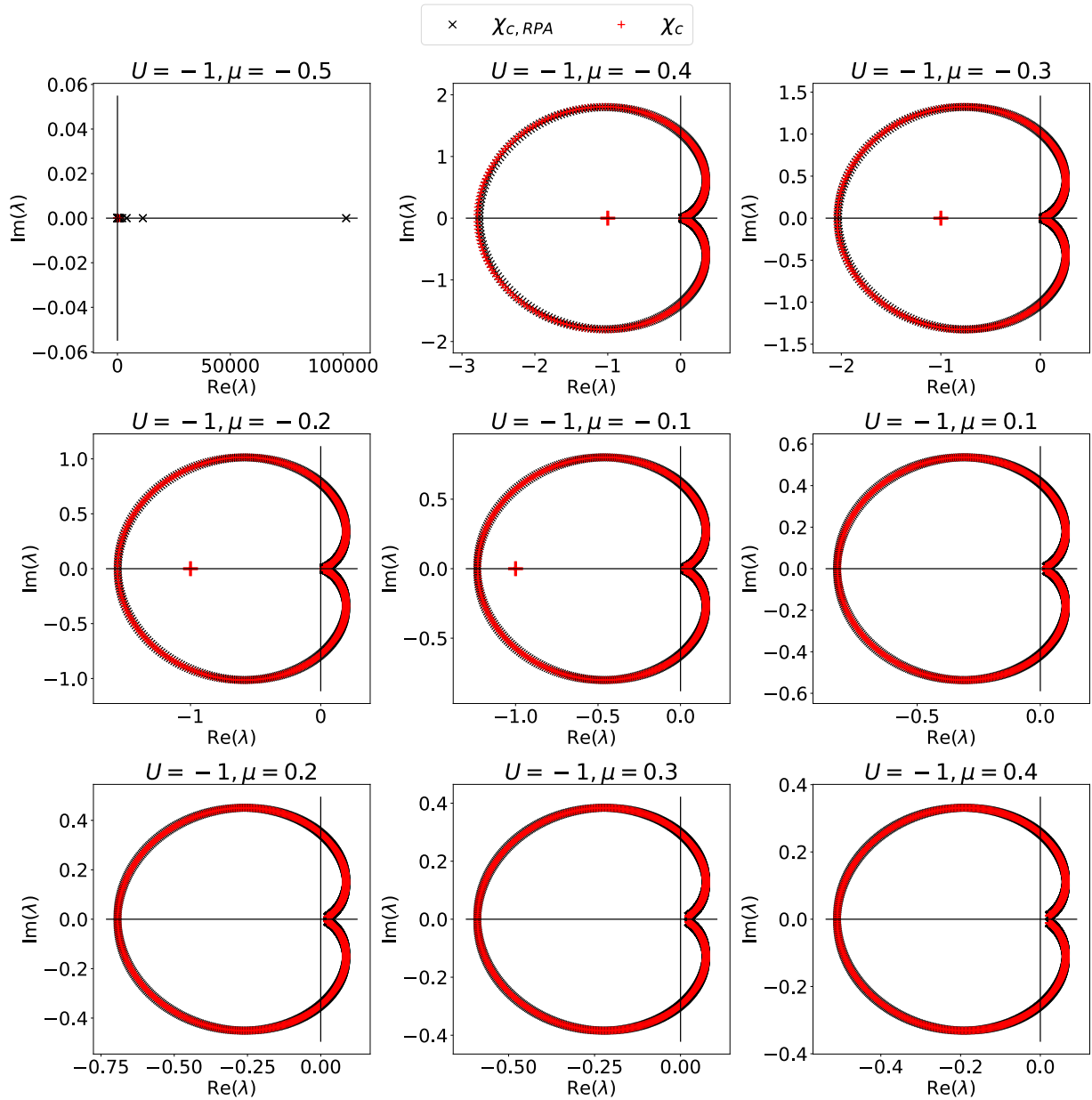
Figure 4.17: Discretized spectra of χ_c at $T = 0$ in the attractive sector for $U = -1$ and different μ values together with the spectra of the charge susceptibility calculated with the RPA.

We see that at ph-symmetry, again an outlier eigenvalue appears. This eigenvalue is again responsible for a diverging physical charge susceptibility (see Fig. 4.18) due to the degenerate ground state $|0\rangle, |\uparrow\downarrow\rangle$ at $\mu = U/2$. Further, we find a divergence for every U at half filling and pseudo-divergences everywhere out of half filling. We again have continuous spectra except for the isolated outlier eigenvalue at particle-hole symmetry and one real eigenvalue for $U/2 < \mu < 0$ at ≈ -1. This eigenvalue gets part of the continuous spectrum for $\mu > 0$. All eigenvalues that are not part of the continuous spectrum are again connected to the delocalized eigenvector associated to a slow decaying frequency structure in the generalized susceptibility. Further, this eigenvalue is connected to a Curie behavior of the physical susceptibility at ph-symmetry as discussed in

appendix A.3.

We see that the RPA nicely reproduce the spectra beyond ph-symmetry except for the one disconnected eigenvalue for $U/2 < \mu < 0$. However, this seems to be no intrinsic limitation of RPA, as it is discussed in appendix A.5.
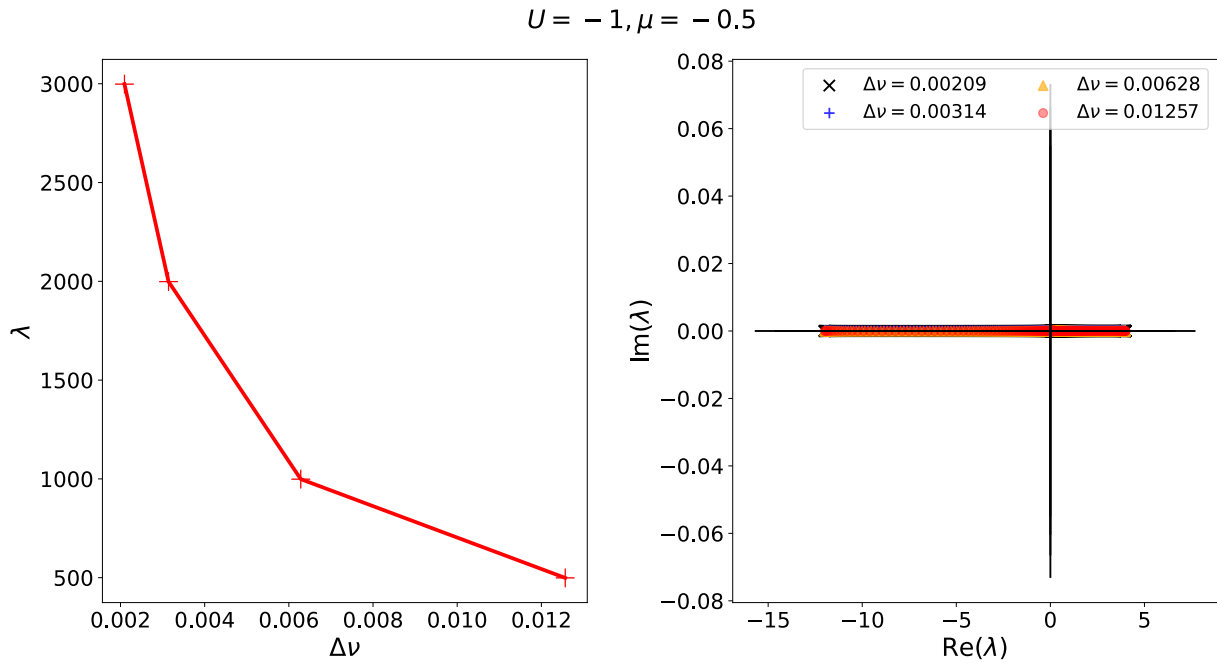
Figure 4.18: **Left:** The dependence of the outlier eigenvalue of the generalized susceptibility in the charge channel on the discretization $\Delta\nu$. One sees that the outlier eigenvalue diverges for $\Delta\nu \to 0$.
Right: The continuous part of the spectrum only gets denser with $\Delta\nu \to 0$. Both plots are for $U = -1$ and $\mu = -0.5$.

Zooming into the spectra Fig. 4.19 we find no trace of the non-perturbative structure described in Fig. 4.12, consistent with our classification of pseudo-divergences.
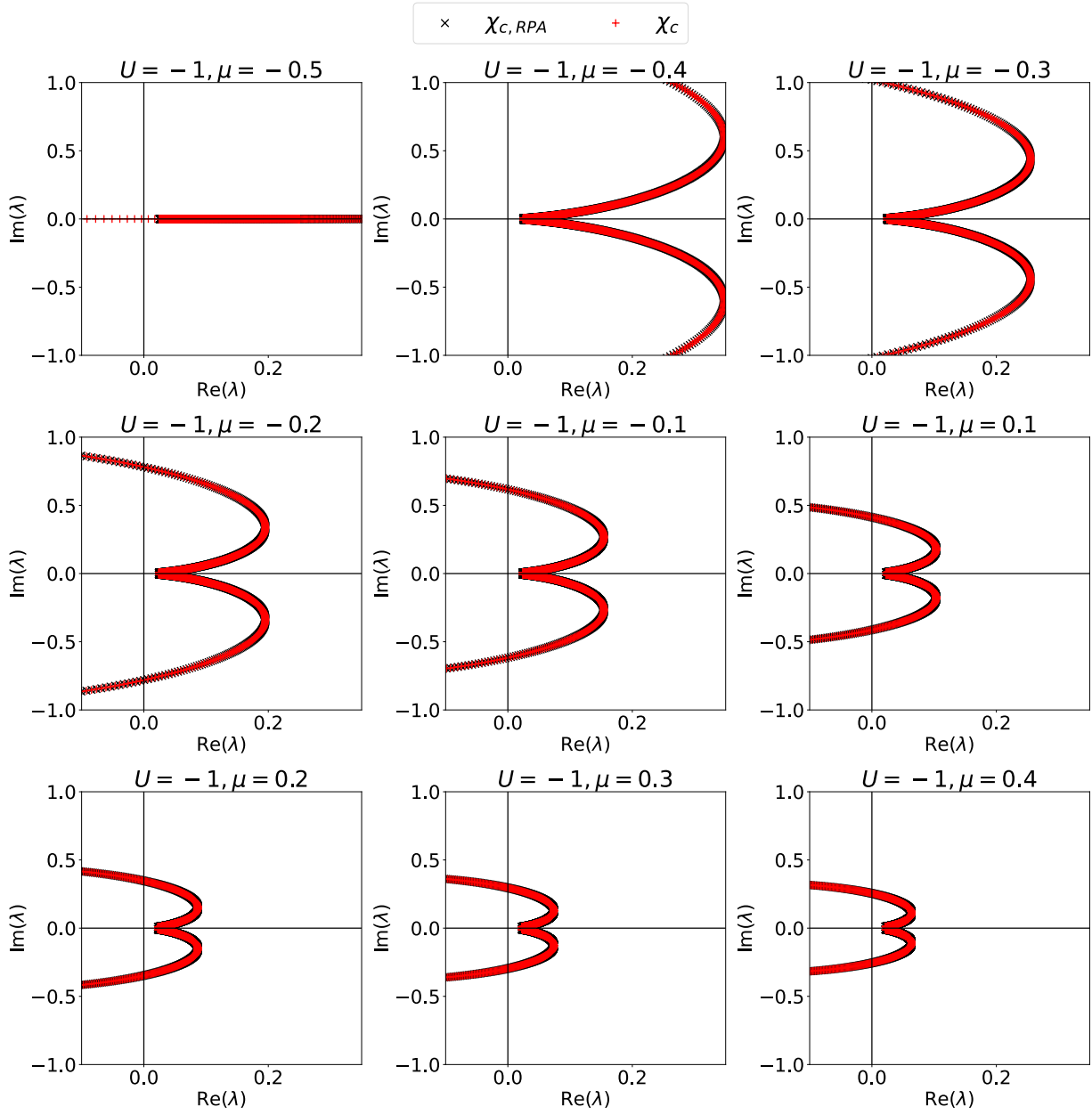
Figure 4.19: Zoomed in spectra of χ_c to see the absence of the non-perturbative structure for the pseudo-divergences together with the spectra of the charge susceptibility calculated with the RPA.

By plotting the spectra of the spin channel for the attractive sector Fig. 4.20 divergences at half filling and pseudo-divergences out of half filling are found.
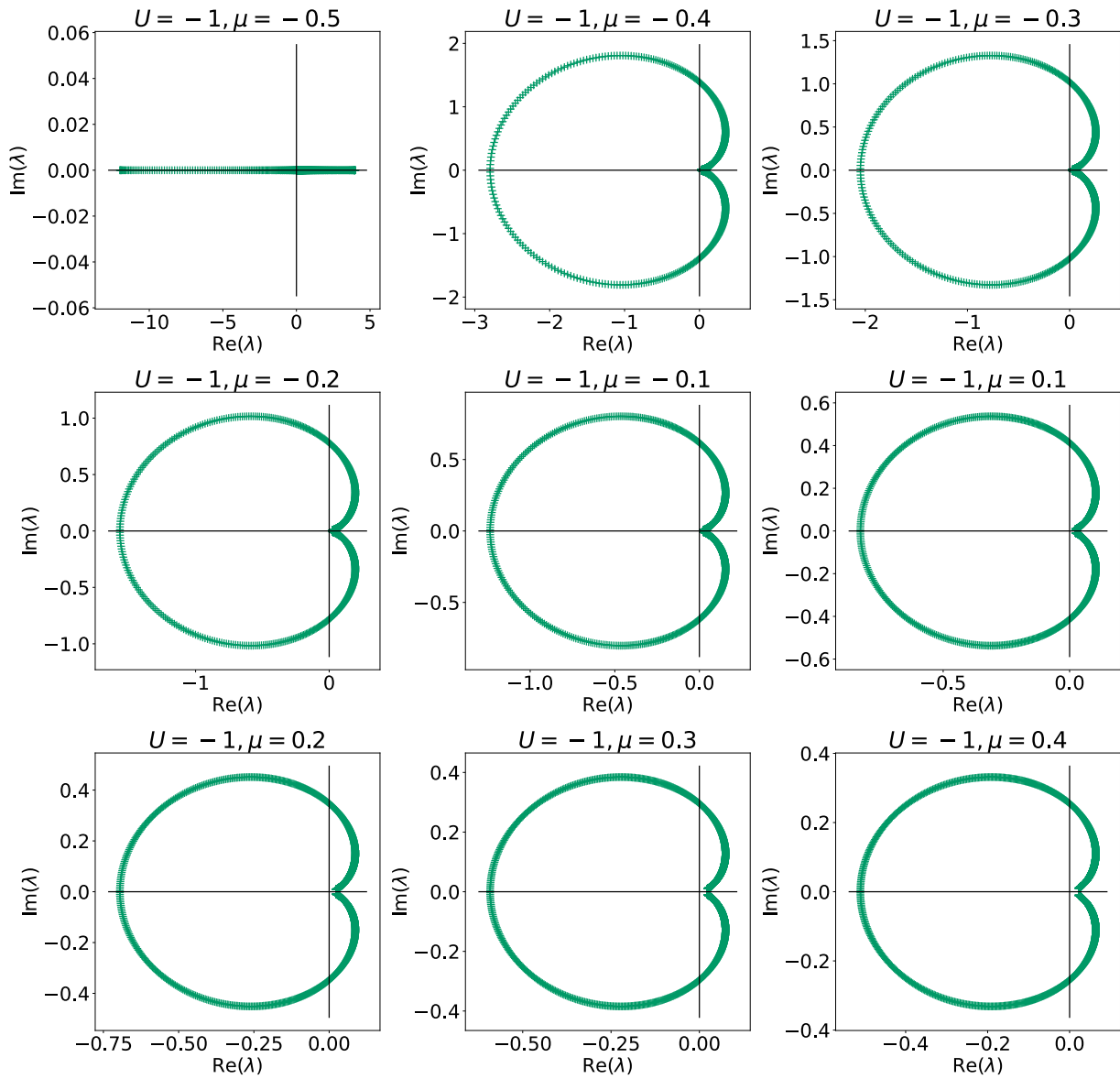
Figure 4.20: Discretized spectra of χ_s at $T = 0$ in the repulsive sector for $U = 1$ and different μ values. The spectra are presented in the complex plane of the eigenvalues λ.

Zooming into the spectra Fig. 4.21, we find again no trace of the non-perturbative structure, consistent to our classification of pseudo-divergences.
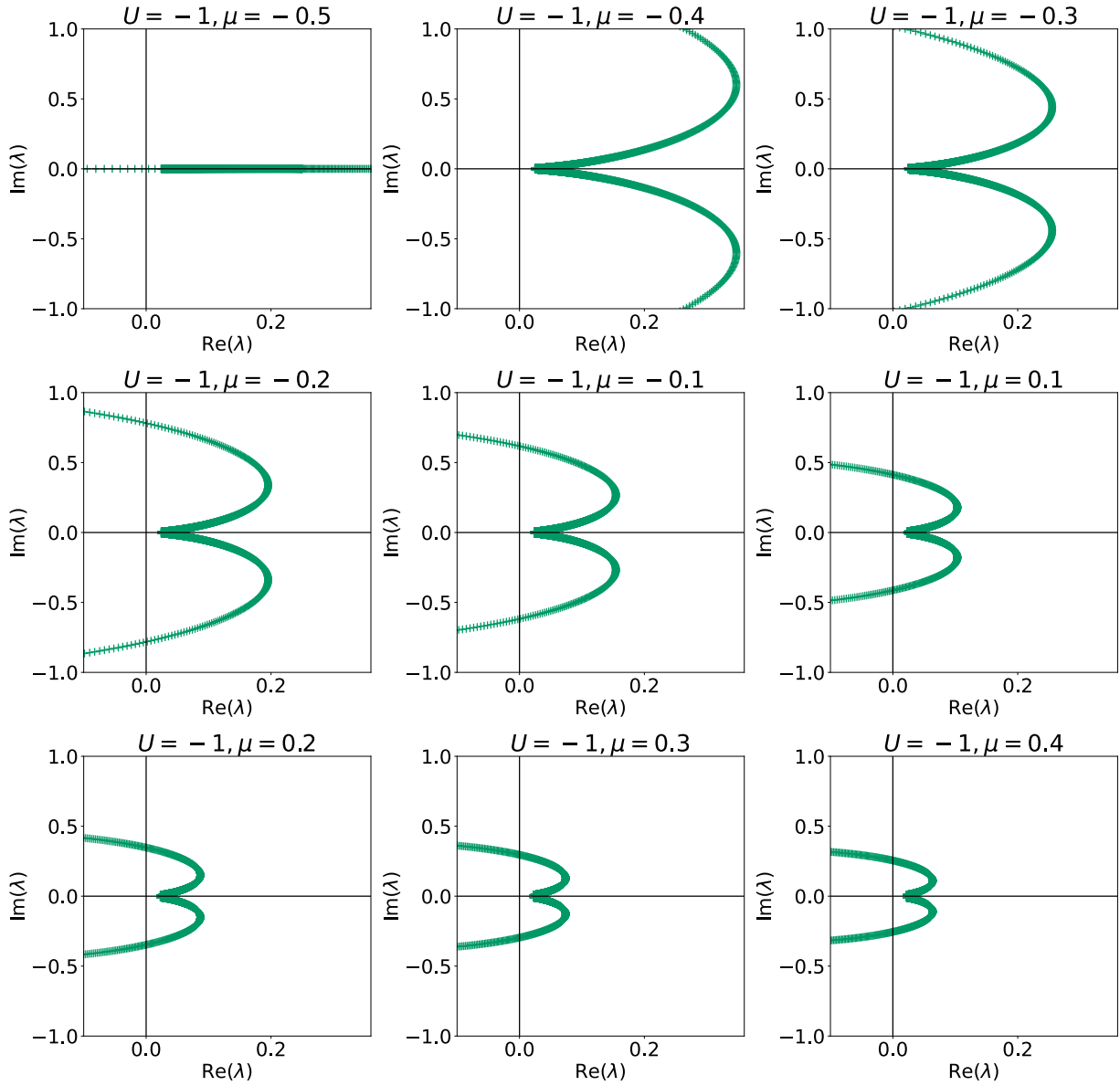
Figure 4.21: Zoomed in spectra of χ_s to see the absence of the non-perturbative structure for the pseudo-divergences.

One last comment about the formation of pseudo-divergences in the attractive sector out of half filling is due. Since we have calculated that at half filling we only find antisymmetric/symmetric divergences in the charge/spin channel, the question remains how the pseudo-divergences out of half filling can form without the crossing of a symmetric and antisymmetric divergence. We speculate that this behavior is possible due to the discontinuity in the generalized susceptibilities at $\mu = U/2$ which can be already seen by looking at n. Due to this discontinuity, the eigenvalues must not evolve continuously and pseudo-divergences can be formed without having a symmetric divergence that meets with an antisymmetric divergence.

This detailed study of the $T = 0$ spectra confirm our conclusions drawn by investigating the asymptotic regime of the reduced phase space $\{\beta\mu, \beta U\}$, highlighting the convenience of working

in this reduced phase space.

In conclusion, we find a non-perturbative region composed of the V-shaped area $0 < \mu < U$ for $U > 0$ and the line $\mu = U/2$ for $U < 0$ at $T = 0$. Remarkably, in this specific region also a violation of the Luttinger Ward theorem appears (with the obvious exception of ph-symmetric cases at $\mu = U/2$ where the LW theorem is enforced by symmetry) as consistent with [48–50].

4.4 Vertex divergences with broken SU(2)-symmetry

In this section the derived mapping from section 4.1 and the divergences out of half filling without magnetic field from section 4.2 will be used to obtain the divergences at half filling with external magnetic field. Because the pairing susceptibility, whose symmetry is not directly affected by a changing of μ, gets completely mapped to the transverse spin channel Eq. (4.16), we note that the divergences in the pairing channel get just mapped to the transverse spin channel. Further, the symmetric part of a charge eigenvector gets mapped to the spin channel respectively the symmetric part of a spin eigenvector gets mapped to the charge channel as in Eqs. (A.19), (A.20). For finite magnetic field the charge and the longitudinal spin sectors are coupled. Therefore, it is convenient to define the percentage of a divergence occurring in this enlarged space in terms of charge or spin relative contributions by using the quantities $\mathcal{S}$ and $\mathcal{A}$. To this aim, we split the eigenvector v of $\chi_{c,\delta\mu}$ or $\chi_{s,\delta\mu}$, that is normalized by $\|.\|_T$, in symmetric part $v_{\mathcal{S}}$ and antisymmetric part $v_{\mathcal{A}}$

$$v = v_{\mathcal{A}} + v_{\mathcal{S}} \quad \text{with} \quad v_{\mathcal{S}/\mathcal{A}} = \frac{1}{2}(v \pm Jv). \tag{4.23}$$

Then we define[10]

$$\mathcal{S} = \frac{\|v_{\mathcal{S}}\|_{\dagger}^2}{\|v\|_{\dagger}^2} \tag{4.24}$$

and

$$\mathcal{A} = \frac{\|v_{\mathcal{A}}\|_{\dagger}^2}{\|v\|_{\dagger}^2}. \tag{4.25}$$

It holds that $\mathcal{S} + \mathcal{A} = 1$ therefore, we can use the value of $\mathcal{S}$ to determine the percentage in

---

[10]Note that for $\mathcal{S}$ and $\mathcal{A}$ other definitions would be also possible. Other definitions could be: a) Use v with $\|v\|_T = 1$ and define $\mathcal{S}/\mathcal{A} = \|v_{\mathcal{S}/\mathcal{A}}\|_T$. This is not practical because $\mathcal{S}/\mathcal{A} \in \mathbb{C}$ and therefore they can not be used directly to define a percentage. b) Use v with $\|v\|_{\dagger} = 1$ and define $\mathcal{S}/\mathcal{A} = \|v_{\mathcal{S}/\mathcal{A}}\|_{\dagger}$. This definition is equivalent to the definition in the main text, but because vectors normalized with $\|.\|_T$ have nicely defined symmetric and antisymmetric parts, it is more handy to work with these vectors. The equivalence is due to the fact that $\tilde{v} = \frac{v'}{\|v'\|_{\dagger}}e^{i\varphi}$, where $\tilde{v}$ and v' are the same vector but different normalized ($\|\tilde{v}\|_{\dagger} = 1$, $\|v'\|_T = 1$) and φ is the phase of $\|\tilde{v}\|_T$. Finally, the factor $1/\|v\|_{\dagger}^2$ in the definition in the main text is needed, because $\|v\|_{\dagger} \neq 1$ and this would lead to $\mathcal{S} + \mathcal{A} \neq 1$ without this factor.

longitudinal spin/charge space of a mapped vector when the original vector was a vector in charge/spin channel and $\mathcal{A}$ is the percentage that stays in the original channel. This is also used for the weighted color coding in Fig. 4.22.

Now consider the vectors v_1 and v_2 of a complex conjugate pair, again normalized with $\|.\|_T$. Because of Eq. (3.10) the symmetric and antisymmetric parts of v_1 can be written as

$$v_1 = \frac{1}{2}(v_1 + v_2^*) + \frac{1}{2}(v_1 - v_2^*) \text{ with } v_{\mathcal{S}/\mathcal{A}} = \frac{1}{2}(v_1 \pm v_2^*). \tag{4.26}$$

If we now calculate $\mathcal{S}_{\mathbb{C}}$ and $\mathcal{A}_{\mathbb{C}}$ of this complex eigenvalue we get

$$\mathcal{S}_{\mathbb{C}}/\mathcal{A}_{\mathbb{C}} = \frac{\|v_{\mathcal{S}/\mathcal{A}}\|_{\dagger}^2}{\|v_1\|_{\dagger}^2} = \frac{1}{4\|v_1\|_{\dagger}^2}(v_1^{\dagger} \cdot v_1 \pm v_2^T \cdot v_1 \pm v_1^{\dagger} \cdot v_2^* + v_2^T \cdot v_2^*) = \frac{1}{2}, \tag{4.27}$$

where it was used that $v_1^T \cdot v_2 = 0$ and $\|v_2\|_{\dagger} = \|v_1\|_{\dagger}$[11].

Hence, we find that complex conjugate pairs, and therefore pseudo-divergences, have the maximal mixing ($\mathcal{S} = \mathcal{A} = 0.5$) between the coupled charge and longitudinal spin channel when we map them.

Exploiting these definitions, we then report in Fig. 4.22 our results for the divergences of the HA with magnetic field at half filling, where the weighted color coding is defined by $\mathcal{S}$ and $\mathcal{A}$.

---

[11]$v_1^T \cdot v_2 = 0$, because the vectors are orthogonal regarding the scalar product Eq. (3.7). Further, $\|v_2\|_{\dagger} = \|v_1\|_{\dagger}$ holds because of the relation $v_2 = J v_1^*$
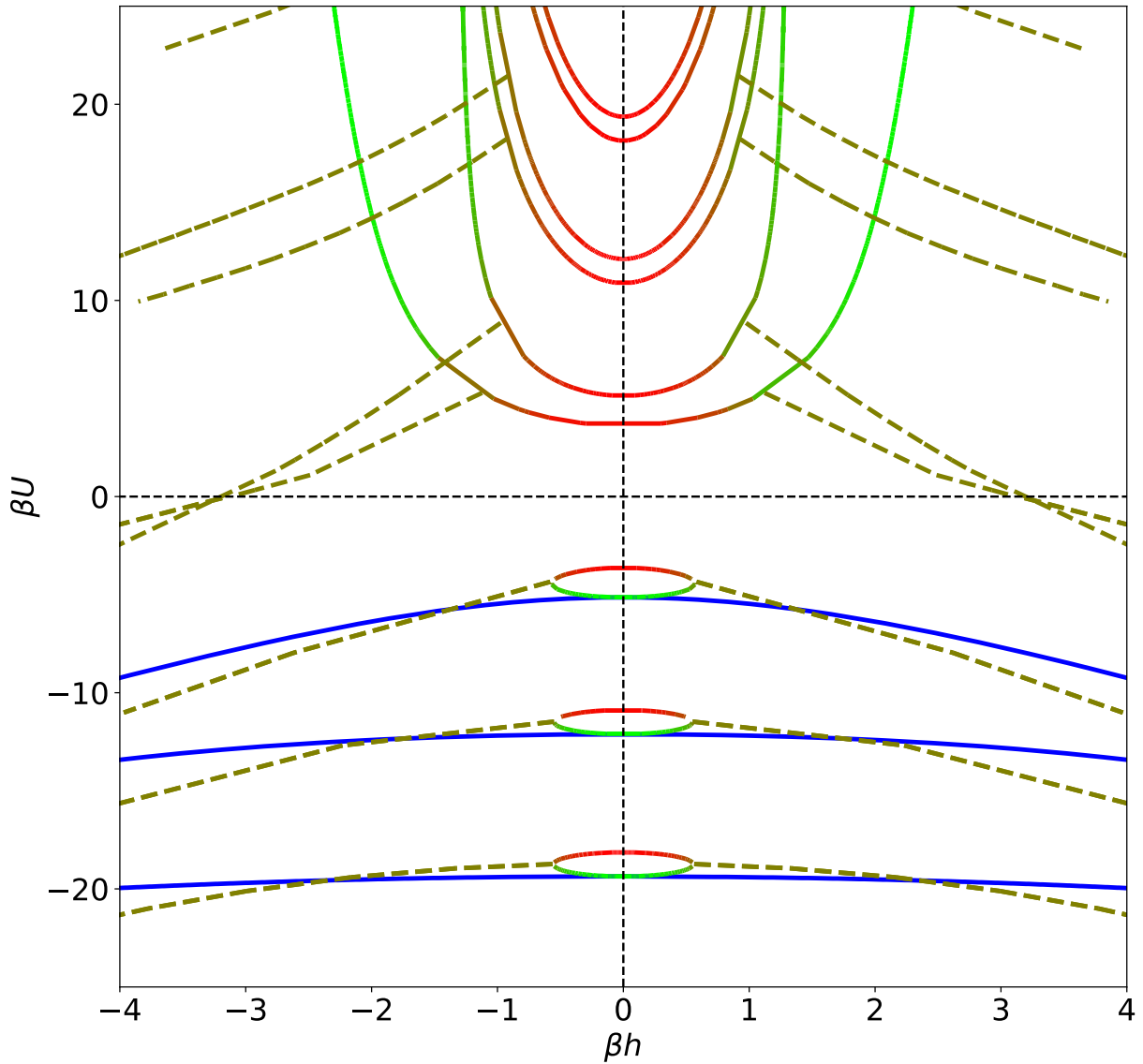
Figure 4.22: Vertex divergences and pseudo-divergences for the HA with external magnetic field h at half filling. Solid lines mark vertex divergences and dashed lines mark pseudo-divergences. The channel in which the (pseudo-)divergence appears is made clear by the color of the line: charge: red, longitudinal spin: green, transverse spin: blue. The charge and longitudinal spin channel are coupled. Therefore, the color of the coupled channel is a mix of red and green, where the portion of red/green is determined by the fraction that the eigenvector has in the charge/spin subspace, e.g. the quantities $\mathcal{S}$ and $\mathcal{A}$. The (pseudo-)divergences are plotted in the reduced parameter space $\{\beta h, \beta U\}$.

Looking at Fig. 4.22 we can immediately notice that the parabolas get mapped to the repulsive ($\beta U > 0$) sector and the loop structures get mapped to the attractive ($\beta U < 0$) sector. Looking first along the h-axis, we find that for $\beta U > 0$ we only have divergences that are fully in the charge channel and for $\beta U < 0$ the antisymmetric divergences are fully in the charge channel and the symmetric divergences are fully in the longitudinal spin channel (as it should be, regarding the findings in [5, 11]).

Going along a parabola towards the exceptional point the percentage of the longitudinal spin channel in the divergences increases. Remarkably, the maximal mixing happens at the exceptional point. Far away from the exceptional point at high βU the divergences are almost fully in the longitudinal spin channel.

For the attractive sector we find that the antisymmetric/symmetric divergence gets a greater portion in the longitudinal spin/charge channel going toward the exceptional point.

Further, we can confirm the finding of Eq. (4.27) that the pseudo-divergences are maximally mixed.

Note that this also can be deduced from the eigenvectors plotted in section 4.2, because for symmetric/antisymmetric divergences we can simply take the real/imaginary part of the eigenvector for evaluating the percentage that gets mapped to the other channel. The vectors that do not have such nice symmetry properties are the one corresponding to complex conjugated pairs of eigenvalues which always have a maximal mixing of the channels Eq. (4.27).

To give an easier to understand illustration of the mapping, which also corresponds to the "natural" properties of the mapping, i.e. $\delta\mu \leftrightarrow h$ and $U \leftrightarrow -U$, we will show two more plots.

First, we show in Fig. 4.23 the (pseudo-)divergence lines in the attractive sector for the HA with external magnetic field at half filling together with the repulsive sector out of half filling and without magnetic field. Where the SU(2)-broken case is obtained via the derived mapping and the x-axis is βh for $U < 0$ and $\beta\delta\mu$ for $U > 0$.

Second, we show in Fig. 4.24 the (pseudo-)divergence lines in the repulsive sector for the HA with external magnetic field at half filling together with the attractive sector out of half filling and without magnetic field. Where the SU(2)-broken case is obtained via the derived mapping and the x-axis is βh for $U > 0$ and $\beta\delta\mu$ for $U < 0$.
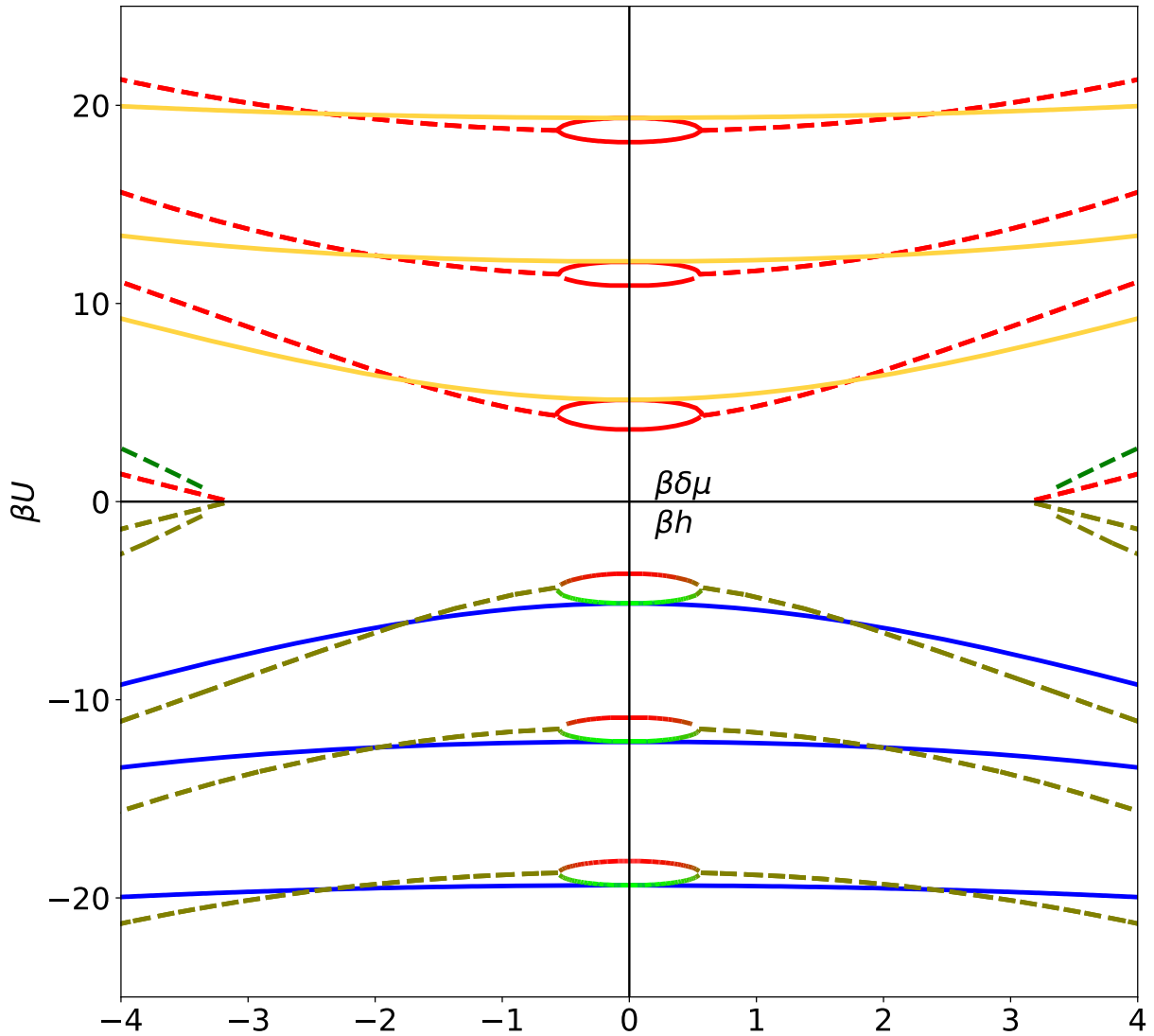
Figure 4.23: Mapping of the repulsive vertex divergences and pseudo-divergences in the HA from out of half filling without magnetic field to magnetic field h at half filling. Solid lines mark vertex divergences and dashed lines mark pseudo-divergences. The channel in which the (pseudo-)divergence appears is made clear by the color of the line: charge: red, longitudinal spin: green, transverse spin: blue, pairing: yellow, spin with SU(2)-symmetry: bluish green. The charge and longitudinal spin channel are coupled. Therefore, the color of the coupled channel is a mix of red and green, where the portion of red/green is determined by the fraction that the eigenvector has in the charge/spin subspace. The (pseudo-)divergences are plotted in the reduced 2-d parameter space $\{\beta\delta\mu, \beta U\}$ in the upper half and in the $\{\beta h, \beta U\}$ in the lower half
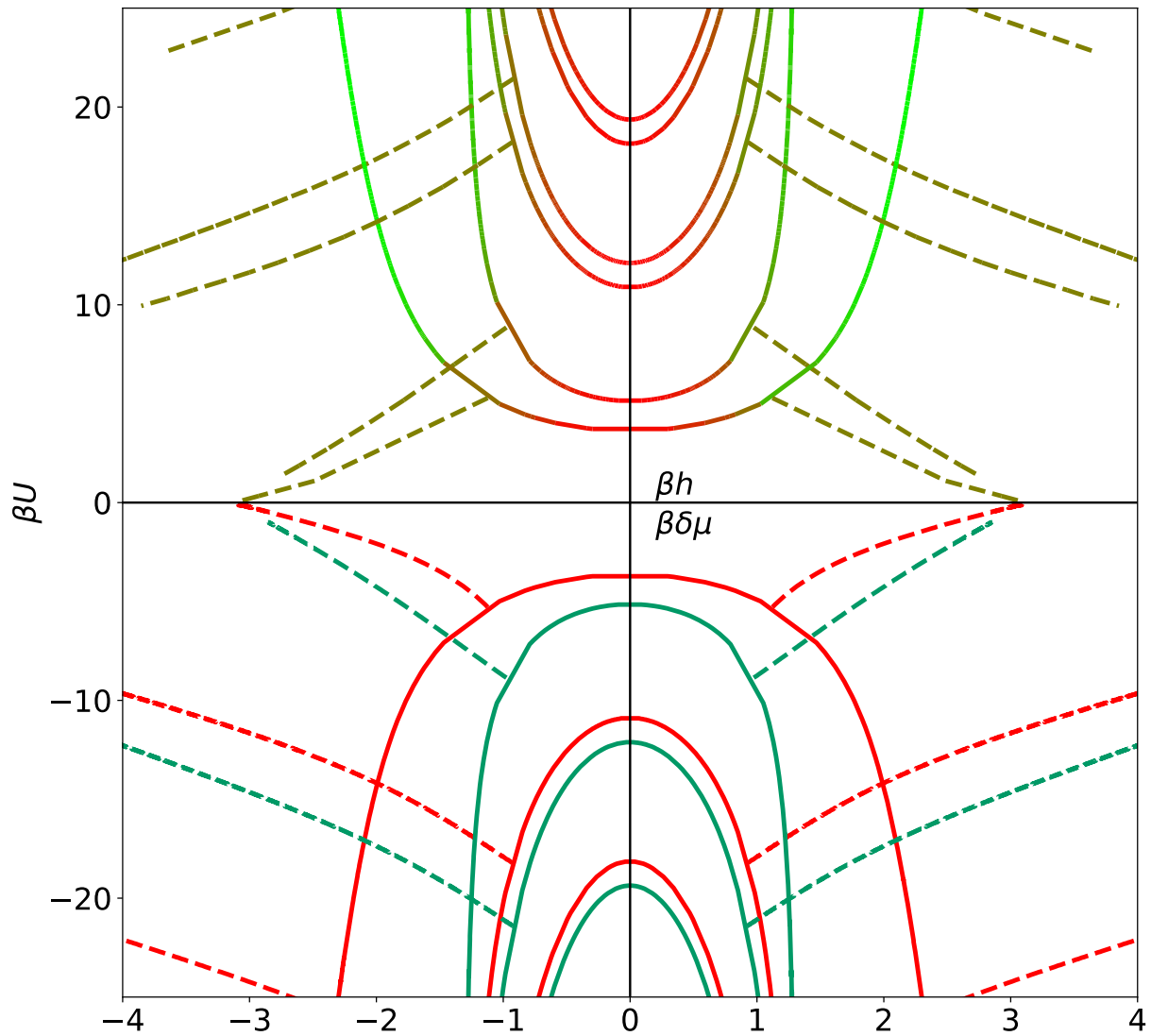
Figure 4.24: Mapping of the attractive vertex divergences and pseudo-divergences in the HA from out of half filling without magnetic field to magnetic field h at half filling. Solid lines mark vertex divergences and dashed lines mark pseudo-divergences. The channel in which the (pseudo-)divergence appears is made clear by the color of the line: charge: red, longitudinal spin: green, spin with SU(2)-symmetry: bluish green. The charge and longitudinal spin channel are coupled. Therefore, the color of the coupled channel is a mix of red and green, where the portion of red/green is determined by the fraction that the eigenvector has in the charge/spin subspace. The (pseudo-)divergences are plotted in the reduced 2-d parameter space $\{\beta h, \beta U\}$ in the upper half and in the $\{\beta \delta \mu, \beta U\}$ in the lower half

Chapter 5

Results: Branching of solutions

This chapter focuses on the second manifestation of the breakdown of perturbation theory: The misleading convergence of the bold perturbation series, which originates from the intrinsic multivaluedness of the Luttinger-Ward functional. To investigate the misleading convergence in the Hubbard Atom (HA) beyond particle-hole symmetry an iterative scheme, originally introduced in Ref. [20], that calculates G_0, given the exact G (which is analytically known in the HA), is used. This scheme mimics the convergence of the bold perturbation series, with the difference that G is fixed and not G_0 as in the bold perturbation series. The convergence of the iterative scheme is investigated in the phase space of the SU(2)-symmetric Hubbard Atom beyond particle-hole symmetry and linked to the results presented in the previous chapter.

5.1   Method

In this chapter we investigate the convergence of the bold (self-consistent) perturbation series for the Hubbard Atom beyond particle-hole symmetry.

For this we adapt scheme A in Eq. (3.18) developed in Ref. [20], that empirically (see section 3.3) mimics the convergence of the bold perturbation series. The difference to the bold perturbation series is that we fix the full Green's function G to obtain a G_0.

The adapted scheme is presented in Eq. (5.1)

$$[G_0^{-1}]^{(n+1)} = G_{\text{phys}}^{-1} + \Sigma[G_0^{(n)}], \tag{5.1}$$

where $\Sigma[G_0^{(n)}]$ is calculated with the AIM solver. To solve the AIM, a hybridization expansion continuous-time quantum Monte Carlo (QMC) with the worm sampling method of *w2dynamics* [51] is used. In practice, a hybridization function Δ (so basically a G_0) is provided as input to the QMC solver, which gives back the corresponding impurity self energy of the associated interacting AIM. Further, as both $\Delta(\nu_n)$ and $\Delta(\tau)$ are needed as an input for *w2dynamics*, but our iterative scheme only yields $G_0(\nu_n)$ (and therefore $\Delta(\nu_n)$) we use the sparse IR package [52] to perform the inverse Fourier transformation of $\Delta(\nu_n)$.

This iterative scheme is then used until we converge to a G_0 (e.g. $\left\|G_0^{(n)} - G_0^{(n-1)}\right\| < \varepsilon$, where ε is some small positive upper bound, below which we assume that the numerical convergence has been obtained.)

Note that in the context of diagrammatic resummations in self-consistent perturbation theory there are two different parameters for convergence. First, there is the convergence with respect to iterations of the self-consistent equation, which would correspond to n in Eq. (5.1). Second, one considers the convergence with respect to the order in the expansion. This corresponds to the number of orders which are considered in the skeleton diagrams of the functional $\Sigma[G]$. The latter is the convergence one usually talks about when using bold diagrammatic schemes.

For the scheme we use the situation is a bit different: We only consider the convergence with respect to iterations of the self-consistent Eq. (5.1), since the convergence with respect to the expansion, numerically obtained via the QMC solver, is always fulfilled.

It is worth to emphasize that the numerical convergence of the iterative scheme Eq. (5.1) can be made easier by adopting the following procedure.

First, we detect if our solution oscillates with respect to the iterations. If this is the case, we mix the solution of the current iteration with the solutions of previous iterations.

Second, we exploit the inside that the Hartree term of the self energy must be nU for both the unphysical and the physical solution. This is due to the fact that we fix G to the physical solution and the corresponding Hartree term is $\frac{1}{\beta} \sum_n G(i\nu_n) e^{-i\nu_n 0^-}$. However, we noticed that although the filling of the auxiliary AIM n_{AIM} should coincide with the exact filling of the HA (n_{HA}) numerical deviations can occur. As we interpret these deviations as a numerical error, we correct the self energy from the AIM Σ_{AIM} according to

$$\Sigma = \Sigma_{\text{AIM}} - (n_{\text{AIM}} - n_{\text{HA}})U, \tag{5.2}$$

which has considerably helped the convergence of our iterative procedure in the most delicate regimes.

With this background, we calculate G_0 for paths along constant $\delta\mu$ but for different U values.

In some cases the solution we obtain depends on the starting value of Δ. For the selection of the starting value of Δ we discuss different options: **(i)** We can use the converged solution of the previous point in U as an input for next U-point. This can be either done by going from low $|U|$ values to higher values ("left to right") or by going from high $|U|$ values to low values ("right to left"). Evidently, option **(i)** has the advantage that fewer iterations are needed, reducing the overall numerical effort, but with the (potential) disadvantage of a possible bias towards one solution. To prevent this, we can use **(ii)** a random Δ as a starting value at every U-point. We interpret the two methods "left to right" and "right to left" in the context of self-consistent perturbation theory as choosing different starting values for G. Normally one chooses $G_{\text{start}} = G_0$ this would correspond to the "left to right" method as we start from a physical solution, while choosing some other (unphysical) starting value would plausibly correspond to the "right to left" method.

Following the example of Ref. [20] we note that for the analysis of the misleading convergence a practical one-dimensional parameter is the double occupancy $\langle n_\uparrow n_\downarrow \rangle$ which is related to G_0 via Eq. (5.3)

$$\langle n_\uparrow n_\downarrow \rangle = \frac{1}{\beta U} \text{Tr}(\Sigma G) = \frac{1}{\beta U} \text{Tr}\left((G_0^{-1} - G^{-1})G\right). \tag{5.3}$$

5.2 Results for the misleading convergence in the Hubbard Atom

In this section we show the results for the convergence of the scheme in Eq. (5.1) to an unphysical solution in the Hubbard Atom beyond particle-hole symmetry. For this, we apply the iterative scheme along paths with constant $\delta\mu$ and different U values and investigate several such paths with different $\delta\mu$ values.

The physical values for the double occupancy of the HA calculated with the (analytical) Eq. (2.61) and the corresponding ones calculated with the iterative obtained G_0 via Eq. (5.3) can be seen in Fig. 5.1 for $\delta\mu = 0$ (half filling). Here, the start value of $\Delta(\nu_n)$ has been set randomly at each U-point to avoid bias towards one specific solution. This is realized, by using the QMC randomized noise for $\Delta(\nu_n)$ which is possible because the hybridization function of the physical solution is exactly zero, therefore the converged physical solution corresponds to a hybridization function that is only numerical noise. To prevent a bias towards one solution, the random start value for $\Delta(\nu_n)$ is chosen such that it is one magnitude greater than the numerical noise of the physical solution.
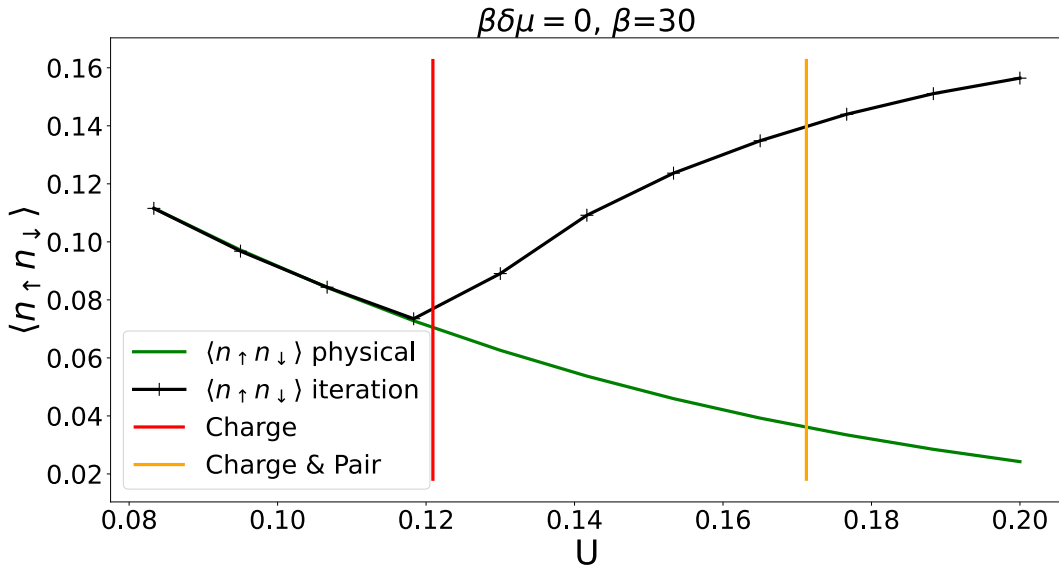
Figure 5.1: Double occupancy of the physical solution and the iteratively obtained solution for different U values and $\delta\mu = 0$ plotted over U. The red vertical line marks the U value of the first divergence in the charge channel, while the orange vertical line marks the U values of the second divergence in the charge channel, which is also a divergence in the pairing channel at half filling.

We can clearly see that the iterative scheme converges to the physical solution for U values smaller than the U value where the first divergence in the charge channel appears (marked by a vertical red line). For U values larger than the U value of the first charge divergence, we observe a convergence to an unphysical solution consistent to [12, 20].

We also compare the physical with the iterative obtained $G_0(\nu_n)$ and $\Sigma(\nu_n)$ for the largest U value of in Fig. 5.1 in Fig. 5.2.
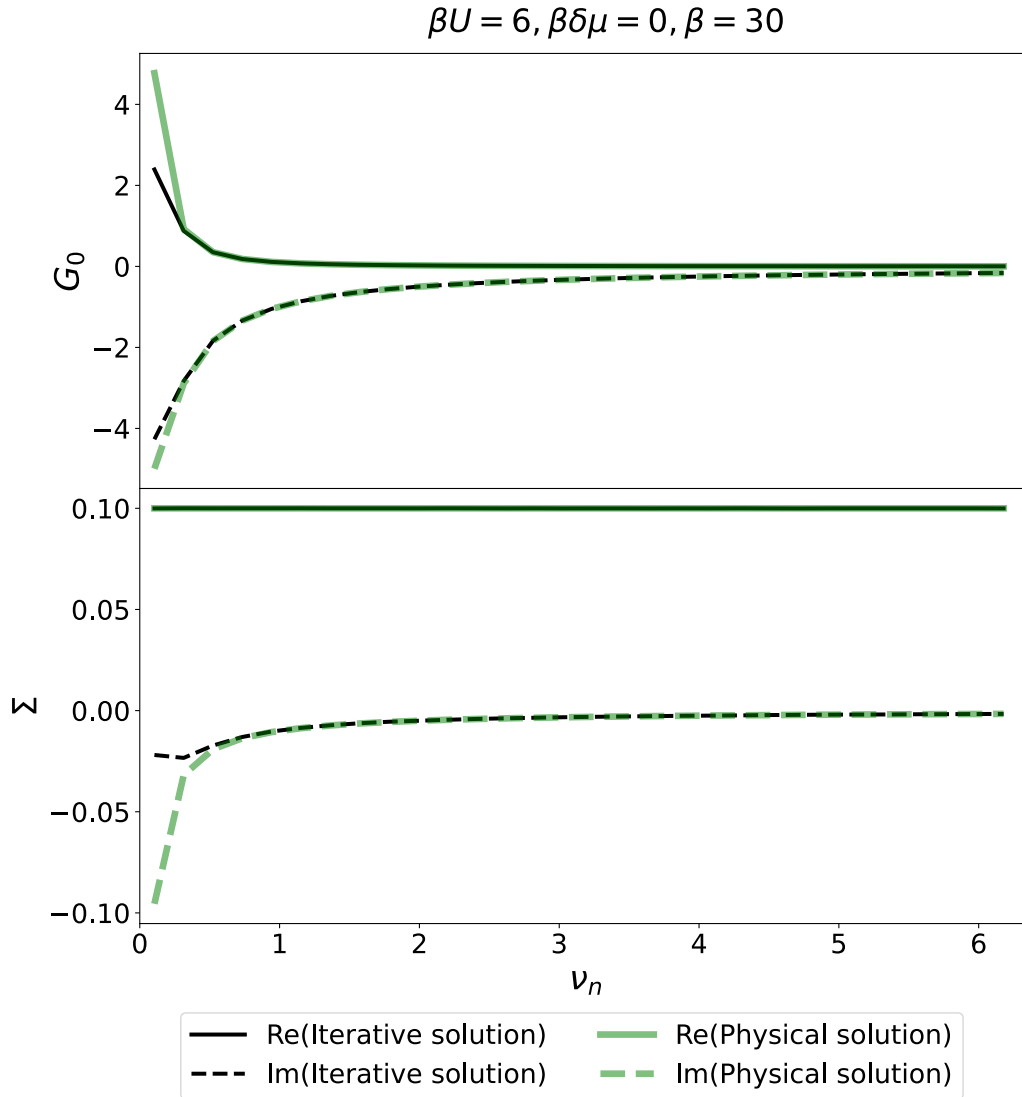
Figure 5.2: **Upper:** The physical and the iteratively obtained G_0 plotted over positive Matsubara frequencies. **Lower:** The physical and the iteratively obtained Σ plotted over positive Matsubara frequencies at $\beta U = 6$, $\delta\mu = 0$ and $\beta = 30$

We see that the main difference between the physical and the unphysical solution is at the first Matsubara frequency, therefore we will focus on comparing G_0 and Σ on the first Matsubara frequency. The corresponding data are presented in Fig. 5.3.

$$\beta\delta\mu = 0, \ \beta = 30$$
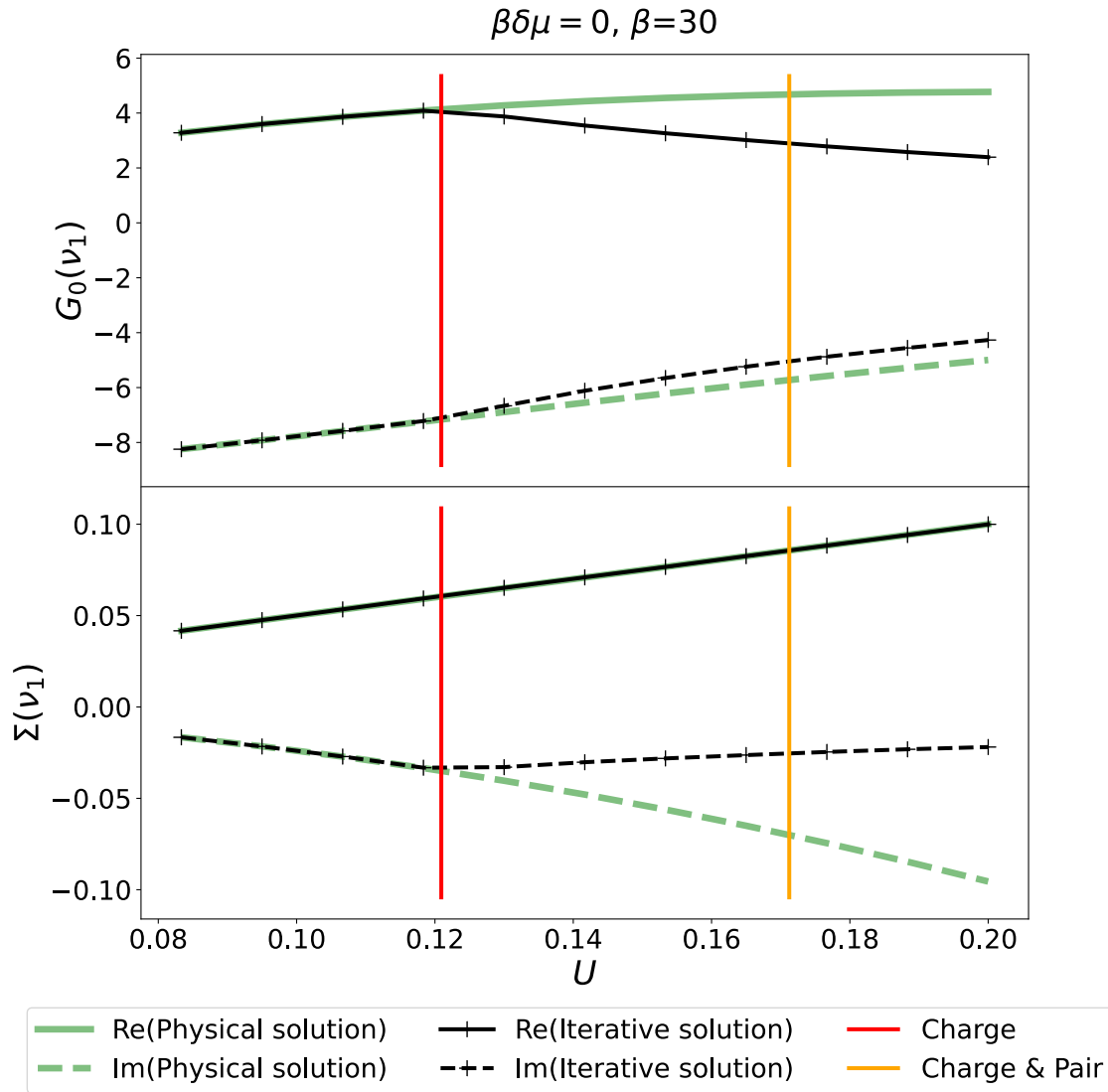
Figure 5.3: **Upper:** The physical and the iteratively obtained $G_0(\nu_1)$ of the HA plotted for different U values. **Lower:** The physical and the iteratively obtained $\Sigma(\nu_1)$ plotted for different U values at $\delta\mu = 0$ and $\beta = 30$. The red vertical line marks the U value of the first divergence in the charge channel, while the orange vertical line marks the U values of the second divergence in the charge channel, which is also a divergence in the pairing channel at half filling.

From the numerical data in Fig. 5.3 we infer that the deviation from the physical G_0 is continuous *both* in the real part and the imaginary part of the non-interaction Green's function G_0. Consequently, the deviation in Σ from the physical solution is also continuous, as G_0 and Σ are related via the Dyson equation. From this we conclude, similarly as in Ref [20], that the physical G_0 is equal to an unphysical solution at the U value of the first charge U_{div} divergence and that the two solutions approach each other continuously for $U \to U_{\mathrm{div}}$.

This observation is consistent with the proof in Ref. [12].

Moreover, we see, by looking at Figs. 5.1, 5.3, that the second charge divergence (which is also a pairing divergence because we are at half filling) does not appear to have any effect on the

67

convergence of the algorithm. This is also consistent with the proof in Ref. [12] due to the fact that only the crossing of the *physical* G_0 with some unphysical G_0 implies a divergence in the irreducible charge vertex. Since our algorithm already converged to an unphysical branch very far from $G_{0,\text{phys}}$ when crossing the second charge divergence, we do not see any particular effect.

Further, it can be seen in Fig. 5.2 that the real part of the physical and the unphysical Σ coincide. Since the only contribution to the real part of Σ at half filling is the Hartree term and the correction of Eq. (5.2) is not made for half filling, we can conclude the Hartree term of the physical and the unphysical solution is indeed the same.

Although the proof in Ref. [12] formally has been derived for half filling, it can easily be extended to vertex divergences in the charge channel out of half filling by introducing the additional parameter μ and μ_0 for the position of the crossing in μ-space additionally to U_0. Introducing this parameter does not alter the arguments of the proof, therefore we expect results that are qualitative the same as for half filling, when crossing a vertex divergence in charge channel beyond ph-symmetry. Consequently, we expect a continuous deviation from the physical G_0 and Σ after crossing the first charge divergence out of half filling ($\delta\mu \neq 0$).

This is confirmed by the numerical data in Figs. 5.4, 5.5, where the data are calculated along a "from left to right" path, e.g. using the scheme where we use the solution of the last U point as a starting point for the new U point which has a higher U value.
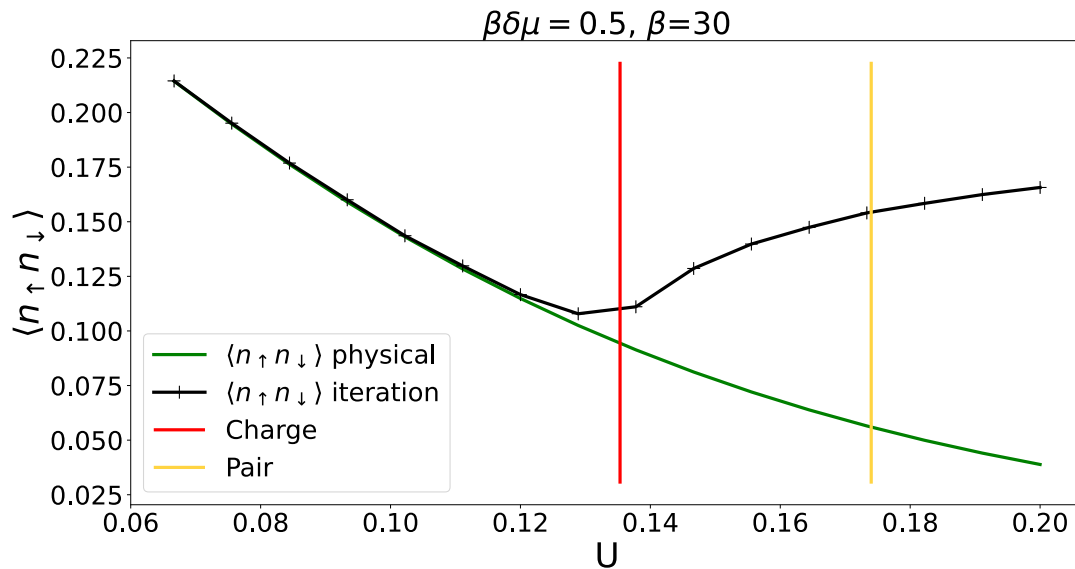
Figure 5.4: Double occupancy of the physical solution and the iteratively obtained solution of the HA plotted for different U values and $\beta\delta\mu = 0.5$. The red vertical line marks the U value of the first vertex divergence in the charge channel, while the yellow vertical line marks the U values of the first divergence in the pairing channel.
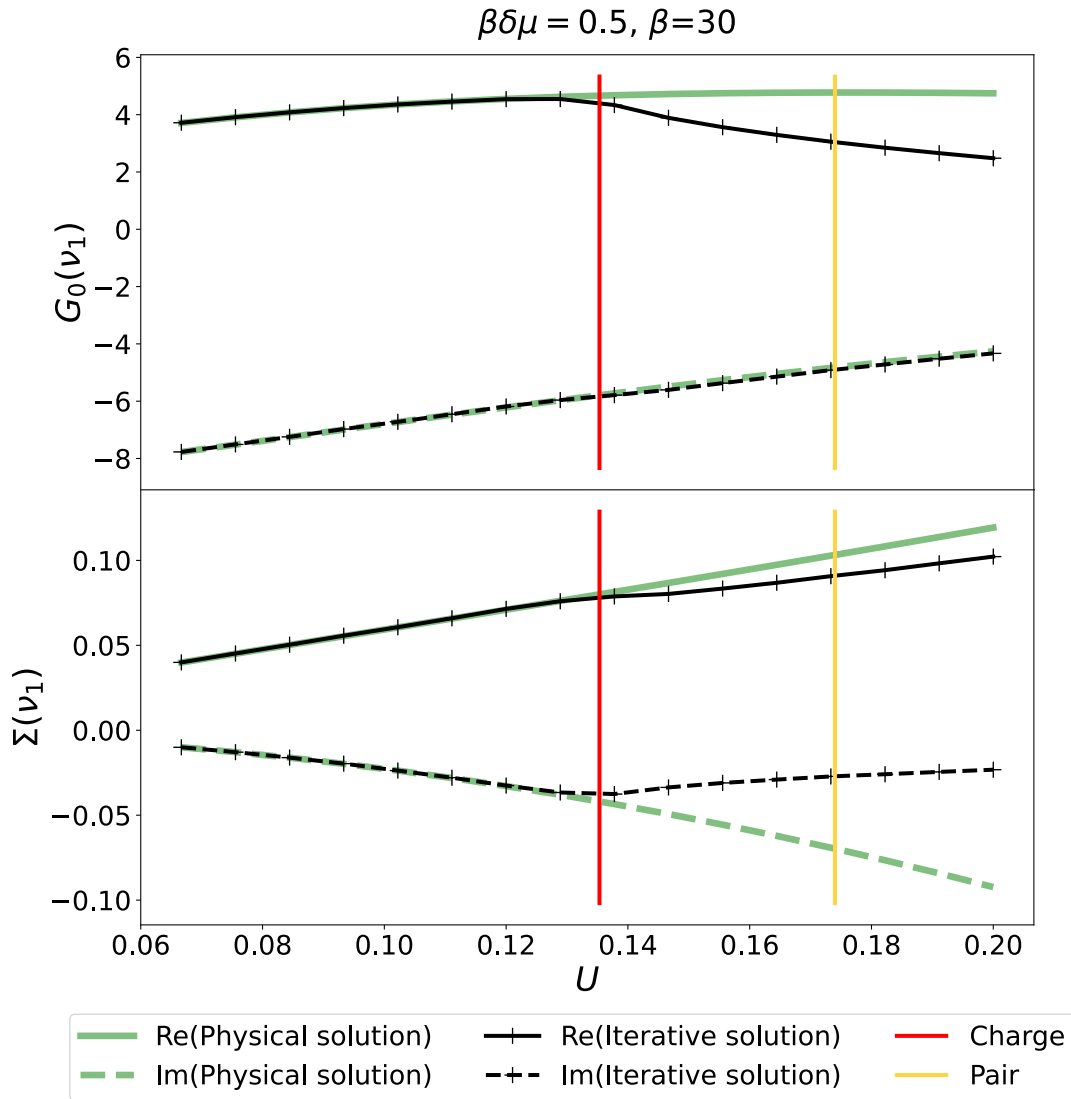
Figure 5.5: **Upper:** The physical and the iteratively obtained $G_0(\nu_1)$ of the HA plotted for different U values. **Lower:** The physical and the iteratively obtained $\Sigma(\nu_1)$ of the HA plotted for different U values at $\delta\mu = 0.5$ and $\beta = 30$. The red vertical line marks the U value of the first vertex divergence in the charge channel, while the yellow vertical line marks the U values of the first divergence in the pairing channel.

As it can be seen in Figs. 5.4, 5.5 the convergence to an unphysical solution begins when crossing the charge divergence at the lowest U value. This happens continuously, like for half filling, and, thus, we get qualitatively the same behavior as in the half filling case. Again, the crossing of the second charge divergence or the crossing of the pairing divergence has no effect on the convergence. To some extent these results were already, at least implicitly, known because of the proof in Ref. [12] and the data at half filling in Ref. [20].

On the other hand, the numerical data in [18], though not conclusive, seem somehow to suggest that *also* the pseudo-divergences, as defined in section 4.2, may have some effect on the self-consistent perturbation theory.

Therefore, we will investigate what happens if we cross a non-perturbative pseudo-divergence,

e.g. pseudo-divergences that stem from the loop structure of the vertex divergence lines in the phase diagram (see section 4.2). To this aim, we use the iterative scheme of Eq. (5.1) for $\delta\mu$ values *higher* than that of the exceptional point ($\beta\delta\mu = 0.6$). In Fig. 5.6 the iteratively obtained, double occupancy together with the physical double occupancy can be seen along a "left to right" U–path at $\beta\delta\mu = 3$.
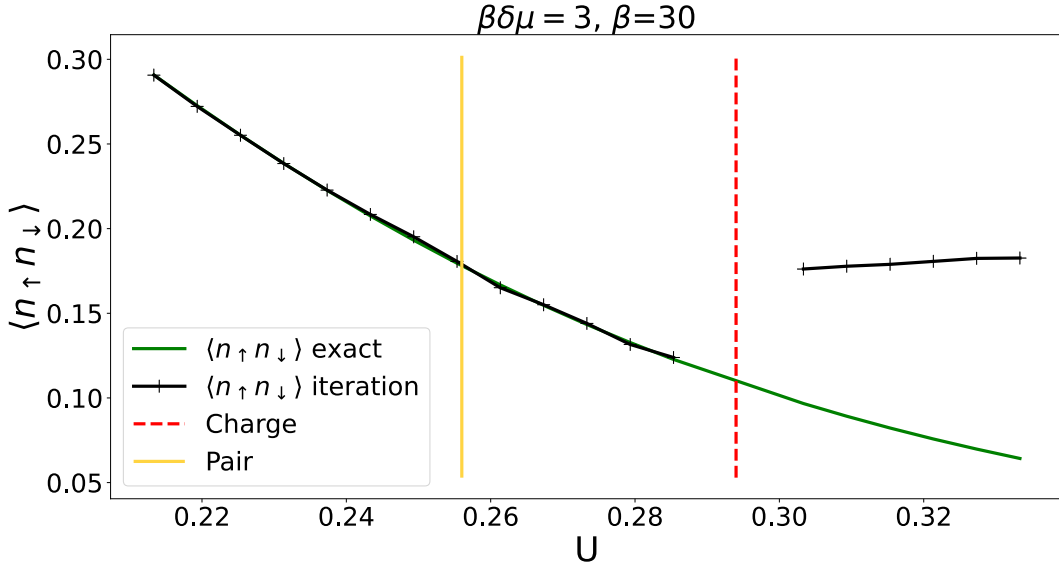
Figure 5.6: Double occupancy of the physical solution and the iteratively obtained solution plotted for different U values and $\beta\delta\mu = 3$. The dashed red vertical line marks the U value of the first non-perturbative pseudo-divergence in the charge channel, while the yellow vertical line marks the U values of the first divergence in the pairing channel.

From the double occupancy in Fig. 5.6 we clearly see that also the crossing of the (non-perturbative) pseudo-divergence in the charge channel represents a barrier for the convergence of our self-consistent algorithm to the physical solution. Therefore, also this kind of pseudo-divergences mark the end of the self-consistent perturbation theory, justifying their classification as "non-perturbative". Moreover, we infer, from the numerical data, that the branch switch to the unphysical solution happens *discontinuously*. The structure of the discontinuity is analyzed by looking at $G_0(\nu_1)$ and $\Sigma(\nu_1)$ in Fig. 5.7.

$$\beta\delta\mu = 3,\ \beta=30$$
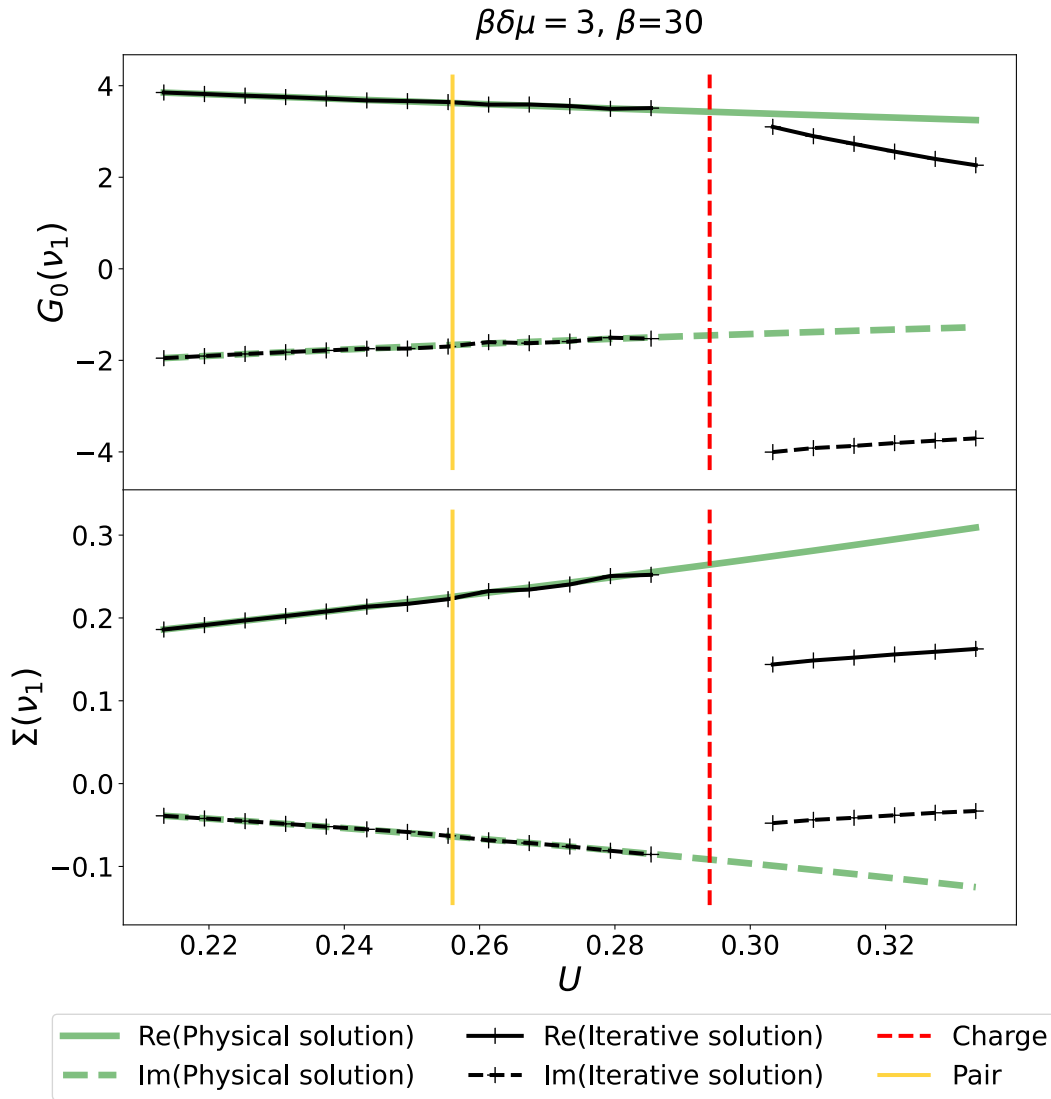
Figure 5.7: **Upper:** The physical and the iteratively obtained $G_0(\nu_1)$ of the HA plotted for different U values. **Lower:** The physical and the iteratively obtained $\Sigma(\nu_1)$ plotted for different U values at $\delta\mu = 3$ and $\beta = 30$. The dashed red vertical line marks the U value of the first non-perturbative pseudo-divergence in the charge channel, while the solid yellow vertical line marks the U values of the first divergence in the pairing channel.

According to the data shown in Fig. 5.7, the switching to the unphysical solution at the pseudo-divergence (red dashed vertical line) is continuous in the real part of G_0, but discontinuous in the imaginary part of G_0 as well as in both real and imaginary part of Σ. We want to emphasize that the branch switch to the unphysical solution at pseudo-divergences needs to be discontinuous in some way, as a continuous switch would imply a vertex divergence [12] leading to a contradiction. On the other hand, in order to make the switch between solutions possible, it is plausible that a link between these must exist. In this case the link appears to be the real part of G_0. More in general one can argue that this link is needed because, otherwise one could not single out the case of the observed switch from the generic situation where infinitely many unphysical solutions, with

no link to the physical solution, exist[1].

Such a discontinuous behavior appears somewhat reminiscent of that of a first order phase-transition in thermodynamics. Indeed, by a closer inspection, one finds, another similarity: We find a *coexistence region* of the physical and the unphysical solution. This coexistence region can be accessed by performing a calculation by means of the iterative scheme from "left to right" and from "right to left", in analogy to the e.g. metal insulator coexistence region in the Mott transition.

These calculations are shown in Fig. 5.8.
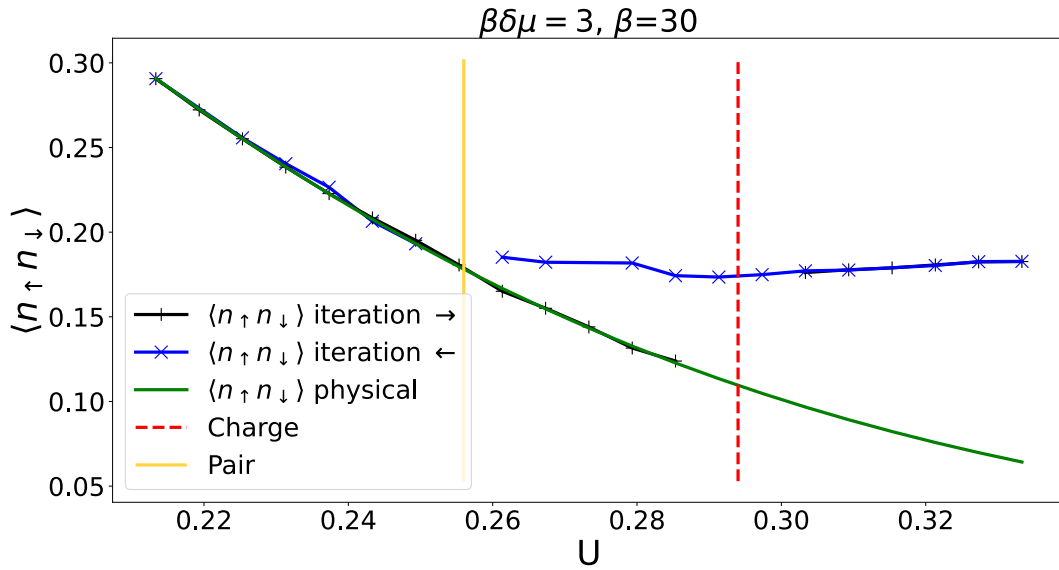
Figure 5.8: Double occupancy of the physical solution and the iteratively obtained solution plotted for different U values and $\beta\delta\mu = 3$. The data plotted with a black line is calculated from "left to right" while the data plotted with a blue line is calculated from "right to left". The dashed red vertical line marks the U value of the first non-perturbative pseudo-divergence in the charge channel, while the solid yellow vertical line marks the U values of the first divergence in the pairing channel.

More precisely, we find that the unphysical regime extends beyond the pseudo-divergence, when calculating the data from "right to left". Remarkably, the branch switch from unphysical to physical solution then happens at the pairing divergence, suggesting a (loose) analogy between the yellow divergence line and the U_{c1} of the Mott MIT.

To further investigate the structure of the branch, we plot again $G_0(\nu_1)$ and $\Sigma(\nu_1)$ in Fig. 5.9.

---

[1]The existence of infinitely many unphysical solutions is suggested by the existence of infinitely many divergences [5, 12, 17]
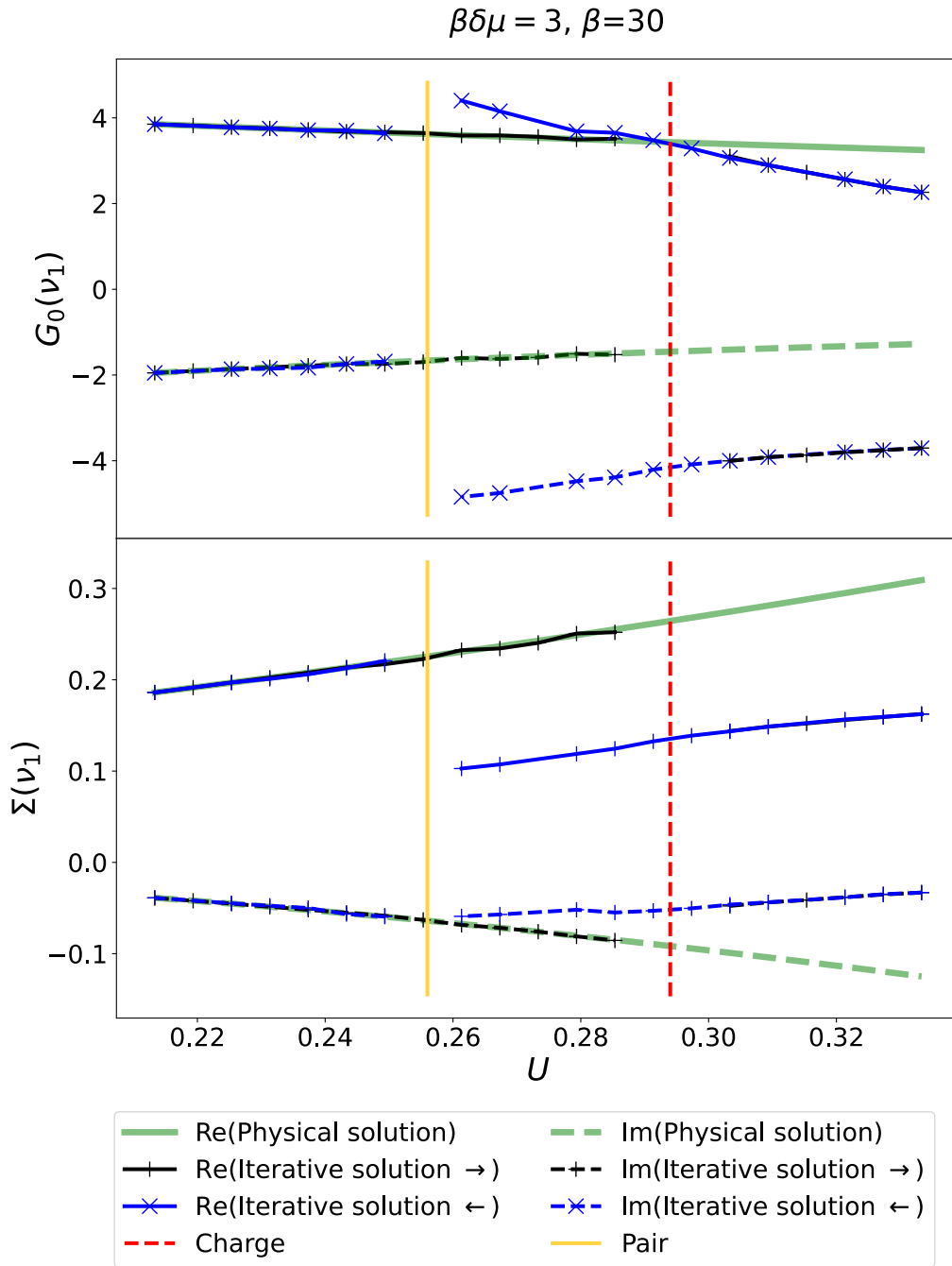
Figure 5.9: **Upper:** The physical and the iteratively obtained $G_0(\nu_1)$ of the HA plotted for different U values. **Lower:** The physical and the iteratively obtained $\Sigma(\nu_1)$ plotted for different U values at $\delta\mu = 3$ and $\beta = 30$. The data plotted with a black line is calculated from "left to right" while the data plotted with a blue line is calculated from "right to left". The dashed red vertical line marks the U value of the first non-perturbative pseudo-divergence in the charge channel, while the solid yellow vertical line marks the U values of the first divergence in the pairing channel.

Notably, the numerical data suggest that the link between the physical and the unphysical solution, when calculating the data from "right to left", is no longer guaranteed by the real part of G_0, as it is the case for the calculation from "left to right", but by the imaginary part of Σ, since the

73

imaginary of Σ appears (numerically) continuous at the branch switch while all other quantities are discontinuous.

This insight raises the question of what happens if the pseudo-divergence in the charge channel occurs at lower U values than the pairing divergence, as it is the case for $0.6 < |\beta\delta\mu| < 1.75$.

It turns out that the convergence of our iterative scheme in this region is very challenging due to very strong oscillations during the iterations. These oscillations can be suppressed by mixing different iteration steps, as described in section 5.1. But our data suggest that in this parameter regime of strong oscillations rather leads to a sort of Maxwell-construction-like interpolation between the physical and the unphysical solution, instead of a proper convergence to a given solution (see appendix A.6 for more information). Therefore, only converged data that are obtained without mixing are presented in the main text for $0.6 < |\beta\delta\mu| < 1.75$, where the oscillations are very strong and the charge pseudo-divergence is located at lower U values than the pairing divergence. In Figs. 5.10, 5.11 data for $\beta\delta\mu = 0.7$ calculated from "left to right" and from "right to left" *without* mixing are presented.
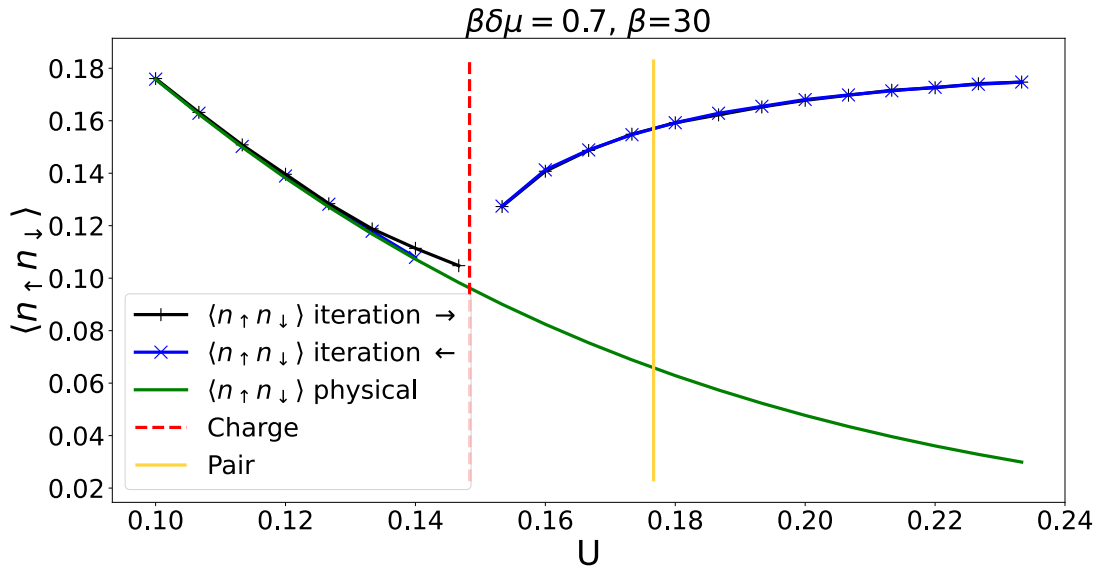
Figure 5.10: Double occupancy of the physical solution and the iteratively obtained solution plotted for different U values at $\beta\delta\mu = 0.7$ and $\beta = 30$. The data plotted with a black line is calculated from "left to right" while the data plotted with a blue line is calculated from "right to left". The red dashed vertical line marks the U value of the first non-perturbative pseudo-divergence in the charge channel, while the solid yellow vertical line marks the U values of the first divergence in the pairing channel. The small deviation from the physical solution right before the charge pseudo-divergence is interpreted as numerical error. The numerical error associated to the iterative scheme seems to happen near the exceptional point, see also Fig. 5.4.

No coexistence region is found for the cases where the charge pseudo-divergence is located at smaller U values than the pairing divergence. This can be seen in Fig. 5.10, where the branch switch occurs at the pseudo-divergence in the charge channel for both "left to right" and "right to left". For a more detailed analysis, we must again closely inspect the behavior of $G_0(\nu_1)$ and

$\Sigma(\nu_1)$ in Fig. 5.11.

Since a continuous branch switch would imply a divergence in the charge channel [12], which is not observed in this parameter regime, the branch switch must be discontinuous.

Because we are near the exceptional point ($\beta\delta\mu = 0.6$) the discontinuous jump is very small, and it is very hard to numerically identify which parts of G_0 and Σ are continuous and which are discontinuous.
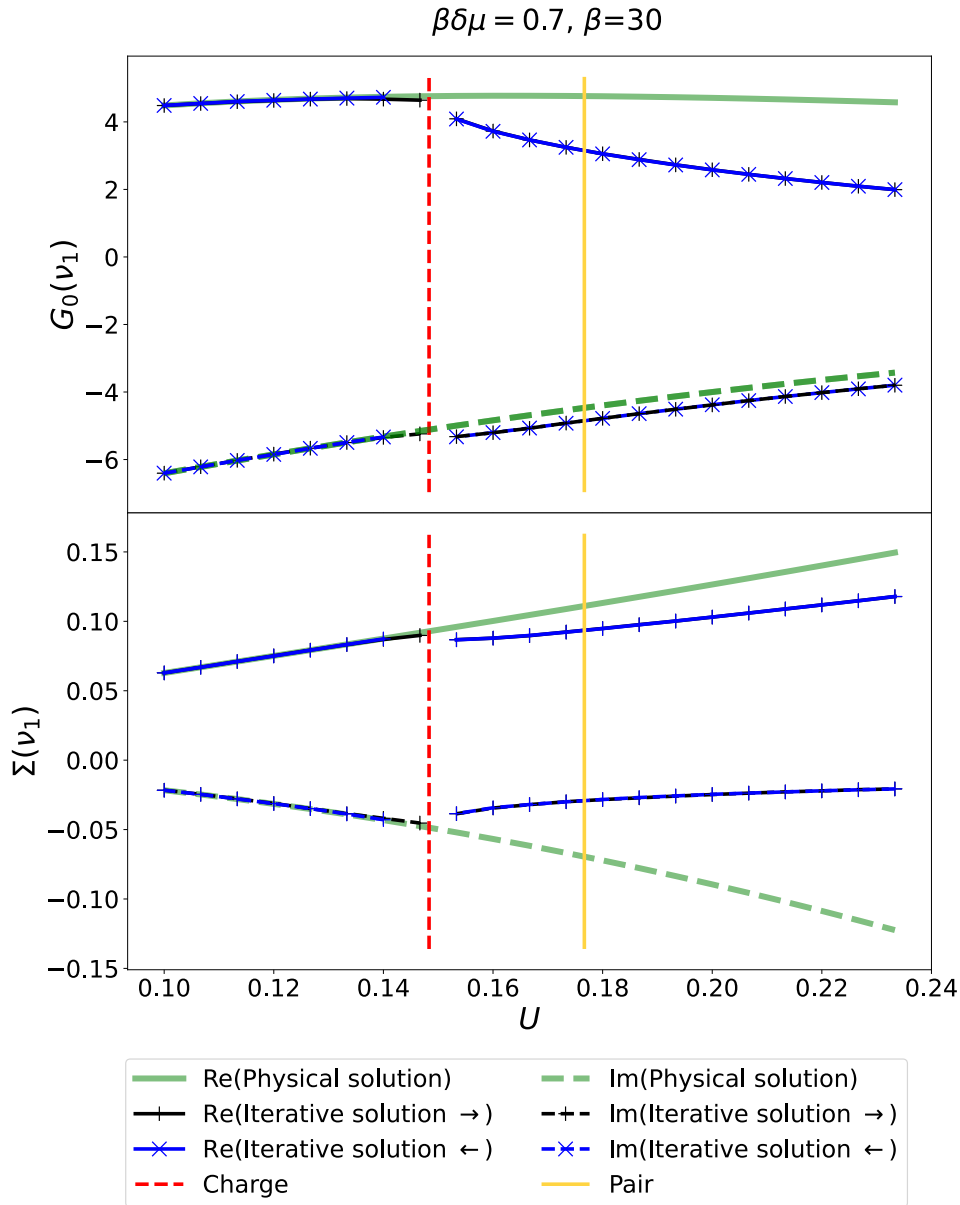
Figure 5.11: **Upper:** The physical and the iteratively obtained $G_0(\nu_1)$ of the HA plotted for different U values. **Lower:** The physical and the iteratively obtained $\Sigma(\nu_1)$ plotted for different U values at $\delta\mu = 0.7$ and $\beta = 30$. The data plotted with a black line is calculated from "left to right" while the data plotted with a blue line is calculated from "right to left". The dashed red vertical line marks the U value of the first non-perturbative pseudo-divergence in the charge channel, while the solid yellow vertical line marks the U values of the first divergence in the pairing channel.

Therefore, more data are needed to provide a solid interpretation for the structure of the branch switch. To this aim, we calculate the difference between the unphysical and the physical solution at the first Matsubara frequency at the U value of the (pseudo-)divergence in the charge channel. The value of the unphysical $G_0(\nu_1)$ (or $\Sigma(\nu_1)$) at the U corresponding to the pseudo-divergence is determined by fitting the calculated values of $G_0(\nu_1)$ (or $\Sigma(\nu_1)$) obtained through our iterative scheme. The fitting process involves a second-degree polynomial in U to which the unphysical $G_0(\nu_1)$ (or $\Sigma(\nu_1)$) in proximity to the pseudo-divergence are fitted. Due to the strong oscillations in the iterative scheme, only data that are calculated *without* mixing is used for the fitting procedure (see appendix A.6).

The difference between the fitted polynomial at the U value of the first (pseudo-)divergence in the charge channel and the physical $G_0(\nu_1)$ (resp. $\Sigma(\nu_1)$) is plotted in Fig. 5.12 for different $\delta\mu$ values and denote by ΔG_0 (resp. $\Delta\Sigma$).
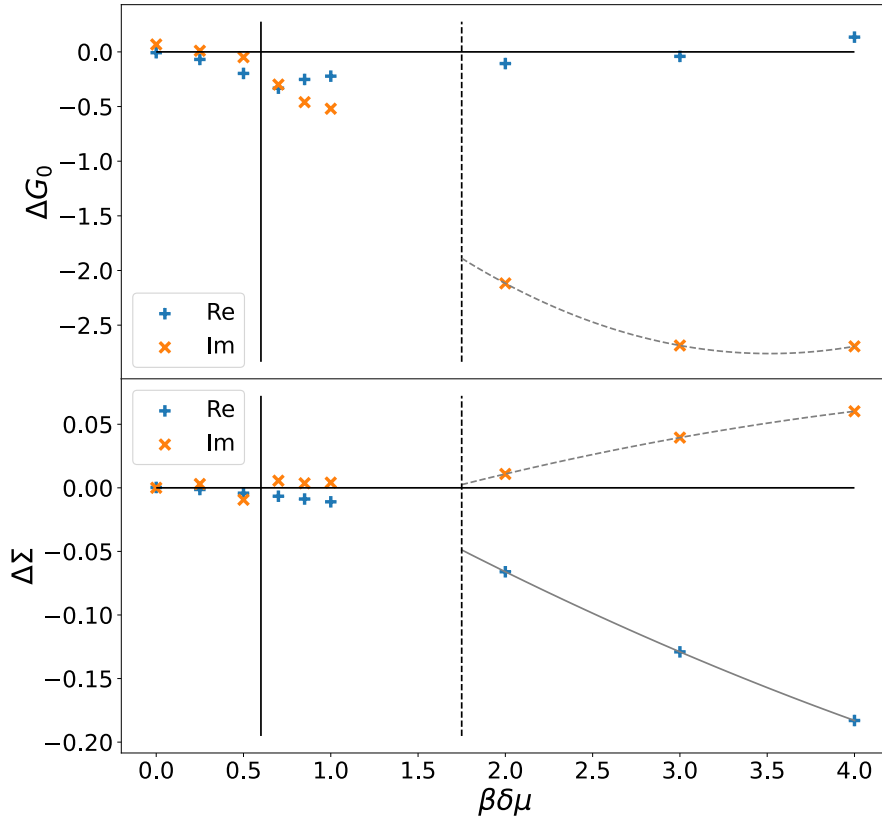
Figure 5.12: **Upper:** Difference between the extrapolated value of $G_0(\nu_1)$ computed with the iterative algorithm and the value of the physical $G_0(\nu_1)$ at the U value of the first (non-perturbative pseudo-)divergence plotted for different $\delta\mu$ values. **Lower:** Difference between the extrapolated value of $\Sigma(\nu_1)$ computed with the iterative algorithm and the value of the physical $\Sigma(\nu_1)$ at the U value of the first (non-perturbative pseudo-)divergence plotted for different $\delta\mu$ values. The black solid vertical line marks the $\beta\delta\mu$ value of the corresponding exceptional point, while the black dashed vertical line marks the $\beta\delta\mu$ value at which the first charge pseudo-divergence line and the first pairing divergence line cross.

We interpret the enhancement of the real part of ΔG_0 observed around the exceptional point, marked by a solid vertical line in Fig. 5.12, as numerical error. This is plausible as the data (especially for $\beta\delta\mu = 0.5$) suggest that the slope of the branch switch gets steeper when approaching the exceptional point and diverge at the exceptional point. Evidently, this makes it hard to get good numerical results in this region, which likely also explains the numerical artefacts seen in Figs. 5.4, 5.10, where the double occupancy appears to slightly deviate from the physical value also right before the pseudo-divergence. A further support of this interpretation is the fact that $\mathrm{Re}(\Delta G_0)$ decreases again when departing from the exceptional point. In contrast, to the clear enhancement in $\mathrm{Im}(\Delta G_0)$ observed for $|\beta\delta\mu| > 0.6$.

At the same time, we do not see a clear trend in the data of $\mathrm{Im}(\Delta\Sigma)$ for $|\beta\delta\mu| < 1.75$, while the value of $\mathrm{Im}(\Delta\Sigma)$ extrapolates to zero for $\beta\delta\mu = 1.75$. This suggests the interpretation that $\mathrm{Im}(\Delta\Sigma)$ is nonzero only for $|\beta\delta\mu| > 1.75$. On the other hand, for $\mathrm{Re}(\Delta\Sigma)$ we do see a clear trend for $|\beta\delta\mu| > 0.6$ which would likely imply that $\mathrm{Re}(\Delta\Sigma)$ is only zero for $|\beta\delta\mu| < 0.6$.

Although our numerical data are not completely conclusive, we present here the simplest possible explanation which is not in contradiction with the whole data sets, in the spirit of the well known concept of Ockham's razor:

(i) A completely continuous switch between physical and unphysical solution occurs at vertex divergences in the charge channel.

(ii) A branch switch that is *only* continuous in the real part of G_0 and the imaginary part of Σ occurs at (non-perturbative) pseudo-divergences that are at lower U values than the pairing divergence for the same $\delta\mu$. This structure unifies the behavior of the two solutions in the coexistence region for $|\beta\delta\mu| > 1.75$, as the "left to right" branch switch is *only* continuous in the real part of G_0 and the "right to left" switch is *only* continuous in the imaginary part of Σ.

(iii) A branch switch that takes place at (non-perturbative) pseudo-divergences that are at higher U values than the pairing divergence for the same $\delta\mu$ is *only* continuous in the real part of G_0 (when the data are calculated from "left to right"). Further, this is the only case where a coexistence of physical and unphysical solution is found: This happens in the parameter region bounded by the pairing divergence from the left and the charge pseudo-divergence from the right.

The three cases that we found for the branch switch from the physical to the unphysical solution are summarized in Tab. 5.1.

	Case	(i)	(ii)	(iii)
	$\beta\delta\mu$	$|\beta\delta\mu| < 0.6$	$0.6 < |\beta\delta\mu| < 1.75$	$|\beta\delta\mu| > 1.75$
	(Pseudo-)Divergences	Charge divergence at lower U than pairing divergence	Charge pseudo-divergence at lower U than pairing divergence	Pairing divergence at lower U than charge pseudo-divergence
	Coexistence region	✗	✗	Between pairing divergence and charge pseudo-divergence
	Branch switch at	Charge divergence	Charge pseudo-divergence	Charge pseudo-divergence (Pairing divergence)
Branch switch is continuous:	$\mathbf{Re}(G_0)$	✓	✓	✓ (✗)
	$\mathbf{Im}(G_0)$	✓	✗	✗
	$\mathbf{Re}(\Sigma)$	✓	✗	✗
	$\mathbf{Im}(\Sigma)$	✓	✓	✗ (✓)

Table 5.1: Summarized properties of the branch switch for all found cases. In the case where a coexistence region exists, the entry in brackets is for the "right to left" solution and the entry without brackets is for the "left to right" solution.

Eventually, we turn to the discussion of the case $\delta\mu < 0$. For $\delta\mu < 0$ our numerical data suggest that we have the same behavior as for $\delta\mu > 0$ but the iterative scheme faces more difficulties to converge for small $\delta\mu$ values which is probably due to the very small value of the double occupancy and the filling characterizing these cases.

Finally, we address the pseudo-divergences in the charge channel that emerge from the discussed parabola structures (see section 4.2) at $U < 0$. To this aim, we calculate the convergence of the iterative scheme for $\beta\delta\mu = 4$ and $U > 0$ Fig. 5.13 and for $\beta\delta\mu = 1.5$ and $U < 0$ Fig. 5.14.

We find that the pseudo-divergences that stem from the parabolas do not lead to a branch switch *neither* in the attractive nor the repulsive sector. This again supports our classification of these pseudo-divergences as "perturbative" pseudo-divergences. Further, the vertex divergences in the attractive sector lead to a completely continuous branch switch similarly as in the repulsive case.
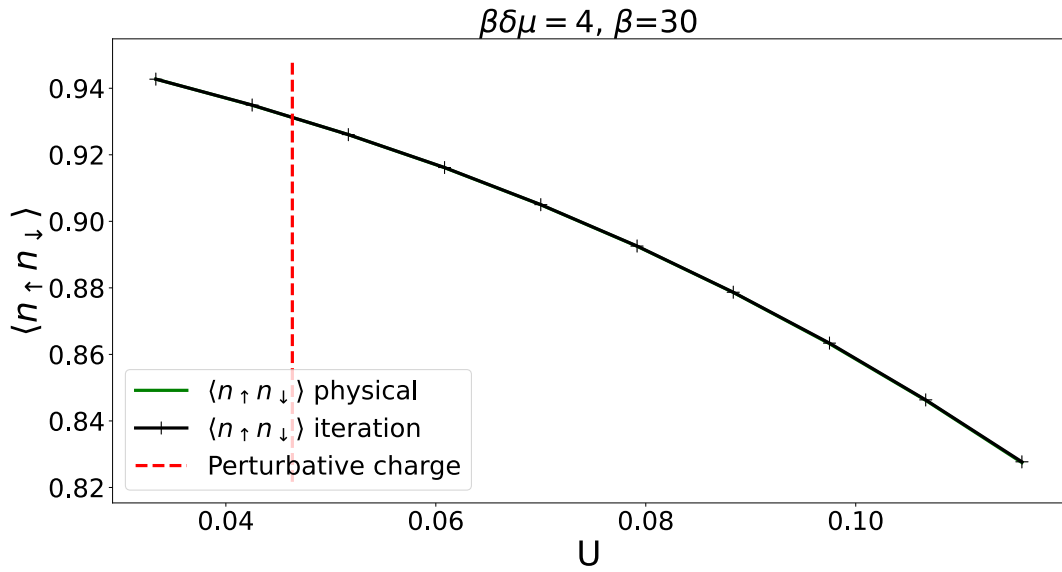
Figure 5.13: Double occupancy of the physical solution and the iteratively obtained solution plotted for different U values at $\beta\delta\mu = 4$. The dashed red vertical line marks the U value of the first perturbative pseudo-divergence in the charge channel.
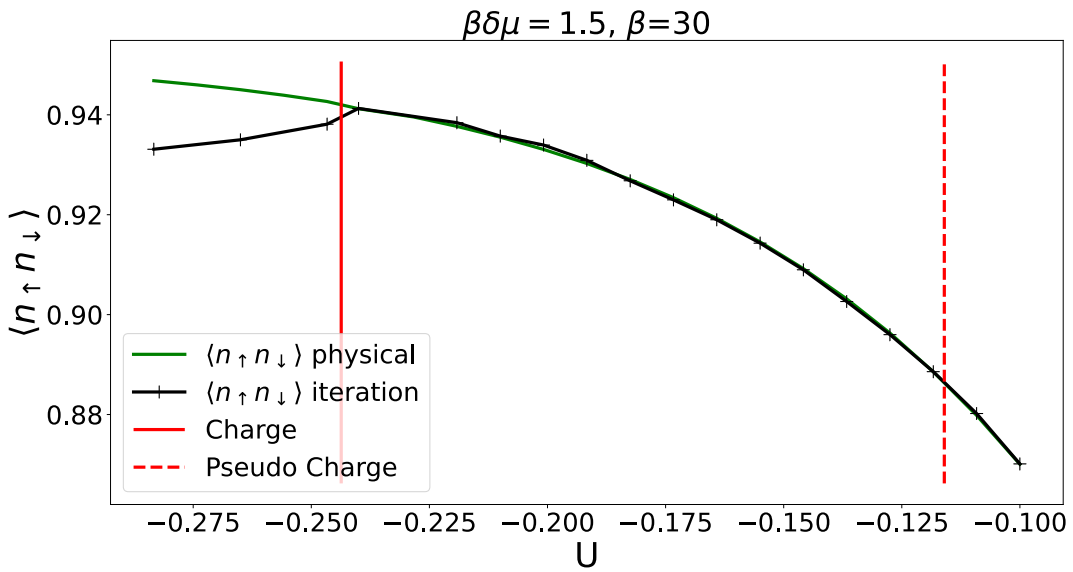
Figure 5.14: Double occupancy of the physical solution and the iteratively obtained solution plotted for different negative U values at $\beta\delta\mu = 1.5$. The solid red vertical line marks the U value of the first divergence in the charge channel, while the dashed red vertical line marks the U value of the first perturbative pseudo-divergence in the charge channel.

Chapter 6

Conclusion and outlook

6.1 Conclusion

In this thesis we managed to successfully extend the existing analyses of the breakdown of the many-electron perturbation expansion, presented in chapter 3, which are manly limited to the particle-hole symmetric case. In particular, we were able to provide a precise answer to the questions posed in section 3.4:

How can the mapping of 2-particle quantities between repulsive and attractive models of Ref. [11] be extended beyond SO(4)-symmetry?

The mapping developed in section 4.1 links local generalized susceptibilities calculated for systems that are invariant under rotations in the spin-space to the corresponding ones of systems that are invariant under rotations in the pseudospin-space. This corresponds to relating a system beyond particle-hole symmetry without external magnetic field to a corresponding one with particle-hole symmetry but with external magnetic field and a sign flip in the interaction. Our derivation demonstrates that, consistent with the results of [11], the symmetric real part of the generalized susceptibilities is mapped from the charge to the spin channel (or vice versa), while the antisymmetric real part is invariant under the mapping. At the same time, the imaginary parts of the generalized susceptibilities beyond particle-hole symmetry get mapped to the generalized susceptibilities that couple the charge and the spin channel for the corresponding SU(2)-broken system.

How do the vertex divergences behave beyond particle-hole symmetry?

In section 4.2 we have investigated the structure of the vertex divergences, which correspond to a vanishing eigenvalue in the generalized susceptibility, in the Hubbard Atom beyond particle-hole symmetry both for repulsive and attractive interaction.

Additionally, we find that a $(N+1)$-dimensional phase space of a general many-electron model at finite T that depends on the N parameters $\{\varepsilon_i\}|_{i=1}^{N}$ can be reduced to a N-dimensional phase space by considering the dimensionless parameters $\beta\varepsilon_i$ without losing any information about the generalized susceptibilities.

Since the eigenvalues of the generalized susceptibility out of half filling can be either real or complex conjugate pairs, we define the pseudo-divergence We also search for the presence of

"pseudo-divergences", in addition to the location of vertex divergences. Pseudo-divergences occur, according to our definition, when the generalized susceptibility has a complex conjugate pair of eigenvalues with vanishing real part but finite imaginary part.

By searching for divergences and pseudo-divergences in the reduced parameter space $\{\beta\delta\mu, \beta U\}$-space, we find the following results:

In the repulsive sector only charge and pairing (pseudo-)divergences occur. Two charge divergence lines in the repulsive sector form a closed "loop" structure in parameter space, where the point where the two divergence lines meet is identified as an exceptional point[1]. Further, a pseudo-divergence line emerges from each exceptional point by increasing doping. Moreover, the pairing divergence lines beyond particle-hole symmetry deviate from the symmetric charge divergence lines due to the violation of the pseudospin SU(2)-symmetry.

In the attractive sector, only charge and spin (pseudo-)divergences are found, whereas both channels share a similar structure of the (pseudo-)divergence lines. For both channels, two divergence lines meet at an exceptional point, from where a pseudo-divergence line emerges. In contrast to the repulsive sector the divergence lines do not form a closed structure but rather a parabola structure that extend to $U \to -\infty$. Interestingly, the pseudo-divergence lines of these parabolas cross the $U = 0$-axis and extend into the repulsive sector (cf. Fig. 4.1).

Further, by using the developed mapping, we can also obtain the divergence lines for a Hubbard Atom at half filling with external magnetic field without performing the respective calculations as discussed in section 4.4.

How does the $T = 0$ limit behave?

In appendix A.4, we have developed a procedure which allows to investigate the $T = 0$ limit of the generalized susceptibilities. Equipped with this scheme, we study the structure of the eigenspectra of the generalized susceptibilities expressed in terms of the imaginary frequencies at $T = 0$ in section 4.3. A remarkable outcome of this analysis is the following: We find a non-perturbative region, with a continuous distribution of pseudo-divergences and divergences, in the whole phase space enclosed in $0 < \mu < U$ with $U > 0$ and for the specific value of $\mu = U/2$ for $U < 0$. Further, we classify the pseudo-divergences as "perturbative" and "non-perturbative" pseudo-divergences, which are characterized by a different structure of the spectrum (see Fig. 4.12). The non-perturbative pseudo-divergences correspond to the pseudo-divergences that emerge from the "loop structures" at finite temperature, while the perturbative divergences stem from the parabola structures.

How does the misleading convergence of self-consistent perturbation theory happen beyond particle-hole symmetry?

In chapter 5 we investigate the convergence of the self-consistent perturbation theory beyond particle-hole symmetry by means of an iterative scheme first adapted in Ref. [20]. This way, we find a misleading convergence of the iterative scheme for different values of the chemical potential. In particular, for $|\beta\delta\mu| < 0.6$, where we still find divergences in the charge channel by increasing the value of βU and no pseudo-divergences the situation remains qualitatively similar to the half

---

[1]exceptional points are points where the algebraic multiplicity of an eigenvalue is bigger than the geometric multiplicity [42]

filling case: The convergence to an unphysical solution starts by crossing the first divergence in the charge channel (see Fig. 5.4).

For $|\beta\delta\mu| > 0.6$, instead, we have pseudo-divergences in the charge channel, there we find that also the crossing of the first non-perturbative pseudo-divergence leads to an unphysical convergence of the iterative scheme (see Fig. 5.10) which, as mentioned before, resembles the self-consistent perturbation theory while the crossing of a perturbative pseudo-divergence does not lead to an unphysical convergence of the scheme (see Figs. 5.13, 5.14).

Further, consistent with a loose analogy with the properties of a 1st order phase transition, we find a coexistence region for the physical and the unphysical solution between the pairing divergence and the non-perturbative pseudo-divergence if the pairing divergence occurs at smaller U values than the pseudo-divergence, which is the case for $|\beta\delta\mu| > 1.75$. In particular, following a U-path from lower to larger U values the iterative scheme starts to converge to an unphysical solution after crossing the first pseudo-divergence in the charge channel, but following the same U−path in the opposite direction, the convergence to an unphysical solution also takes place for U values smaller than the U value of the first pseudo-divergence and only terminates for U values smaller than the U value of the first pairing divergence (see Fig. 5.8).

Moreover, our investigations have demonstrated that, when the misleading convergence is caused by the crossing of the divergence in the charge channel, the corresponding deviation from the physical solution occurs continuously regardless of whether one considers the at half filling or the out of half filling case (see Figs. 5.3, 5.5).

On the other hand, when the misleading convergence is caused by a non-perturbative pseudo-divergence, the situation becomes more complicated.

For $0.6 < |\beta\delta\mu| < 1.75$, where the charge pseudo-divergence occurs at smaller U values than the pairing divergence, we do not have conclusive data due to the strong oscillations in our self-consistent procedure. However, we suspect that the branch switch between the physical and the unphysical solution happens continuous in the real part of G_0 and the imaginary part of Σ, while it probably displays a discontinuous jump in the imaginary part of G_0 and the real part of Σ (see Figs. 5.11, 5.12). Further, we suspect that no coexistence region of the physical and the unphysical solution exists in this case.

For $|\beta\delta\mu| > 1.75$ where the charge pseudo-divergence is at larger U values than the pairing divergence, we find a coexistence region between the charge pseudo-divergence and the pairing divergence. If the branch switch occurs at the charge pseudo-divergence (e.g. considering a path with increasing U) only the real part of G_0 appears to be continuous. Instead, only the imaginary part of Σ appears to be continuous if the branch switch occurs at the pairing divergence (e.g. on the opposite path with decreasing U) as it can be seen in Fig. 5.9.

The findings of misleading convergence are summarized in Tab. 5.1.

6.2 Outlook

Although we were able to answer the posed questions, taking a first step towards a systematic understanding of the perturbative breakdown beyond particle-hole symmetry, some relevant questions still need to be addressed.

A very natural extension would be to break further symmetries, e.g. investigate the (pseudo-)divergences of the Hubbard Atom for the most general case: beyond particle-hole symmetry *and* in the presence of an external magnetic field. By deriving the mapping for the most general case where neither SU(2) nor particle-hole symmetry are fulfilled one only needs to consider the repulsive system and can obtain the attractive model with this mapping (or vice versa), for this our developed framework should be very convenient.

Also, the difference between the non-perturbative and the perturbative pseudo-divergences remains to be understood. To this aim, a closer examination of the non-perturbative structure in the spectra of the generalized susceptibilities, best seen in the $T = 0$ limit, could be interesting.

Further, a more precise investigation of the structure of the misleading convergence of our iterative scheme, especially in the region $0.6 < |\beta\delta\mu| < 1.75$, where the charge pseudo-divergence occurs at smaller U values than the pairing divergence for which our data are not very conclusive, needs to be done. The final goal of this investigation would be to develop an analytical proof like the one in Ref. [12] for non-perturbative pseudo-divergences. In this respect, a possible direction to be followed, which looks quite promising, is the examination of the vertex divergences occurring for complex values of the interaction. Their occurrence in the complex interaction plane could be linked directly to the non-perturbative pseudo-divergences, as suggested by the preliminary data in Ref. [53]. Moreover, we note that the analysis of complex interactions has also been used in the context of diagrammatic Monte Carlo calculations for a determination of the convergence radii of the method itself [54].

Finally, the investigation of other models needs to be done. Interesting cases would be: **(i)** The Falicov-Kimball model solved with DMFT, because the functional form of its self energy as functional of the full Green's function is analytically known [17]. **(ii)** The Hubbard Dimer as well as the Hubbard model solved with cluster DMFT methods [18, 55] to investigate the effect of non-local spacial correlations on the breakdown of perturbation theory. **(iii)** A two orbital impurity model with magnetic coupling to fully clarify the supposed connection between the breakdown of perturbation theory and the violation of the Luttinger theorem [48–50].

Appendix A

Appendix

A.1 Analytical expression for the generalized susceptibility in the Hubbard Atom without magnetic field

The 1-particle Green's function and the connected 2-particle Green's functions for the HA in ph-notation (if no explicit ph or pp index is present, the quantity is expressed in ph-notation) for different spin combinations are shown in Eqs. (A.1) to (A.3).

$$G_1^{T=0}(\nu) = \frac{1-n}{i\nu + \mu} + \frac{n}{i\nu + \mu - U}, \tag{A.1}$$

$$G_{2,\uparrow\uparrow}^{T=0,c}(\nu,\nu',\omega) = \frac{U^2 n(1-n)(\delta(\omega) - \delta(\nu - \nu'))}{(i(\nu+\omega)+\mu)(i(\nu+\omega)+\mu-U)(i\nu'+\mu)(i\nu'+\mu-U)} \tag{A.2}$$

and

$$G_{2,\uparrow\downarrow}^{T=0,c}\left(\nu,\nu',\omega\right) =$$

$$= \frac{2n-1}{i(\nu+\omega)+i\nu'+2\mu-U}\left(\frac{1}{i(\nu+\omega)+\mu-U}+\frac{1}{i\nu'+\mu-U}\right)\left(\frac{1}{i\left(\nu'+\omega\right)+\mu-U}+\frac{1}{i\nu+\mu-U}\right)$$

$$+ \frac{-\beta e^{\beta(U+\mu)}\delta_{\nu\nu'}}{(2e^{\beta\mu}+1)e^{\beta U}+e^{2\beta\mu}}\left(\frac{1}{i(\nu+\omega)+\mu}-\frac{1}{i\left(\nu'+\omega\right)+\mu-U}\right)\left(\frac{1}{i\nu+\mu}-\frac{1}{i\nu'+\mu-U}\right)$$

$$+ \frac{\beta U^2 \delta_{\omega 0}\left(e^{(2\mu-U)\beta}-e^{2\mu\beta}\right)}{\left(1+2e^{\mu\beta}+e^{(2\mu-U)\beta}\right)^2}\frac{1}{(i(\nu+\omega)+\mu)(i(\nu+\omega)+\mu-U)(i\nu'+\mu)(i\nu'+\mu-U)}$$

$$+ \frac{n-1}{(i(\nu+\omega)+\mu)\left(i\left(\nu'+\omega\right)+\mu-U\right)(i\nu+\mu)}+\frac{1-n}{(i(\nu+\omega)+\mu)(i\nu'+\mu-U)\left(i\left(\nu'+\omega\right)+\mu-U\right)}$$

$$+ \frac{1-n}{(i(\nu+\omega)+\mu-U)(i\nu'+\mu)\left(i\left(\nu'+\omega\right)+\mu-U\right)}+\frac{n-1}{(i\nu'+\mu)\left(i\left(\nu'+\omega\right)+\mu-U\right)(i\nu+\mu)}$$

$$+ \frac{1-n}{(i(\nu+\omega)+\mu)(i\nu'+\mu)(i\nu+\mu)}+\frac{1-n}{(i(\nu+\omega)+\mu)(i\nu'+\mu)\left(i\left(\nu'+\omega\right)+\mu\right)}$$

$$+ \frac{1-n}{(i(\nu+\omega)+\mu-U)\left(i\left(\nu'+\omega\right)+\mu\right)(i\nu+\mu-U)}+\frac{n-1}{(i(\nu+\omega)+\mu-U)(i\nu'+\mu)\left(i\left(\nu'+\omega\right)+\mu\right)}$$

$$+ \frac{1-n}{(i\nu'+\mu-U)\left(i\left(\nu'+\omega\right)+\mu\right)(i\nu+\mu-U)}+\frac{n-1}{(i(\nu+\omega)+\mu)(i\nu'+\mu-U)\left(i\left(\nu'+\omega\right)+\mu\right)}$$

$$+ \frac{-n}{(i(\nu+\omega)+\mu-U)(i\nu'+\mu-U)(i\nu+\mu-U)}+\frac{-n}{(i(\nu+\omega)+\mu-U)(i\nu'+\mu-U)\left(i\left(\nu'+\omega\right)+\mu-U\right)},$$

$$(A.3)$$

where the superscript c in the Green's functions means that only the connected part of the Green's functions is considered and n is the occupation number of each spin (which is equal for spin up and down in the SU(2) symmetric case)

$$n = \frac{e^{\mu\beta}+e^{(2\mu-U)\beta}}{1+2e^{\mu\beta}+e^{(2\mu-U)\beta}}. \tag{A.4}$$

The corresponding generalized susceptibilities are defined in Eqs. (A.5), (A.6)

$$\chi_{\uparrow\uparrow}^{\nu\nu'\omega} = G_{2,\uparrow\uparrow}^c(\nu,\nu',\omega) - \beta G_1(\nu)G_1(\nu+\omega)\delta_{\nu\nu'} \tag{A.5}$$

and

$$\chi_{\uparrow\downarrow}^{\nu\nu'\omega} = G_{2,\uparrow\downarrow}^c(\nu,\nu',\omega). \tag{A.6}$$

The explicit expression for the generalized charge/spin susceptibility as defined in Eq. (2.43) is given in Eq. (A.7)

$$\chi_{c/s}^{\nu\nu'} = -\beta \left[\frac{1-n}{i\nu+\mu} + \frac{n}{i\nu+\mu-U} \right]^2 \delta_{\nu\nu'} + \frac{\beta U^2 n(1-n)(1-\delta_{\nu\nu'})}{(i\nu+\mu)(i\nu+\mu-U)(i\nu'+\mu)(i\nu'+\mu-U)}$$

$$\pm \frac{2n-1}{i\nu+i\nu'+2\mu-U}\left(\frac{1}{i\nu+\mu-U} + \frac{1}{i\nu'+\mu-U} \right)^2$$

$$\pm \frac{-\beta e^{\beta(U+\mu)}\delta_{\nu\nu'}}{(2e^{\beta\mu}+1)e^{\beta U}+e^{2\beta\mu}}\left(\frac{1}{i\nu+\mu} - \frac{1}{i\nu'+\mu-U} \right)^2$$

$$\pm \frac{\beta U^2\left(e^{(2\mu-U)\beta}-e^{2\mu\beta} \right)}{\left(1+2e^{\mu\beta}+e^{(2\mu-U)\beta}\right)^2}\frac{1}{(i\nu+\mu)(i\nu+\mu-U)(i\nu'+\mu)(i\nu'+\mu-U)}$$

$$\pm \frac{n-1}{(i\nu+\mu)(i\nu'+\mu-U)(i\nu+\mu)} \pm \frac{1-n}{(i\nu+\mu)(i\nu'+\mu-U)(i\nu'+\mu-U)} \quad \text{(A.7)}$$

$$\pm 2\left(\frac{1-n}{(i\nu+\mu-U)(i\nu'+\mu)(i\nu'+\mu-U)} + \frac{n-1}{(i\nu'+\mu)(i\nu'+\mu-U)(i\nu+\mu)} \right)$$

$$\pm \frac{1-n}{(i\nu+\mu)(i\nu'+\mu)(i\nu+\mu)} \pm \frac{1-n}{(i\nu+\mu)(i\nu'+\mu)(i\nu'+\mu)}$$

$$\pm \frac{1-n}{(i\nu+\mu-U)(i\nu'+\mu)(i\nu+\mu-U)} \pm \frac{n-1}{(i\nu+\mu-U)(i\nu'+\mu)(i\nu'+\mu)}$$

$$\pm \frac{-n}{(i\nu+\mu-U)(i\nu'+\mu-U)(i\nu+\mu-U)} \pm \frac{-n}{(i\nu+\mu-U)(i\nu'+\mu-U)(i\nu'+\mu-U)}.$$

The corresponding particle-particle quantities can be obtained by the frequency shift Eq. (2.33) and using the definition of the generalized susceptibility in the pairing channel Eq. (2.45).

For the prefactor in the second line of Eq. (A.7) the limit towards $\mu \to U/2$ needs to be taken carefully:

$$q_0 = \frac{2n-1}{i\nu+i\nu'+2\mu-U} \xrightarrow{\mu\to U/2} \frac{\beta\delta_{\nu,-\nu'}}{2(1+e^{\beta\mu})}. \quad \text{(A.8)}$$

A.2 Derivation of the mapping beyond SO(4)-symmetry

In this section the calculations for section 4.1 are done in more detail. For this we start by showing how the orthogonal transformation Q in Eq. (4.12) separates the symmetric and antisymmetric parts of a centro-hermitian matrix. A centro-hermitian matrix χ_{CH} can be represented by the sum of a centro-symmetric real matrix χ' and a skew-centro-symmetric imaginary matrix χ'' [1]

$$\chi_{CH} = \chi' + i\chi'' \quad \text{with} \quad \chi' = \begin{pmatrix} A' & JC'J \\ C' & JA'J \end{pmatrix} \quad \text{and} \quad \chi'' = \begin{pmatrix} A'' & -JC''J \\ C'' & -JA''J \end{pmatrix}, \quad \text{(A.9)}$$

where $\chi'^{(\prime)}$, $A'^{(\prime)}$ and $C'^{(\prime)}$ are real square matrices.

---
[1] Centro-hermitian matrix: $JAJ = A^*$, centro-symmetric matrix: $JAJ = A$, skew-centro-symmetric matrix: $JAJ = -A$, with $J = \begin{pmatrix} & & 1 \\ & \ddots & \\ 1 & & \end{pmatrix}$

The transformation Q acts on (skew-)centro-symmetric matrices as follows[2]

$$Q\chi'Q^T = \begin{pmatrix} A' - JC' & \mathbb{0} \\ \mathbb{0} & A' + JC' \end{pmatrix} \quad \text{and} \quad Q\chi''Q^T = \begin{pmatrix} \mathbb{0} & A'' - JC'' \\ A'' + JC'' & \mathbb{0} \end{pmatrix}. \tag{A.10}$$

To understand why $A' - JC'$ and $A'' + JC''$ are termed antisymmetric blocks and $A' + JC'$ and $A'' - JC''$ are termed symmetric blocks, we let χ' and χ'' act on a vector v which is decomposed into symmetric and antisymmetric parts

$$\begin{pmatrix} A' & JC'J \\ C' & JA'J \end{pmatrix} \left[\begin{pmatrix} v_{\mathcal{S}} \\ Jv_{\mathcal{S}} \end{pmatrix} + \begin{pmatrix} v_{\mathcal{A}} \\ -Jv_{\mathcal{A}} \end{pmatrix} \right] = \begin{pmatrix} (A' + JC')v_{\mathcal{S}} + (A' - JC')v_{\mathcal{A}} \\ (C' + JA')v_{\mathcal{S}} + (C' - JA')v_{\mathcal{A}} \end{pmatrix} \tag{A.11}$$

and

$$\begin{pmatrix} A'' & -JC''J \\ C'' & -JA''J \end{pmatrix} \left[\begin{pmatrix} v_{\mathcal{S}} \\ Jv_{\mathcal{S}} \end{pmatrix} + \begin{pmatrix} v_{\mathcal{A}} \\ -Jv_{\mathcal{A}} \end{pmatrix} \right] = \begin{pmatrix} (A'' - JC'')v_{\mathcal{S}} + (A'' + JC'')v_{\mathcal{A}} \\ (C'' - JA'')v_{\mathcal{S}} + (C'' + JA'')v_{\mathcal{A}} \end{pmatrix}. \tag{A.12}$$

As it can be seen $A' - JC'$ and $A'' + JC''$ couple to the antisymmetric part of the vector and $A' + JC'$ and $A'' - JC''$ couple to the symmetric part of the vector.

Now defining $\chi_{\uparrow\uparrow,\delta\mu}$ and $\chi_{\uparrow\downarrow,\delta\mu}$ as

$$\chi_{\uparrow\uparrow,\delta\mu} = \begin{pmatrix} A' & JB'J \\ B' & JA'J \end{pmatrix} + i \begin{pmatrix} A'' & -JB''J \\ B'' & -JA''J \end{pmatrix} \quad \text{and} \quad \chi_{\uparrow\downarrow,\delta\mu} = \begin{pmatrix} C' & JD'J \\ D' & JC'J \end{pmatrix} + i \begin{pmatrix} C'' & -JD''J \\ D'' & -JC''J \end{pmatrix} \tag{A.13}$$

we find that

$$\mathcal{Q}\chi_{\delta\mu}\mathcal{Q}^T = \begin{pmatrix} Q\chi_{c,\delta\mu}Q^T & \mathbb{0} \\ \mathbb{0} & Q\chi_{s,\delta\mu}Q^T \end{pmatrix} = \begin{pmatrix} \chi'_{c,\delta\mu,\mathcal{A}} & i\,\chi''_{c,\delta\mu,\mathcal{S}} & \\ i\,\chi''_{c,\delta\mu,\mathcal{A}} & \chi'_{c,\delta\mu,\mathcal{S}} & \mathbb{0} \\ & & \chi'_{s,\delta\mu,\mathcal{A}} & i\,\chi''_{s,\delta\mu,\mathcal{S}} \\ \mathbb{0} & & i\,\chi''_{s,\delta\mu,\mathcal{A}} & \chi'_{s,\delta\mu,\mathcal{S}} \end{pmatrix}, \tag{A.14}$$

with

$$\chi'_{c,\delta\mu,\mathcal{A}} = A' - JB' + C' - JD', \quad \chi'_{c,\delta\mu,\mathcal{S}} = A' + JB' + C' + JD',$$
$$\chi''_{c,\delta\mu,\mathcal{A}} = A'' + JB'' + C'' + JD'', \quad \chi''_{c,\delta\mu,\mathcal{S}} = A'' - JB'' + C'' - JD'', \tag{A.15}$$

---

[2]with $Q = \begin{pmatrix} \mathbb{1} & -J \\ \mathbb{1} & J \end{pmatrix}$

and

$$\chi'_{s,\delta\mu,\mathcal{A}} = A' - JB' - C' + JD', \ \chi'_{s,\delta\mu,\mathcal{S}} = A' + JB' - C' - JD',$$
$$\chi''_{s,\delta\mu,\mathcal{A}} = A'' + JB'' - C'' - JD'', \ \chi''_{s,\delta\mu,\mathcal{S}} = A'' + JB'' - C'' + JD''. \tag{A.16}$$

For the SU(2) broken situation at half filling we find[3]

$$
\mathcal{Q}\chi_h\mathcal{Q}^T = \begin{pmatrix} Q\chi_{c,h}Q^T & Q\chi_{cs,h}Q^T \\ Q\chi_{sc,h}Q^T & Q\chi_{s,h}Q^T \end{pmatrix}
$$
$$
= \begin{pmatrix} Q\mathrm{Re}(\chi_{\uparrow\uparrow,\delta\mu} - J\chi_{\uparrow\downarrow,\delta\mu})Q^T & iQ\mathrm{Im}(\chi_{\uparrow\uparrow,\delta\mu} - J\chi_{\uparrow\downarrow,\delta\mu})Q^T \\ iQ\mathrm{Im}(\chi_{\uparrow\uparrow,\delta\mu} + J\chi_{\uparrow\downarrow,\delta\mu})Q^T & Q\mathrm{Re}(\chi_{\uparrow\uparrow,\delta\mu} + J\chi_{\uparrow\downarrow,\delta\mu})Q^T \end{pmatrix}
$$
$$
= \begin{pmatrix} \chi'_{c,\delta\mu,\mathcal{A}} & \mathbb{0} & \mathbb{0} & i\,\chi''_{c,\delta\mu,\mathcal{S}} \\ \mathbb{0} & \chi'_{s,\delta\mu,\mathcal{S}} & i\,\chi''_{s,\delta\mu,\mathcal{A}} & \mathbb{0} \\ \mathbb{0} & i\,\chi''_{s,\delta\mu,\mathcal{S}} & \chi'_{s,\delta\mu,\mathcal{A}} & \mathbb{0} \\ i\,\chi''_{c,\delta\mu,\mathcal{A}} & \mathbb{0} & \mathbb{0} & \chi'_{c,\delta\mu,\mathcal{S}} \end{pmatrix}, \tag{A.17}
$$

which has clearly the same matrix components as $\mathcal{Q}\chi_{\delta\mu}\mathcal{Q}^T$ but with the 2$^{\mathrm{nd}}$ and 4$^{\mathrm{th}}$ column and row exchanged. Therefore, a corresponding reordering of Eq. (A.17), which corresponds to a matrix transformation with T of Eq. (4.14), leads to the matrix in Eq. (A.15). This proves

$$\mathcal{Q}\chi_h\mathcal{Q}^T = T\mathcal{Q}\chi_{\delta\mu}\mathcal{Q}^T T. \tag{A.18}$$

The final step is to compare the eigenvalues and eigenvectors of $\chi_{\delta\mu}$ and χ_h. Since the two matrices just differ by the orthogonal transformation $T\mathcal{Q}$ the eigenvalues of both matrices are the same and for each eigenvector v of $\chi_{\delta\mu}$, $T\mathcal{Q}v$ is an eigenvector of χ_h. Due to the block diagonal form of $\chi_{\delta\mu}$, all eigenvectors have either entries in the first two subspaces (the charge subspace) or in the last two subspaces (the spin subspace). If we now transform an eigenvector from the charge/spin subspace $v_{c/s}$ of $\chi_{\delta\mu}$ we find

$$
T\mathcal{Q}v_c = T\mathcal{Q}\left[\begin{pmatrix} v_{\mathcal{S}} \\ Jv_{\mathcal{S}} \\ \mathbb{0} \\ \mathbb{0} \end{pmatrix} + \begin{pmatrix} v_{\mathcal{A}} \\ -Jv_{\mathcal{A}} \\ \mathbb{0} \\ \mathbb{0} \end{pmatrix}\right] = \begin{pmatrix} \mathbb{0} \\ \mathbb{0} \\ v_{\mathcal{S}} \\ Jv_{\mathcal{S}} \end{pmatrix} + \begin{pmatrix} v_{\mathcal{A}} \\ -Jv_{\mathcal{A}} \\ \mathbb{0} \\ \mathbb{0} \end{pmatrix} \tag{A.19}
$$

---

[3]Note that $J\chi_{\uparrow\downarrow,\delta\mu} = \begin{pmatrix} \mathbb{0} & J \\ J & \mathbb{0} \end{pmatrix}\left(\begin{pmatrix} C' & JD'J \\ D' & JC'J \end{pmatrix} + i\begin{pmatrix} C'' & -JD''J \\ D'' & -JC''J \end{pmatrix}\right)$

and

$$
T\mathcal{Q}v_{\mathrm{s}} = T\mathcal{Q}\left[\begin{pmatrix} \mathbb{0} \\ \mathbb{0} \\ v_{\mathcal{S}} \\ Jv_{\mathcal{S}} \end{pmatrix} + \begin{pmatrix} \mathbb{0} \\ \mathbb{0} \\ v_{\mathcal{A}} \\ -Jv_{\mathcal{A}} \end{pmatrix}\right] = \begin{pmatrix} v_{\mathcal{S}} \\ Jv_{\mathcal{S}} \\ \mathbb{0} \\ \mathbb{0} \end{pmatrix} + \begin{pmatrix} \mathbb{0} \\ \mathbb{0} \\ v_{\mathcal{A}} \\ -Jv_{\mathcal{A}} \end{pmatrix}, \tag{A.20}
$$

where we clearly see an invariance of the antisymmetric part and a mapping from charge to spin subspace (or vice versa) for the symmetric part.

Now the final step is the mapping of the pairing susceptibility from out of half filling without magnetic field

$$
\chi_{\mathrm{pair},\delta\mu}^{\nu\nu'\omega} = \chi_{\uparrow\downarrow,\mathrm{pp},\delta\mu}^{\nu,\omega-\nu',\omega} - \chi_{0,\mathrm{pp}}^{\nu\nu'\omega} \tag{A.21}
$$

to the transverse spin channel at half filling with magnetic field [46]

$$
\chi_{S_x,h}^{\nu\nu'\omega} = \chi_{S_y,h}^{\nu\nu'\omega} = \frac{1}{2}(\chi_{\overline{\uparrow\downarrow},h} + \chi_{\overline{\downarrow\uparrow},h}). \tag{A.22}
$$

From Eq. (2.27) it is obvious that $\chi_{\overline{\uparrow\downarrow}} = G_{2,\overline{\uparrow\downarrow}}$ and $\chi_{\overline{\downarrow\uparrow}} = G_{2,\overline{\downarrow\uparrow}}$, if there is spin conservation. Then using the definition

$$
G_{2,\overline{\sigma\sigma'}} = \int_0^\beta d\tau_1 d\tau_2 d\tau_3 d\tau_4\, e^{-i\nu_1\tau_1} e^{i\nu_2\tau_2} e^{-i\nu_3\tau_3} e^{i\nu_4\tau_4} \langle T_\tau c_\sigma^\dagger(\tau_1) c_{\sigma'}(\tau_2) c_{\sigma'}^\dagger(\tau_3) c_\sigma(\tau_4) \rangle \tag{A.23}
$$

and making a Shiba transformation we obtain

$$
G_{2,\overline{\uparrow\downarrow},h}(\nu_1,\nu_2,\nu_3,\nu_4) = -G_{2,\overline{\uparrow\downarrow},\delta\mu}(\nu_1,-\nu_3,-\nu_2,\nu_4) \quad \text{and} \tag{A.24}
$$

$$
G_{2,\overline{\downarrow\uparrow},h}(\nu_1,\nu_2,\nu_3,\nu_4) = -G_{2,\overline{\downarrow\uparrow},\delta\mu}(-\nu_4,\nu_2,\nu_3,-\nu_1). \tag{A.25}
$$

By using the crossing symmetry, we can obtain [26]

$$
\chi_{\sigma\sigma'}(\nu_1,\nu_4,\nu_3,\nu_2) - \chi_{0,\overline{\sigma\sigma'}}(\nu_1,\nu_2,\nu_3,\nu_4) = -\chi_{\overline{\sigma\sigma'}}(\nu_1,\nu_2,\nu_3,\nu_4) + \chi_{0,\sigma\sigma'}(\nu_1,\nu_4,\nu_3,\nu_2)\delta_{\sigma\sigma'} \tag{A.26}
$$

and get

$$
\chi_{\overline{\uparrow\downarrow},h}(\nu_1,\nu_2,\nu_3,\nu_4) = \chi_{\uparrow\downarrow,\delta\mu}(\nu_1,\nu_4,-\nu_2,-\nu_3) - \chi_{0,\overline{\uparrow\downarrow},\delta\mu}(\nu_1,-\nu_3,-\nu_2,\nu_4) \quad \text{and} \tag{A.27}
$$

$$
\chi_{\overline{\downarrow\uparrow},h}(\nu_1,\nu_2,\nu_3,\nu_4) = \chi_{\downarrow\uparrow,\delta\mu}(-\nu_4,-\nu_1,\nu_3,\nu_2) - \chi_{0,\overline{\downarrow\uparrow},\delta\mu}(-\nu_4,\nu_2,\nu_3,-\nu_1). \tag{A.28}
$$

Now introducing the ph-frequency convention of Eq. (2.30a) and shifting $\omega \to \omega - \nu - \nu'$ according to Eq. (2.33) on the right-hand side of the equations to switch to the pp-notation, we end up with

89

$$\chi_{\uparrow\downarrow,h}^{\nu\nu'\omega} = \chi_{\uparrow\downarrow,\mathrm{pp},\delta\mu}^{\nu,-\nu'-\omega,-\omega} - \chi_{0,\overline{\uparrow\downarrow},\mathrm{pp},\delta\mu}^{\nu,\nu',-\omega} \quad \text{and} \tag{A.29}$$

$$\chi_{\downarrow\uparrow,h}^{\nu\nu'\omega} = \chi_{\downarrow\uparrow,\mathrm{pp},\delta\mu}^{-\nu',\nu+\omega,\omega} - \chi_{0,\overline{\downarrow\uparrow},\mathrm{pp},\delta\mu}^{-\nu',-\nu,\omega} \overset{\text{TR Eq. (2.36)}}{=} \chi_{\uparrow\downarrow,\mathrm{pp},\delta\mu}^{\nu+\omega,-\nu',\omega} - \chi_{0,\overline{\uparrow\downarrow},\mathrm{pp},\delta\mu}^{-\nu,-\nu',\omega}. \tag{A.30}$$

Calculating χ_{S_x} gives

$$\chi_{S_x,h}^{\nu\nu'\omega} = \frac{1}{2} \left(\chi_{\uparrow\downarrow,\mathrm{pp},\delta\mu}^{\nu,-\nu'-\omega,-\omega} + \chi_{\uparrow\downarrow,\mathrm{pp},\delta\mu}^{\nu+\omega,-\nu',\omega} - \chi_{0,\overline{\uparrow\downarrow},\mathrm{pp},\delta\mu}^{\nu,\nu',-\omega} - \chi_{0,\overline{\uparrow\downarrow},\mathrm{pp},\delta\mu}^{\nu+\omega,\nu'+\omega,\omega} \right), \tag{A.31}$$

by using crossing symmetry Eq. (2.34) and SU(2)-symmetry Eq. (2.37) for $\chi_{0,\overline{\uparrow\downarrow},\mathrm{pp},\delta\mu}^{-\nu,-\nu',\omega}$. For $\omega = 0$ Eq. (4.16) is proven.

A.3 Corresponding eigenvectors of divergence lines

In this section additional analysis of the eigenvectors of the corresponding divergences in section 4.2 are presented.

We start by showing the eigenvectors of the second loop structure of the repulsive sector in Figs. A.1 to A.3
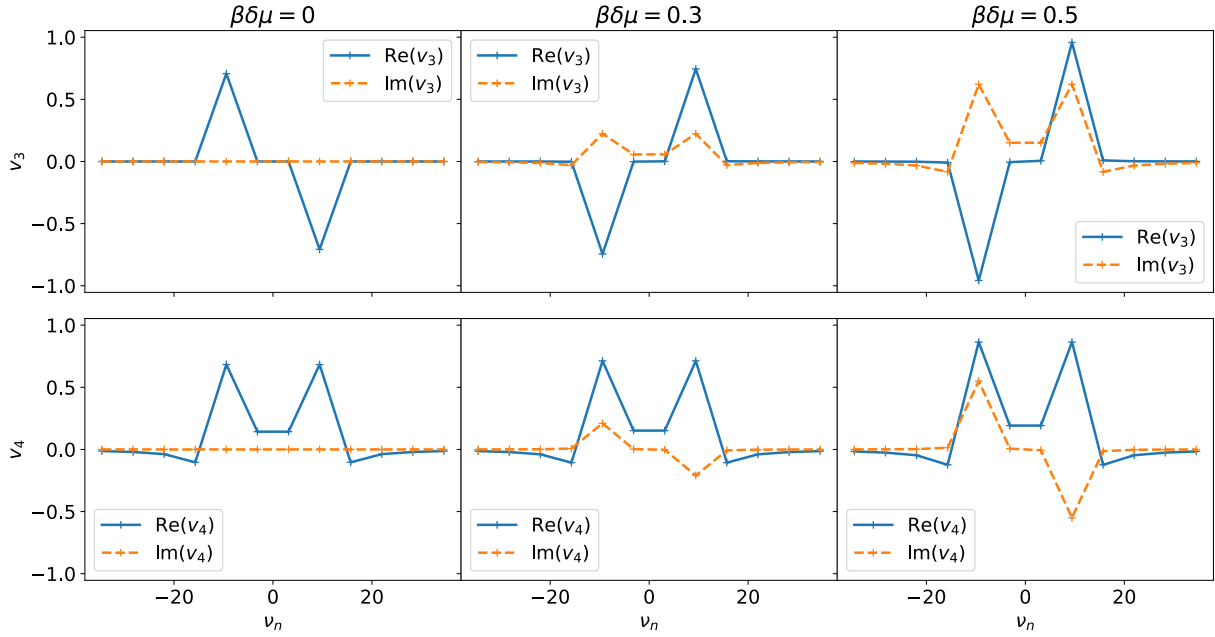
Figure A.1: Upper row: Eigenvectors along the second antisymmetric divergence v_3. Lower row: Eigenvectors along the second symmetric divergence v_4. Both for different $\beta\delta\mu$. Vectors are normalized with $\|.\|_T$.

90
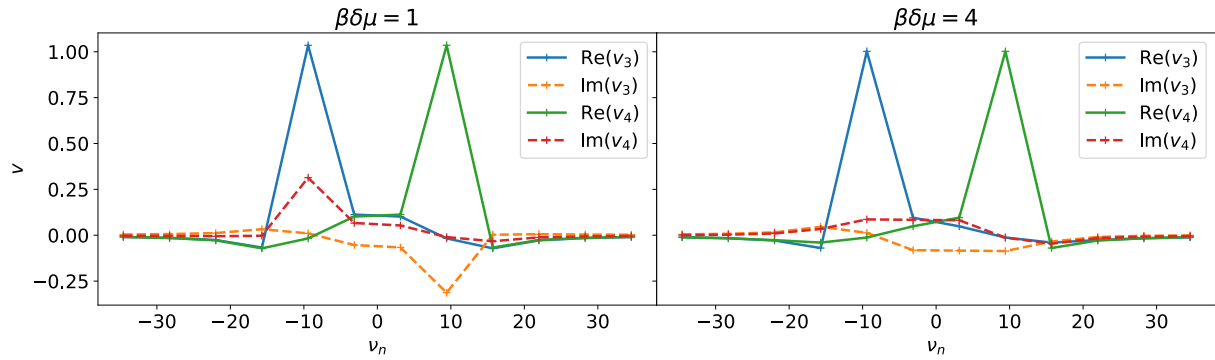
Figure A.2: Eigenvectors along the second pseudo-divergence in the charge channel for different $\beta\delta\mu$. Vectors are normalized with $\|.\|_T$.
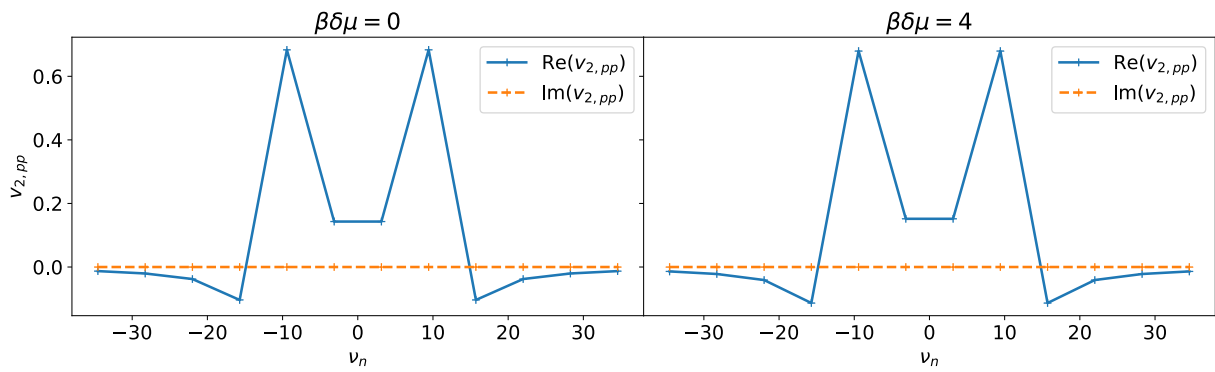
Figure A.3: Eigenvector of the second divergence in the pairing channel for different $\beta\delta\mu$. Vectors are normalized with $\|.\|_T$.

One clearly sees that the vectors of the second loop structure are approximately localized at ν_2 and $-\nu_2$.

In Fig. A.4 the development of the eigenvalues, that lead to the first symmetric and antisymmetric divergence in the charge channel (attractive sector), along a path with constant $\beta\delta\mu = 1.5$ are shown.
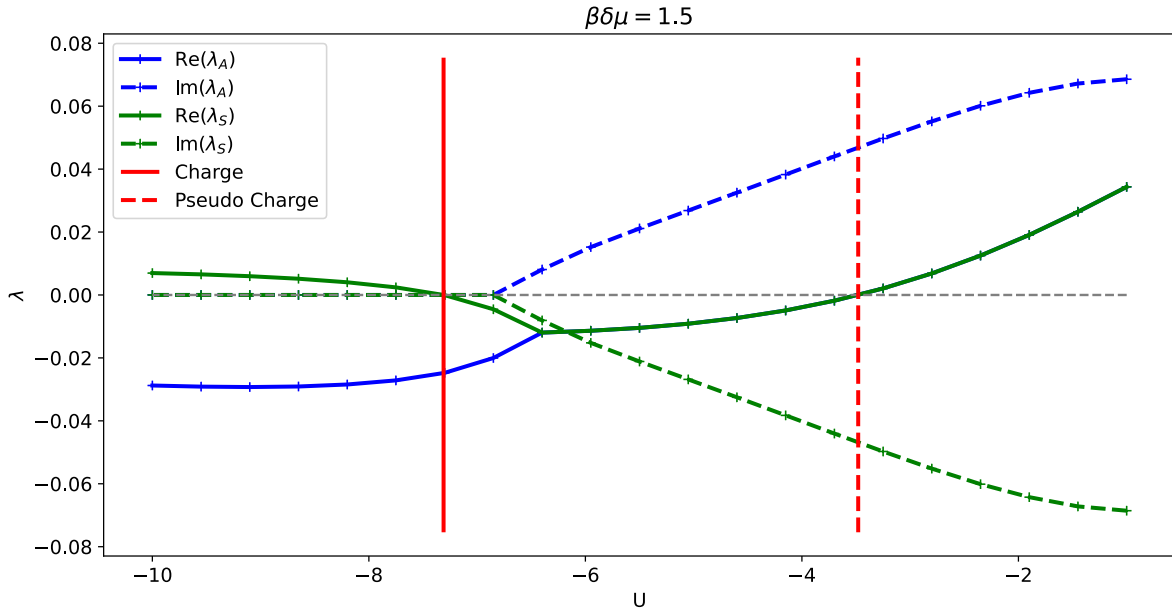
Figure A.4: Development of the eigenvalues, that lead to the first symmetric λ_S and antisymmetric λ_A divergence in the charge channel (attractive sector), along a path with constant $\beta\delta\mu = 1.5$. The red dashed lines mark the first pseudo-divergence and the red solid line marks the symmetric divergence of the first parabola.

We see that, coming from larger U values, the real part of the complex conjugate pair changes from positive to negative at the pseudo-divergence. In the following, the complex pair becomes two distinct real eigenvalues after an exceptional point. The eigenvalue that corresponds to the symmetric eigenvector λ_S becomes positive by crossing the symmetric divergence while the antisymmetric eigenvalue λ_A stays negative.

In Fig. A.5 we plot the development of the eigenvectors along the first symmetric divergence in the charge channel of the repulsive sector ($U > 0$).
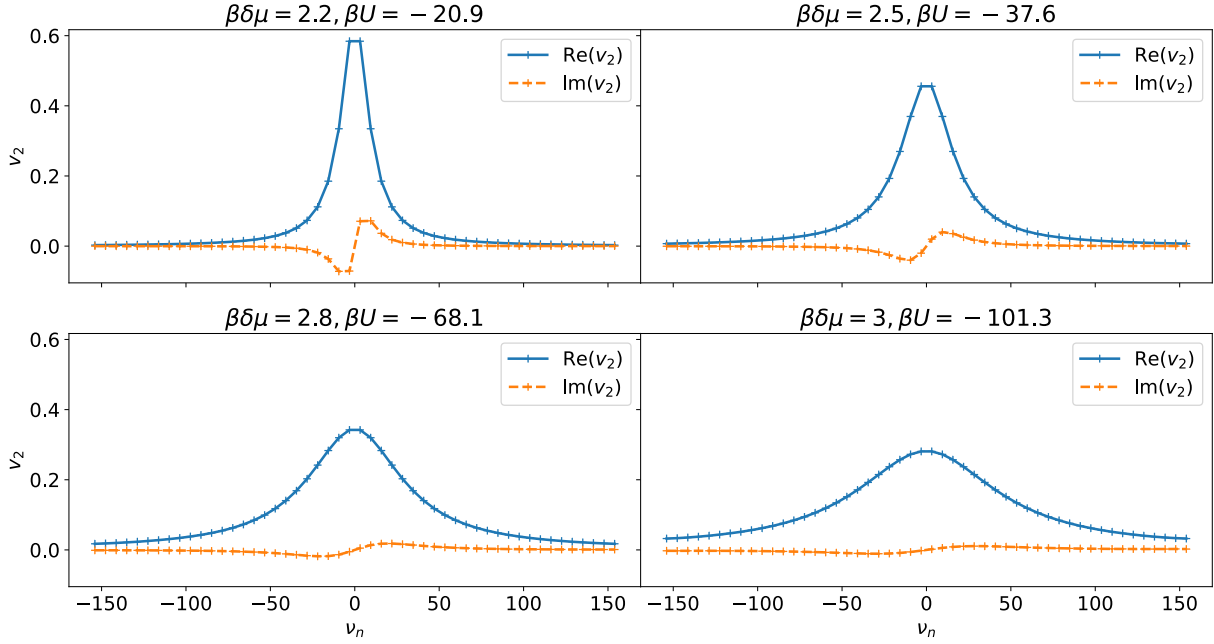
Figure A.5: Delocalization of the eigenvector along the first parabola in the charge channel. Vectors are normalized with $\|.\|_T$.

We find that the eigenvector gets more and more delocalized in Matsubara frequencies for more negative values of βU ($U < 0$).

This delocalized eigenvector corresponds to the largest eigenvalue in the generalized susceptibility. As it was found in Ref. [11] this eigenvalue dominates the behavior of the physical susceptibility and gives rise to a Curie behavior ($\chi_{\text{phys}} \propto \beta$). Therefore, the eigenvalue must scale like β, diverging in the limit $T \to 0$, and the eigenvector must correspond to a weight which does not get suppressed. Both conditions are naturally realized by a delocalized symmetric eigenvector. In fact, this behavior can be generated by an eigenvector that becomes more and more delocalized for $T \to 0$ as we observe in Fig. A.5. For instance, let's consider a matrix where every coefficient is equal to 1, namely the all-ones matrix. The argument can be understood by considering a matrix where every coefficient is equal to 1, namely the all-ones matrix. This provides a way to generate a divergent eigenvalue without any divergent matrix element. If we consider an all-ones matrix of the shape $n \times n$, this matrix has a single nonzero eigenvalue with the value n and $n-1$ eigenvalues which are equal to 0. The eigenvector of the eigenvalue n is equal to 1 for every component. In the context of generalized susceptibilities the dimension of the matrix, that needs to be considered, scales with β as more and more Matsubara frequencies will be included if the cut-off-frequency is kept constant by reducing the temperature. In this case, the eigenvalue of the delocalized eigenvalue naturally scales proportionally to β.

Numerically, we observe that the delocalized eigenvector gives rise to a slow decaying frequency structure in the generalized susceptibility, as it can be seen in Fig. A.6 in the spin channel for $U > 0$ and in the charge channel for $U < 0$. This structure approaches the all-ones matrix for the $T \to 0$ limit.
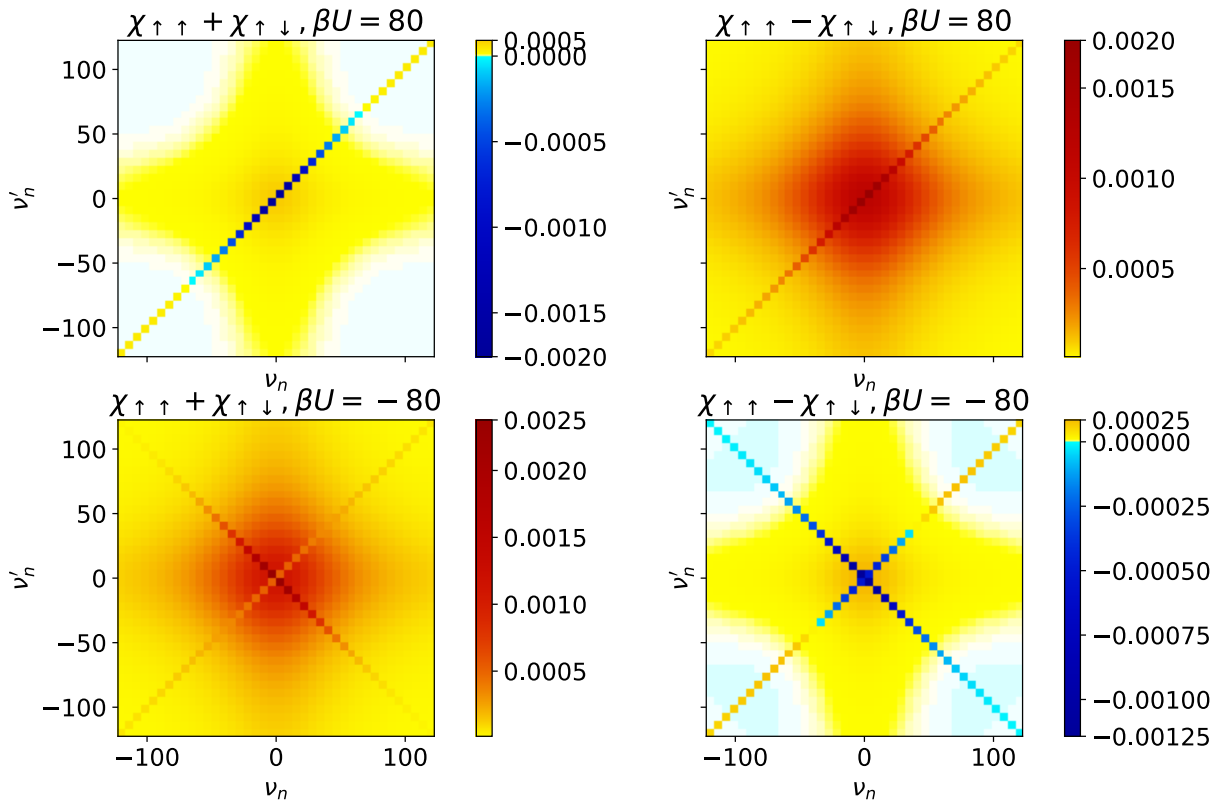
Figure A.6: Generalized susceptibilities for positive and negative interaction U. As matrices in the fermionic frequency space ν, ν'

The delocalization in ν_n of the eigenvector of the first symmetric divergence in the charge channel at $U < 0$ has not been found in any other eigenvectors of the charge channel (see Fig. A.7 for an exemplary competition)
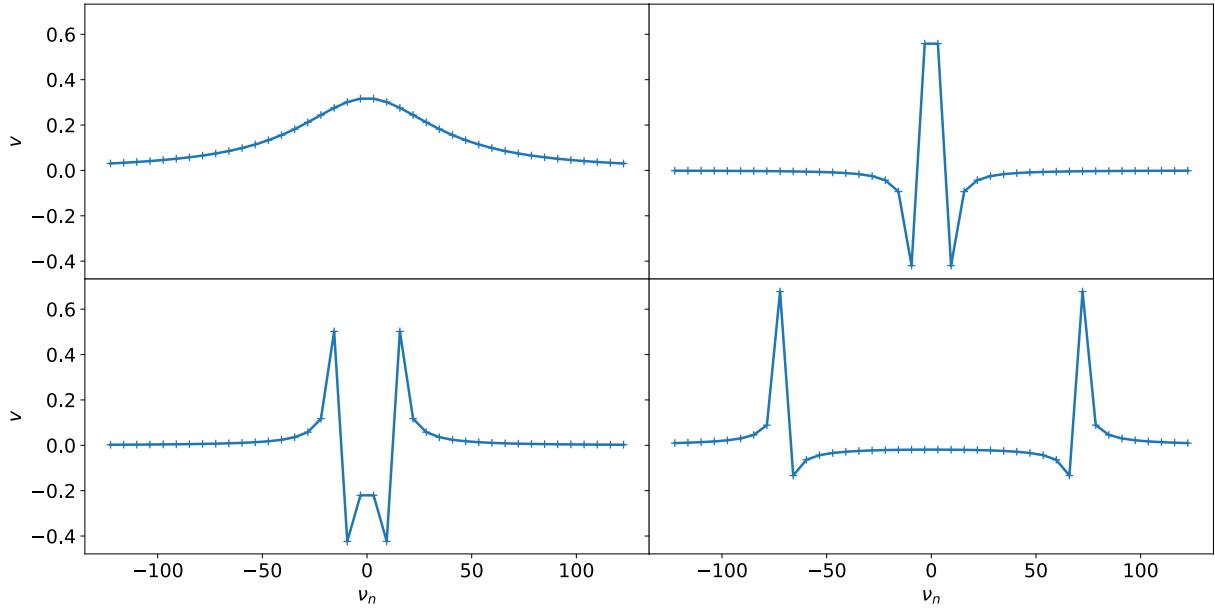
Figure A.7: Different symmetric eigenvectors of the generalized charge susceptibility for $\beta U = -80$ at $\mu = U/2$.

A.4 Generalized susceptibilities for T=0

In this section the $T \to 0$ limit of the generalized charge and spin susceptibility is calculated. Thereby, the susceptibility $\chi_{c/s}(\nu, \nu', \omega)$ at $T = 0$ can no longer be viewed as a matrix, as the Matsubara frequencies become continuous. Mathematically $\chi_{c/s}(\nu, \nu', \omega)$ can be regarded as an operator represented in Matsubara frequency space[4]. Consequently, all sums over Matsubara frequencies become integrals and a Kronecker-Delta of Matsubara frequencies becomes a Dirac-Delta:

$$\frac{1}{\beta} \sum_{\nu} \xrightarrow{\beta \to \infty} \int_{-\infty}^{\infty} \frac{d\nu}{2\pi}, \tag{A.32}$$

$$\beta \delta_{\nu\nu'} \xrightarrow{\beta \to \infty} 2\pi \delta(\nu - \nu'), \tag{A.33}$$

$$\beta \delta_{\omega 0} \xrightarrow{\beta \to \infty} 2\pi \delta(\omega). \tag{A.34}$$

For the remaining terms that depend on β in Eq. (A.7) the limit $\beta \to \infty$ is done for $U > 0$ in Eqs. (A.35) to (A.38)

---

[4]Note that also the susceptibilities at finite T can be regarded as operators in this sense, but we will stick to the terminology of infinite dimensional matrices as they still have discrete indices.

$$n = \frac{1 + e^{\beta(\mu-U)}}{2 + e^{-\beta\mu} + e^{\beta(\mu-U)}} \xrightarrow{\beta\to\infty} \begin{cases} 0, & \text{if } \mu < 0 \\ \frac{1}{3}, & \text{if } \mu = 0 \\ \frac{1}{2}, & \text{if } 0 < \mu < U \\ \frac{2}{3}, & \text{if } \mu = U \\ 1, & \text{if } \mu > U \end{cases} \tag{A.35}$$

$$q_0 = \frac{2n-1}{i\nu + i\nu' + 2\mu - U} \xrightarrow{\beta\to\infty} \begin{cases} 0, & \forall \nu, \nu' \text{ if } \mu \to U/2 \\ \frac{2n-1}{i\nu+i\nu'+2\mu-U}, & \text{else} \end{cases}, \tag{A.36}$$

$$q_1 = -\frac{1}{2 + e^{-\beta\mu} + e^{\beta(\mu-U)}} \xrightarrow{\beta\to\infty} \begin{cases} 0, & \text{if } \mu < 0 \\ -\frac{1}{3}, & \text{if } \mu = 0 \\ -\frac{1}{2}, & \text{if } 0 < \mu < U \\ -\frac{2}{3}, & \text{if } \mu = U \\ 0, & \text{if } \mu > U \end{cases} \tag{A.37}$$

$$q_2 = \frac{e^{-\beta U} - 1}{(2 + e^{-\beta\mu} + e^{\beta(\mu-U)})^2} \xrightarrow{\beta\to\infty} \begin{cases} 0, & \text{if } \mu < 0 \\ -\frac{1}{9}, & \text{if } \mu = 0 \\ -\frac{1}{4}, & \text{if } 0 < \mu < U \\ -\frac{1}{9}, & \text{if } \mu = U \\ 0, & \text{if } \mu > U \end{cases} \tag{A.38}$$

where the limit of q_0 is done according to Eq. (A.8).

The corresponding terms for $U < 0$ and $\beta \to \infty$ are calculated in Eqs. (A.39) to (A.42)

$$n = \frac{1 + e^{\beta(\mu-U)}}{2 + e^{-\beta\mu} + e^{\beta(\mu-U)}} \xrightarrow{\beta\to\infty} \begin{cases} 0, & \text{if } \mu < U/2 \\ \frac{1}{2}, & \text{if } \mu = U/2 \\ 1, & \text{if } \mu > U/2 \end{cases} \tag{A.39}$$

$$q_0 = \frac{2n-1}{i\nu + i\nu' + 2\mu - U} \xrightarrow{\beta\to\infty} \begin{cases} \pi\delta(\nu + \nu'), & \text{if } \mu \to U/2 \\ \frac{2n-1}{i\nu+i\nu'+2\mu-U}, & \text{else} \end{cases}, \tag{A.40}$$

96

$$q_1 = -\frac{1}{2 + e^{-\beta\mu} + e^{\beta(\mu-U)}} \xrightarrow{\beta\to\infty} = 0\,\forall\mu, \tag{A.41}$$

$$q_2 = \frac{e^{-\beta U} - 1}{(2 + e^{-\beta\mu} + e^{\beta(\mu-U)})^2} \xrightarrow{\beta\to\infty} \begin{cases} \frac{1}{4}, & \text{if } \mu = U/2 \\ 0, & \text{else} \end{cases}. \tag{A.42}$$

Having performed all limits in Eq. (A.7) we can now construct the generalized susceptibilities in charge and spin channel for $T = 0$. However, for the numeric calculations, the susceptibilities need to be discretized again. How this is done is stated in Eqs. (A.43) to (A.45)

$$2\pi\delta(\nu - \nu') \xrightarrow{\text{discretization}} \frac{2\pi}{\Delta\nu}\delta_{\nu\nu'}, \tag{A.43}$$

$$2\pi\delta(\omega) \xrightarrow{\text{discretization}} \frac{2\pi}{\Delta\omega}\delta_{\omega 0}, \tag{A.44}$$

$$\int \frac{d\nu}{2\pi} \xrightarrow{\text{discretization}} \frac{\Delta\nu}{2\pi}\sum_\nu, \tag{A.45}$$

where $\Delta\nu$ and $\Delta\omega$ refer to the equidistant frequency grid that is chosen.

The in this way discretization quantities again represent matrices in fermionic Matsubara frequency space (for constant bosonic frequency) with a cut-off frequency $\nu_{\max}$. Evidently, $\nu_{\max}$ and $\Delta\nu$ must be large respectively small enough such that the results do not depend on them.

Finally, the eigenequation of the generalized susceptibilities in its continuous form is

$$\int_{-\infty}^{\infty} \frac{d\nu'}{2\pi}\chi(\nu,\nu')v(\nu') = \lambda v(\nu), \tag{A.46}$$

with the eigenvector $v(\nu)$ and the eigenvalue λ. According to Eq. (A.45) the discretized form is

$$\frac{\Delta\nu}{2\pi}\sum_{\nu'} \frac{d\nu'}{2\pi}\chi^{\nu,\nu'}v(\nu') = \lambda v(\nu). \tag{A.47}$$

Note, that for a numerical diagonalization routine (e.g. *numpy.linalg.eig*) the factor $\frac{\Delta\nu}{2\pi}$ is in general missing. Therefore, to scale correctly every eigenvalue obtained with the help of a numerical routine, the factor $\frac{\Delta\nu}{2\pi}$ of the discretization procedure must be included.

A.5 Random phase approximation for T=0

In this section the random phase approximation (RPA) for $T = 0$ is derived. Thereby, we explicitly separate the singular (proportional to the Dirac-Delta distribution) terms from the regular terms. We start from the Feynman diagrammatic definition of the RPA:

$$
\begin{aligned}
\chi_{\mathrm{RPA}}(\nu,\nu') = \quad & - \;\; \text{⬡} \;\; - \;\; \text{⬡⬡} \;\; - \;\; \text{⬡⬡⬡} \;\; - \; ... \\
=\,& \chi_0(\nu,\nu') - \int \frac{d\nu_1}{2\pi}\frac{d\nu_2}{2\pi} \, \chi_0(\nu,\nu_1)\Gamma(\nu_1,\nu_2)\chi_0(\nu_2,\nu') \\
& + \int \frac{d\nu_1}{2\pi}\frac{d\nu_2}{2\pi}\frac{d\nu_3}{2\pi}\frac{d\nu_4}{2\pi} \, \chi_0(\nu,\nu_1)\Gamma(\nu_1,\nu_2)\chi_0(\nu_2,\nu_3)\Gamma(\nu_3,\nu_4)\chi_0(\nu_4,\nu') - ... \\
=\,& - G^2(\nu)2\pi\delta(\nu-\nu') - G^2(\nu)UG^2(\nu') \sum_{n=0}^{\infty}\left(\int \frac{d\tilde\nu}{2\pi}UG^2(\tilde\nu)\right)^n ,
\end{aligned} \tag{A.48}
$$

where

$$
\chi_0(\nu,\nu') = \quad - \;\; \text{⬡} \;\; = -G^2(\nu)2\pi\delta(\nu-\nu'), \tag{A.49}
$$

$$
\Gamma(\nu,\nu') = \quad \text{✕} \;\; = U \tag{A.50}
$$

and all lines in the diagrams are full Green's functions. The RPA can also be derived from a Luttinger-Ward functional, where the skeleton series only contains a first order term in U. The Luttinger-Ward functional and the from it derived self energy and irreducible vertex are shown in Eqs. (A.51) to (A.53)

$$
\Phi = \quad \text{⦾} , \tag{A.51}
$$

$$
\Sigma = \frac{\delta\Phi}{\delta G} = \quad \text{⟶⦾⟶} \;\; = nU, \tag{A.52}
$$

$$
\Gamma = \frac{\delta^2\Phi}{\delta G^2} = \quad \text{✕} . \tag{A.53}
$$

Therefore, the full Green's function of the RPA reads

$$
G(\nu) = \frac{1}{i\nu^2 + \mu - nU}. \tag{A.54}
$$

With $G(\nu)$ we can further simplify the RPA expression. By defining a χ_0^{Phys}

$$\chi_0^{\text{Phys}} := -\int \frac{d\tilde{\nu}}{2\pi} U G^2(\tilde{\nu}) = -\int \frac{d\tilde{\nu}}{2\pi} \frac{U}{(i\nu^2 + \mu - nU)^2} = \begin{cases} \infty, & \text{if } \mu = nU \\ 0, & \text{otherwise} \end{cases} \tag{A.55}$$

and evaluating the geometric series $\sum_{n=0}^{\infty}(-\chi_0^{\text{Phys}})^n$ in Eq. (A.48) we end up with our final expression for the RPA

$$\chi_{\text{RPA}} = -G^2(\nu)2\pi\delta(\nu - \nu') - G^2(\nu)U G^2(\nu')(1 - \delta_{\mu,nU}). \tag{A.56}$$

Hereby, we ignore that the geometric series does not converge for $\mu = nU$, where χ_0^{Phys} diverges, and take the evaluation of the geometric series, as it is usually done in Feynman diagrammatic methods. We proceed and keep in mind that the RPA is in principle not valid for this case.

For the theory to be consistent, the filling n must be self-consistently determined. The self-consistent equation that defines n is given by

$$n = \frac{1}{\beta} \sum_{\nu_n} G(\nu_n) e^{-i\nu_n 0^-} = \frac{1}{e^{\beta(nU-\mu)} + 1} \xrightarrow{\beta \to \infty} \Theta(-nU + \mu), \tag{A.57}$$

where Θ is the Heaviside step function.

For $T = 0$ the self-consistent equation cannot be fulfilled for all regions in the phase space. The problematic parameter regime is a V-shaped region for both repulsive and attractive interaction, this V-shaped region is defined by $0 < \mu < U$ for $U > 0$ and $U < \mu < 0$ for $U < 0$. For $U > 0$ and $0 < \mu < U$ the self-consistent Eq. (A.57) has no solution except for the ph-symmetric case $\mu = U/2$ where $n = 1/2$. Moreover, Eq. (A.57) has two concurrent solutions for $U < 0$ and $U < \mu < 0$ which are $n = 0$ and $n = 1$, except for $\mu = U/2$ where $n = 1/2$ uniquely.

For all other regions, Eq. (A.57) has a unique solution that coincides with the exact solution of n in Eqs. (A.35), (A.39). Because of these difficulties with the self-consistent determination of n we use the exact filling as an input for the RPA calculations in section 4.3.

In Fig. 4.17 we see that the eigenvalue, that is not part of the continuous spectra for $U/2 < \mu < 0$ and $U < 0$, is not reproduced by our RPA calculations. Although, in principle, eigenvalues that are not part of the continuous spectrum would be possible and can also be generated within a RPA expression. For example, by setting n to the not justified value $1/2$, we find a spectrum that has a similar shape than the spectra of the exact generalized susceptibility with the disconnected eigenvalue included. However, the non-perturbative structure of the spectra (which is a crossing in the spectra structure cf. Fig. 4.10) is not captured by RPA, independently of the choice of n.

A.6 Convergence problem of the iterative scheme

In this section, we investigate the convergence problems due to strong oscillations of our iterative scheme Eq. (5.1) in more detail. We identified the problematic region at the U values between the (non-perturbative) pseudo-divergence in the charge channel and the pairing divergence for $0.6 < |\beta\delta\mu| < 1.75$, where the charge pseudo-divergence is located at smaller U values than the pairing divergence. We exemplarily show data for $\beta\delta\mu = 1$ in the following. We start by presenting data that are calculated with the iterative scheme where the mixing of different iterations (see section 5.1) are used in Figs. A.8, A.9.
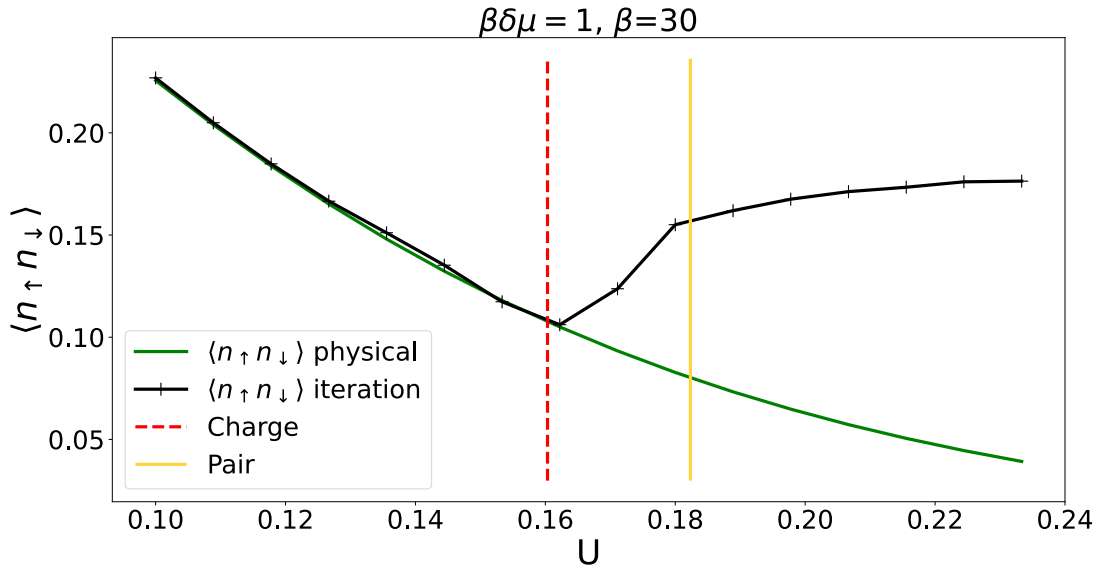
Figure A.8: Double occupancy of the physical solution and the iteratively obtained solution plotted for different U values at $\beta\delta\mu = 1$. In the calculation the mixing of different iterations has been used. The red dashed vertical line marks the U value of the first non-perturbative pseudo-divergence in the charge channel, while the solid yellow vertical line marks the U values of the first divergence in the pairing channel.

In Fig. A.8 we see a clear change in the slope of double occupancy versus U once we enter the problematic parameter region between the charge pseudo-divergence and the pairing divergence. For a more detailed investigation, we look again at $G_0(\nu_1)$ and $\Sigma(\nu_1)$.
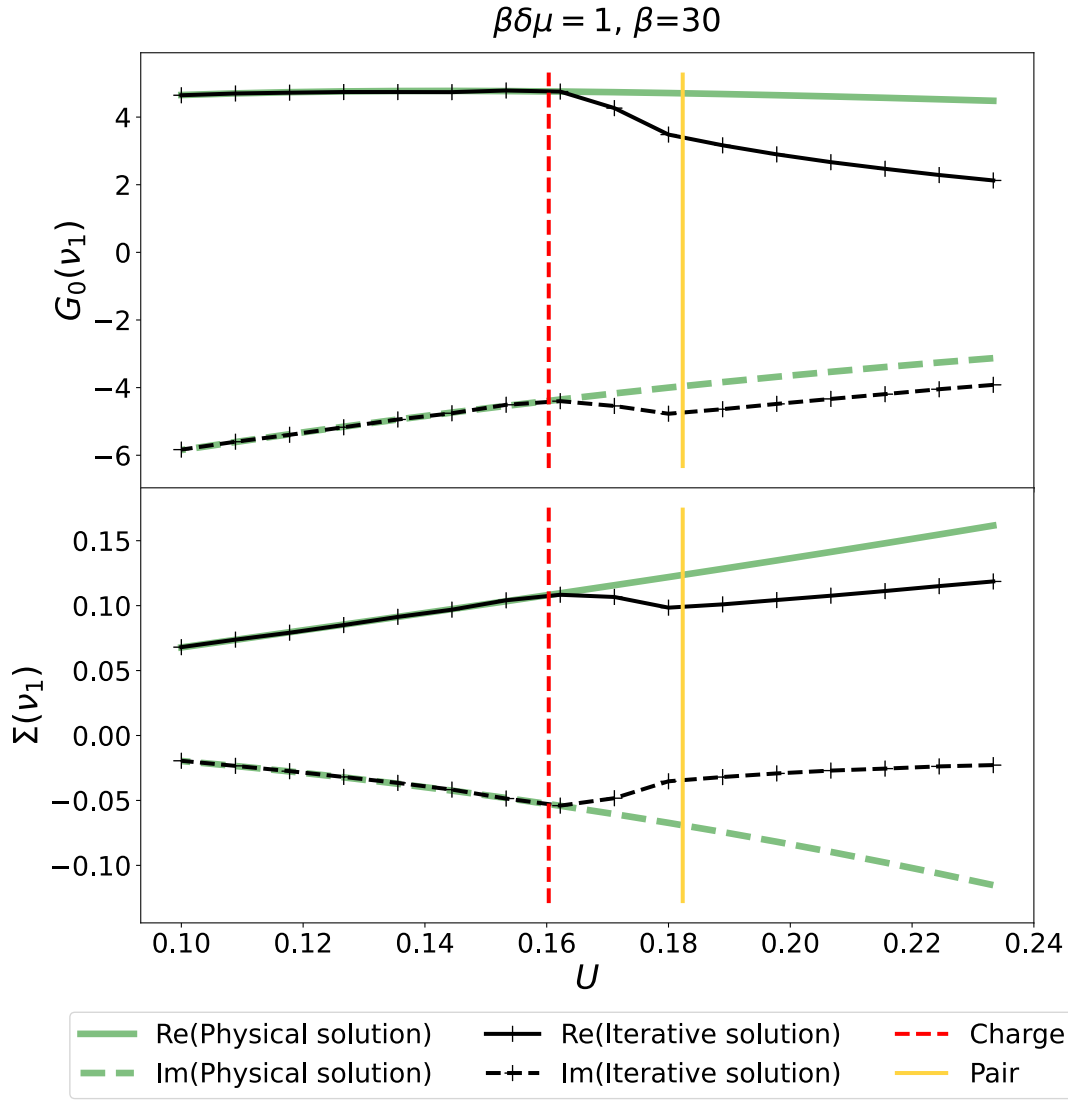
Figure A.9: **Upper:** The physical and the iteratively obtained $G_0(\nu_1)$ of the HA plotted for different U values. **Lower:** The physical and the iteratively obtained $\Sigma(\nu_1)$ plotted for different U values at $\delta\mu = 1$ and $\beta = 30$. In the calculation the mixing of different iterations has been used. The dashed red vertical line marks the U value of the first non-perturbative pseudo-divergence in the charge channel, while the solid yellow vertical line marks the U values of the first divergence in the pairing channel.

The data in Fig. A.9 suggests a completely continuous branch switch between the physical and the unphysical solution at the charge pseudo-divergence. As this contradicts the exact derivation provided in Ref. [12] and our numerical results are strongly dependent on the mixing procedure, we conclude that these data can not be trusted. In fact, we suspect that the mixing procedure in presence of huge oscillations might lead to a Maxwell-construction-like interpolation between the physical and the unphysical solution.

In this context, we also investigate the influence of the mixing procedure on the solution we get from our iterative scheme. To this aim, we run the iterative scheme with mixing (if some oscillations are detected) for a single parameter point until it converges, and after the convergence

we perform 100 additional iterations without mixing to check whether a stable solution with the mixing procedure was obtained.

The results of this procedure are shown for $\beta\delta\mu = 1$ for a U value between the pseudo-divergence and the pairing divergence and a U value after the pairing divergence in Fig. A.10.
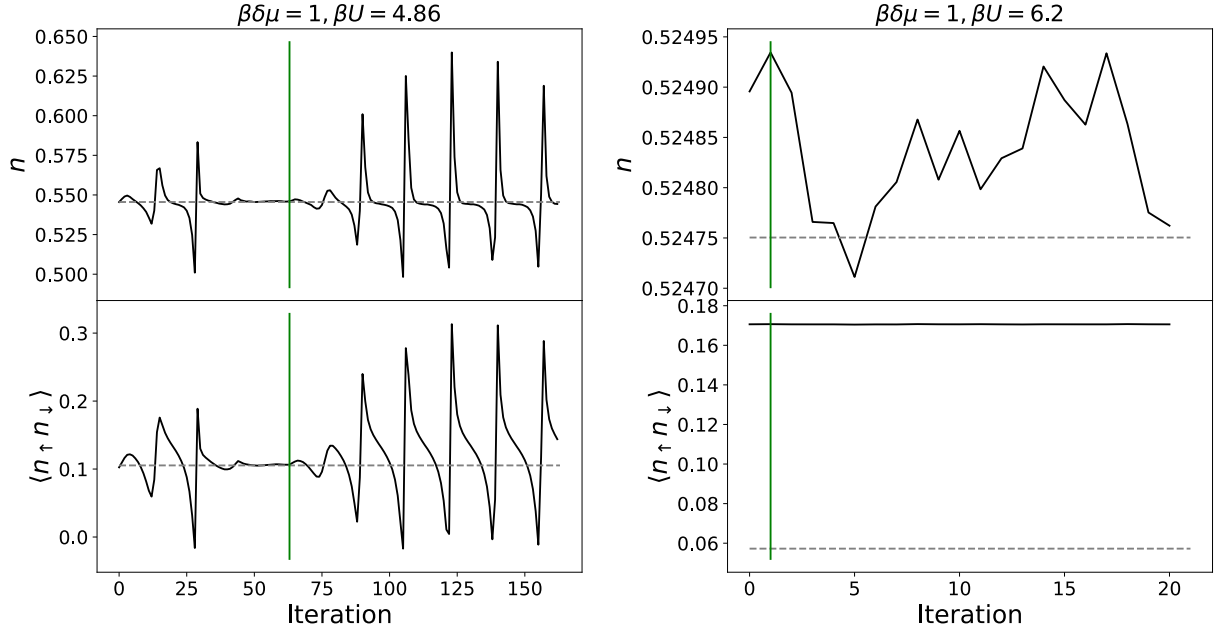
Figure A.10: Filling n and double occupancy $\langle n_\uparrow n_\downarrow \rangle$ of the auxiliary AIM plotted over iterations at $\beta\delta\mu = 1$, where the charge pseudo-divergence is at lower a U value than the pairing divergence. The mixing procedure is applied until the iterative scheme numerically converges, which is marked by a vertical green line, afterward the mixing procedure is switched off. The data shown in the left-hand side panels is calculated for a parameter between the charge pseudo-divergence and the pairing divergence, while the data shown in the right-hand side panels is calculated for a parameter after the paring divergence. The horizontal dashed gray line marks the value of the physical filling/double occupancy.

In Fig. A.10 we see that the mixing procedure leads to a convergence that is not stable when the mixing is switched off for a U value that is between the charge pseudo-divergence and the pairing divergence. Therefore, we conclude that the mixing procedure does not lead to trustful results in this parameter region.

The same investigation is also performed for $\beta\delta\mu = 3$, where the charge pseudo-divergence is at higher a U value than the pairing divergence[5].

---

[5]In the corresponding coexistence region, we start from an unphysical solution.
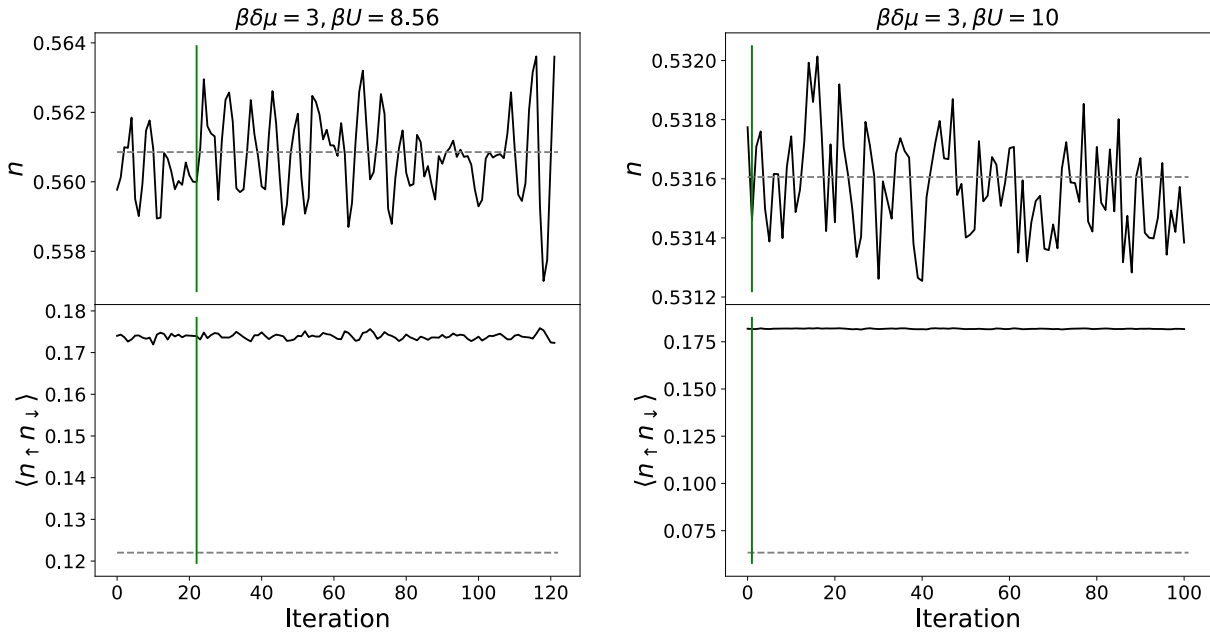
Figure A.11: Filling n and double occupancy $\langle n_\uparrow n_\downarrow \rangle$ of the auxiliary AIM plotted over iterations at $\beta\delta\mu = 3$, where the charge pseudo-divergence is at higher a U value than the pairing divergence. The mixing procedure is applied until the iterative scheme numerically converges, which is marked by a vertical green line, afterward the mixing is switched off. The data in the left-hand side panels is calculated for a parameter between the charge pseudo-divergence and the pairing divergence, while the data in the right-hand side panels is calculated for a parameter after the charge pseudo-divergence. The horizontal dashed gray line marks the value of the physical filling/double occupancy.

In Fig. A.11 we see that the oscillations are way smaller in the parameter region between the charge pseudo-divergence and the pairing divergence than for $\beta\delta\mu = 1$ in Fig. A.10 and differently from this case the oscillations observed before and after switching of the mixing are qualitatively similar. Hence, we conclude that applying the mixing procedure for $\beta\delta\mu > 1.75$ is justified.

Bibliography

1. Martin, R. M., Reining, L. & Ceperley, D. M. Interacting Electrons: Theory and Computational Approaches 1st ed. `https://www.cambridge.org/core/product/identifier/9781139050807/type/book` (Cambridge University Press, 2016).

2. Abrikosov, A. A. Methods of Quantum Field Theory in Statistical Physics. OCLC: 868966450. ISBN: 978-0-486-14015-5. `http://www.myilibrary.com?id=566713` (Dover Publications, 2012).

3. Fabrizio, M. A course in quantum many-body theory: from conventional Fermi liquids to strongly correlated systems. ISBN: 978-3-031-16304-3 (Springer, Cham, Switzerland, 2022).

4. Rohringer, G. *et al.* Diagrammatic routes to nonlocal correlations beyond dynamical mean field theory. *Reviews of Modern Physics* **90,** 025003. ISSN: 0034-6861, 1539-0756. `https://link.aps.org/doi/10.1103/RevModPhys.90.025003` (2018).

5. Thunström, P., Gunnarsson, O., Ciuchi, S. & Rohringer, G. Analytical investigation of singularities in two-particle irreducible vertex functions of the Hubbard atom. *Physical Review B* **98,** 235107. ISSN: 2469-9950, 2469-9969. `https://link.aps.org/doi/10.1103/PhysRevB.98.235107` (2018).

6. Adler, S., Krien, F., Chalupa-Gantner, P., Sangiovanni, G. & Toschi, A. Non-perturbative intertwining between spin and charge correlations: A "smoking gun" single-boson-exchange result. Publisher: arXiv Version Number: 2. `https://arxiv.org/abs/2212.09693` (2022).

7. Ribic, T., Rohringer, G. & Held, K. Nonlocal correlations and spectral properties of the Falicov-Kimball model. *Physical Review B* **93,** 195105. ISSN: 2469-9950, 2469-9969. `https://link.aps.org/doi/10.1103/PhysRevB.93.195105` (2016).

8. Janiš, V. & Pokorný, V. Critical metal-insulator transition and divergence in a two-particle irreducible vertex in disordered and interacting electron systems. *Physical Review B* **90,** 045143. ISSN: 1098-0121, 1550-235X. `https://link.aps.org/doi/10.1103/PhysRevB.90.045143` (2014).

9. Melnick, C. & Kotliar, G. Fermi-liquid theory and divergences of the two-particle irreducible vertex in the periodic Anderson lattice. *Physical Review B* **101,** 165105. ISSN: 2469-9950, 2469-9969. `https://link.aps.org/doi/10.1103/PhysRevB.101.165105` (2020).

10. Gunnarsson, O. *et al.* Parquet decomposition calculations of the electronic self-energy. *Physical Review B* **93,** 245102. ISSN: 2469-9950, 2469-9969. `https://link.aps.org/doi/10.1103/PhysRevB.93.245102` (2016).

11. Springer, D., Chalupa, P., Ciuchi, S., Sangiovanni, G. & Toschi, A. Interplay between local response and vertex divergences in many-fermion systems with on-site attraction. *Physical Review B* **101,** 155148. ISSN: 2469-9950, 2469-9969. `https://link.aps.org/doi/10.1103/PhysRevB.101.155148` (2020).

12. Gunnarsson, O., Rohringer, G., Schäfer, T., Sangiovanni, G. & Toschi, A. Breakdown of Traditional Many-Body Theories for Correlated Electrons. *Physical Review Letters* **119,** 056402. ISSN: 0031-9007, 1079-7114. `http://link.aps.org/doi/10.1103/PhysRevLett.119.056402` (2017).

13. Reitner, M. *et al.* Attractive Effect of a Strong Electronic Repulsion: The Physics of Vertex Divergences. *Physical Review Letters* **125,** 196403. ISSN: 0031-9007, 1079-7114. `https://link.aps.org/doi/10.1103/PhysRevLett.125.196403` (2020).

14. Chalupa, P. *et al.* Fingerprints of the Local Moment Formation and its Kondo Screening in the Generalized Susceptibilities of Many-Electron Problems. *Physical Review Letters* **126,** 056403. ISSN: 0031-9007, 1079-7114. `https://link.aps.org/doi/10.1103/PhysRevLett.126.056403` (2021).

15. Pelz, M. Investigation of the highly non-perturbative nature of the Mott-Hubbard metal insulator transition: Vertex divergences in the coexistence region. Artwork Size: 75 pages Medium: application/pdf Publisher: TU Wien, 75 pages. `https://repositum.tuwien.at/handle/20.500.12708/19742` (2022).

16. Schäfer, T. *et al.* Divergent Precursors of the Mott-Hubbard Transition at the Two-Particle Level. *Physical Review Letters* **110,** 246405. ISSN: 0031-9007, 1079-7114. `https://link.aps.org/doi/10.1103/PhysRevLett.110.246405` (2013).

17. Schäfer, T. *et al.* Nonperturbative landscape of the Mott-Hubbard transition: Multiple divergence lines around the critical endpoint. *Physical Review B* **94,** 235108. ISSN: 2469-9950, 2469-9969. `https://link.aps.org/doi/10.1103/PhysRevB.94.235108` (2016).

18. Vučičević, J., Wentzell, N., Ferrero, M. & Parcollet, O. Practical consequences of the Luttinger-Ward functional multivaluedness for cluster DMFT methods. *Physical Review B* **97,** 125141. ISSN: 2469-9950, 2469-9969. `https://link.aps.org/doi/10.1103/PhysRevB.97.125141` (2018).

19. Chalupa, P., Gunacker, P., Schäfer, T., Held, K. & Toschi, A. Divergences of the irreducible vertex functions in correlated metallic systems: Insights from the Anderson impurity model. *Physical Review B* **97,** 245136. ISSN: 2469-9950, 2469-9969. `https://link.aps.org/doi/10.1103/PhysRevB.97.245136` (2018).

20. Kozik, E., Ferrero, M. & Georges, A. Nonexistence of the Luttinger-Ward Functional and Misleading Convergence of Skeleton Diagrammatic Series for Hubbard-Like Models. *Physical Review Letters* **114,** 156402. ISSN: 0031-9007, 1079-7114. https://link.aps.org/doi/10.1103/PhysRevLett.114.156402 (2015).

21. Rossi, R. & Werner, F. Skeleton series and multivaluedness of the self-energy functional in zero space-time dimensions. *Journal of Physics A: Mathematical and Theoretical* **48,** 485202. ISSN: 1751-8113, 1751-8121. https://iopscience.iop.org/article/10.1088/1751-8113/48/48/485202 (2015).

22. Van Houcke, K., Kozik, E., Rossi, R., Deng, Y. & Werner, F. Physical and unphysical regimes of self-consistent many-body perturbation theory. Publisher: arXiv Version Number: 1. https://arxiv.org/abs/2102.04508 (2021).

23. Kim, A. J. & Kozik, E. Misleading convergence of the skeleton diagrammatic technique: when the correct solution can be found. Publisher: arXiv Version Number: 1. https://arxiv.org/abs/2212.14768 (2022).

24. Tarantino, W., Mendoza, B. S., Romaniello, P., Berger, J. A. & Reining, L. Many-body perturbation theory and non-perturbative approaches: screened interaction as the key ingredient. *Journal of Physics: Condensed Matter* **30,** 135602. ISSN: 0953-8984, 1361-648X. https://iopscience.iop.org/article/10.1088/1361-648X/aaaeab (2018).

25. Stan, A., Romaniello, P., Rigamonti, S., Reining, L. & Berger, J. A. Unphysical and physical solutions in many-body theories: from weak to strong correlation. *New Journal of Physics* **17,** 093045. ISSN: 1367-2630. https://iopscience.iop.org/article/10.1088/1367-2630/17/9/093045 (2015).

26. Rohringer, G. New routes towards a theoretical treatment of nonlocal electronic correlations. Artwork Size: 303 pages Medium: application/pdf Pages: 303 pages. PhD thesis (TU Wien, 2013). https://repositum.tuwien.at/handle/20.500.12708/6957.

27. Rohringer, G., Valli, A. & Toschi, A. Local electronic correlation at the two-particle level. *Physical Review B* **86,** 125114. ISSN: 1098-0121, 1550-235X. https://link.aps.org/doi/10.1103/PhysRevB.86.125114 (2012).

28. Theoretical methods for strongly correlated electrons (eds Sénéchal, D., Tremblay, A.-M. & Bourbonnais, C.) ISBN: 978-0-387-00895-0 (Springer, New York, 2004).

29. Eßl, H. Divergences of the Irreducible Vertex in the Hubbard Atom beyond Particle-Hole Symmetry. *Project work, TU Wien* (2022).

30. Zagoskin, A. Quantum theory of many-body systems. ISBN: 978-3-319-07048-3 (Springer, New York, 2014).

31. Altland, A. & Simons, B. D. Condensed matter field theory. OCLC: 818755106. ISBN: 978-0-511-78998-4 (Cambridge University Press, Cambridge; New York, 2010).

32. Luttinger, J. M. & Ward, J. C. Ground-State Energy of a Many-Fermion System. II. *Physical Review* **118,** 1417–1427. ISSN: 0031-899X. `https://link.aps.org/doi/10.1103/PhysRev.118.1417` (1960).

33. Pavarini, E. Many-body methods for real materials lecture notes of the Autumn School on Correlated Electrons 2019. OCLC: 1197156208. ISBN: 978-3-95806-400-3 (Forschungszentrum Jülich GmbH, Zentralbibliothek, Verlag, Jülich, 2019).

34. Pairault, S., Sénéchal, D. & Tremblay, A.-M. Strong-coupling perturbation theory of the Hubbard model. *The European Physical Journal B* **16,** 85–105. ISSN: 1434-6028. `http://link.springer.com/10.1007/s100510070253` (2000).

35. Pavarini, E. Dynamical Mean-Field Theory of Correlated Electrons lecture notes of the Autumn School on Correlated Electrons 2022 (Forschungszentrum Jülich GmbH, Zentralbibliothek, Verlag, Jülich, 2022).

36. Gull, E. *et al.* Continuous-time Monte Carlo methods for quantum impurity models. *Reviews of Modern Physics* **83,** 349–404. ISSN: 0034-6861, 1539-0756. `https://link.aps.org/doi/10.1103/RevModPhys.83.349` (2011).

37. Georges, A., Kotliar, G., Krauth, W. & Rozenberg, M. J. Dynamical mean-field theory of strongly correlated fermion systems and the limit of infinite dimensions. *Reviews of Modern Physics* **68,** 13–125. ISSN: 0034-6861, 1539-0756. `https://link.aps.org/doi/10.1103/RevModPhys.68.13` (1996).

38. Reitner, M. Notes from Matthias Reitner.

39. Lee, A. Centrohermitian and skew-centrohermitian matrices. *Linear Algebra and its Applications* **29,** 205–210. ISSN: 00243795. `https://linkinghub.elsevier.com/retrieve/pii/0024379580902414` (1980).

40. Fus, D. Breakdown of the many-electron perturbation expansion beyond particle-hole symmetry: {An} atomic limit study. *Bachelor thesis, TU Wien* (2022).

41. Craven, B. D. Complex symmetric matrices. *Journal of the Australian Mathematical Society* **10,** 341–354. ISSN: 1446-7887, 1446-8107. `https://www.cambridge.org/core/product/identifier/S1446788700007588/type/journal_article` (1969).

42. Reitner, M. *et al.* Exceptional Susceptibilities Protect Correlation Induced Phase Instabilities. *Unpublished.*

43. Shiba, H. Thermodynamic Properties of the One-Dimensional Half-Filled-Band Hubbard Model. II: Application of the Grand Canonical Method. *Progress of Theoretical Physics* **48,** 2171–2186. ISSN: 0033-068X. `https://academic.oup.com/ptp/article-lookup/doi/10.1143/PTP.48.2171` (1972).

44. Verstraete, F. *et al.* Density matrix renormalization group, 30 years on. *Nature Reviews Physics* **5,** 273–276. ISSN: 2522-5820. `https://www.nature.com/articles/s42254-023-00572-5` (2023).

45. Strongly Correlated Systems: Numerical Methods (eds Avella, A. & Mancini, F.) `https://link.springer.com/10.1007/978-3-642-35106-8` (Springer Berlin Heidelberg, Berlin, Heidelberg, 2013).

46. Del Re, L. & Toschi, A. Dynamical vertex approximation for many-electron systems with spontaneously broken SU(2) symmetry. *Physical Review B* **104,** 085120. ISSN: 2469-9950, 2469-9969. `https://link.aps.org/doi/10.1103/PhysRevB.104.085120` (2021).

47. Toschi, A., Katanin, A. A. & Held, K. Dynamical vertex approximation: A step beyond dynamical mean-field theory. *Physical Review B* **75,** 045118. ISSN: 1098-0121, 1550-235X. `https://link.aps.org/doi/10.1103/PhysRevB.75.045118` (2007).

48. Skolimowski, J. & Fabrizio, M. Luttinger's theorem in the presence of Luttinger surfaces. *Physical Review B* **106,** 045109. ISSN: 2469-9950, 2469-9969. `https://link.aps.org/doi/10.1103/PhysRevB.106.045109` (2022).

49. Stanescu, T. D., Phillips, P. & Choy, T.-P. Theory of the Luttinger surface in doped Mott insulators. *Physical Review B* **75,** 104503. ISSN: 1098-0121, 1550-235X. `https://link.aps.org/doi/10.1103/PhysRevB.75.104503` (2007).

50. Reitner, M. On the violation of the Luttinger Theorem. *Unpublished.*

51. Wallerberger, M. *et al.* w2dynamics: Local one- and two-particle quantities from dynamical mean field theory. *Computer Physics Communications* **235,** 388–399. ISSN: 00104655. `https://linkinghub.elsevier.com/retrieve/pii/S0010465518303217` (2019).

52. Wallerberger, M. *et al.* sparse-ir: Optimal compression and sparse sampling of many-body propagators. *SoftwareX* **21,** 101266. ISSN: 23527110. `https://linkinghub.elsevier.com/retrieve/pii/S2352711022001844` (2023).

53. Rohshap, S. Analytical calculation of two-particle vertices for multiorbital Hubbard atom. Artwork Size: 101 pages Medium: application/pdf Publisher: TU Wien, 101 pages. `https://repositum.tuwien.at/handle/20.500.12708/176712` (2023).

54. Wu, W., Ferrero, M., Georges, A. & Kozik, E. Controlling Feynman diagrammatic expansions: Physical nature of the pseudogap in the two-dimensional Hubbard model. *Physical Review B* **96,** 041105. ISSN: 2469-9950, 2469-9969. `http://link.aps.org/doi/10.1103/PhysRevB.96.041105` (2017).

55. Maier, T., Jarrell, M., Pruschke, T. & Hettler, M. H. Quantum cluster theories. *Reviews of Modern Physics* **77,** 1027–1080. ISSN: 0034-6861, 1539-0756. `https://link.aps.org/doi/10.1103/RevModPhys.77.1027` (2005).